

**MScR Audio Acoustics**

**Metric-based optimisation of  
acoustic lenses and waveguides**

**Lewis MacDonald**

00426160

lewismacdonald@email.com

Supervisor: Dr Jonathan Hargreaves

Reader: Olga Umnova

**2022**

---

# Abstract

This dissertation develops an automated procedure for the design of acoustic waveguides that can support single parameter (1P) wave propagation over a large bandwidth. 1P waves include plane, cylindrical and spherical waves, and the waveguides aim to either perturb their path or convert between these types. This technology could, for example, be employed in the design of high-precision waveguides and horns for concert sound applications. The design process is driven by two performance metrics proposed by Oclec-Brown, which are calculated from the solution of Laplace's equation in the waveguide. These highlight regions of error in the relative pathlength ("stretch") and change in area ("flare") through the domain. Finite Element Analysis (FEA) is used to calculate these metrics on several test cases. A technique for tracing streamlines of a vector function through the FEA mesh is developed, and these are used to further manipulate the waveguide performance metrics. The method of equalising the relative pathlength by distorting regions of a thin domain, which is covered in the GP Acoustics patent EP3806086A1 (Dodd & Oclec-Brown, 2021), is then investigated. Combined with FEA analysis, this becomes an optimisation tool aiding the design process, and the acoustic performance of the optimised designs is evaluated by FEA simulations of the Helmholtz equation. This is quantified by the uniformity of SPL across the exit of the device. The relationship between arc length and perturbation amplitude is found for triangular and sinusoidal corrugations and used to equalise the relative pathlength in waveguides modelled as shell meshes. The modulated meshes are then re-analysed and the metrics indicate that they are better able to support 1P wave propagation. Thickened 3D waveguides are then considered, and both pathlength and area are optimised using the metrics as design tools. These are shown to perform better acoustically than the unoptimised geometry. Some of the limitations of the pathlength equalisation technique are then explored and discussed.

# Acknowledgements

I would like to express a huge thank you to my supervisor Jonathon Hargreaves for all his patient support and guidance, especially around the beginning of the project when the learning curve was so steep, our meetings always left me feeling positive and inspired.

I would also like to thank Jack Ocle-Brown and Mark Dodd, my colleagues, and mentors. For suggesting such an interesting project and for the in-depth technical guidance throughout.

Lastly, I would like to thank my family and close ones for all the loving help and encouragement throughout my education.

# Table of Contents

1. Introduction .....	7
1.1 Outline of the dissertation .....	9
2. Background & literature review .....	12
2.1 Loudspeaker horns .....	12
2.2 Waveguides and 1P waves .....	13
2.3 Acoustic models of curved ducts .....	14
2.4 Wave manipulation by changing the effective density of air .....	17
2.5 Wave manipulation by path length control .....	18
3. Core mathematical theory .....	20
3.1 Helmholtz wave equation .....	20
3.2 1P Waves .....	21
3.3 Stretch and Flare Metrics .....	22
4. Methodology .....	24
4.1 Finite element analysis – FEA .....	24
4.1.1 Meshes .....	25
4.1.2 Shape functions and element shapes .....	25
4.1.3 Calculating the gradient over an FEA mesh .....	26
4.1.4 Finite element mesh types .....	26
4.2 Tracing streamlines .....	27
4.2.1 Forward Euler method .....	28
4.2.2 RK4 method .....	28
4.2.3 Tracing streamlines through an FEA mesh .....	29
4.2.4 Inverse coordinate system mapping .....	30
4.2.5 Mapping data between nodes and streamlines .....	30
4.3 Numerical calculus techniques .....	31
4.3.1 Cumulative trapezoid numerical integration .....	31
4.3.2 Central difference numerical gradient .....	31
4.4 Metric calculation methods .....	32
5. Understanding the metrics .....	32
5.1 Test geometries .....	33
5.2 Stretch $s$ .....	37
5.3 Normalising stretch .....	40
5.3.1 Minimum-normalised stretch $sn$ .....	40
5.3.2 Average-normalised stretch $sa$ .....	42
5.4 Cumulative required pathlength $\xi r$ .....	42
5.5 Normalised required pathlength $\xi n$ .....	45
5.6 Flare and felt area, $f$ and $af$ – the area metrics .....	46
5.7 Conclusions .....	50
6. Waveguide pathlength optimisation .....	51
6.1 Adding path length with corrugations .....	51
6.1.1 Corrugation shapes .....	52
6.1.2 Arc length to amplitude relationship .....	53
6.1.3 Error from adding pathlength with sinusoidal corrugations .....	56
6.1.4 Corrugation curvature .....	57
6.1.5 Problems with computing the gradient on corrugated meshes .....	57
6.1.6 $\xi n$ spaced meshes .....	60
6.1.7 Further mesh problems caused by triangular shaped corrugations .....	61

6.2	Optimisation test case – Half sine .....	62
6.2.1	Re-analysing a modulated domain .....	63
6.2.2	Effect of pathlength optimisation on felt area - <i>af</i> .....	67
6.2.3	Average squared metric error – Half sine .....	68
6.3	Optimisation test case – Channel Wedge .....	68
6.4	Optimisation test case – S-bend .....	70
6.5	Conclusions .....	72
7.	Three-dimensional geometry .....	74
7.1	Correcting for area – Iterative rectangular cuboid example .....	74
7.2	Acoustic performance of a single thickened corrugation .....	76
7.2.1	Sine shaped corrugation – amplitude and thickness .....	77
7.2.2	Sine shaped corrugation – length and thickness .....	79
7.2.3	Triangular shaped corrugation – Fourier series .....	81
7.3	Creating 3D modulated domains .....	83
7.4	Acoustic simulations of optimised geometry .....	85
7.4.1	Acoustic performance of the half sine .....	86
7.4.2	Effect of thickness on acoustic performance .....	87
7.4.3	Effect of the number of corrugations on the acoustic performance .....	89
7.4.4	Channel-wedge geometry .....	91
7.4.5	S-bend geometry .....	94
7.5	Adding extra channels on to either side of the S-bend – transitions .....	95
7.5.1	Effect of extra channel sections on stretch metric .....	95
7.5.2	Effect of extra sections on area optimisation .....	96
7.5.3	Effect of extra sections on the acoustic performance .....	98
7.6	Circle to square converter .....	99
7.7	Re-analysing a 3D modulated domain .....	102
7.7.1	Metric banding .....	103
7.8	Conclusions .....	104
8.	Discussion, conclusions and future work .....	105
8.1	Waveguide metrics .....	105
8.2	Performance limitations .....	106
8.3	Corrugation shapes .....	106
8.4	Design parameters trade off – The balancing act .....	107
8.5	Acoustic FEA accuracy and approximations .....	108
8.6	Lumped parameter acoustic modelling .....	108
8.7	Future work .....	109
8.7.1	Building samples to validate simulations .....	109
8.7.2	Explore optimising different designs .....	109
8.7.3	Iterative geometry optimisation .....	109
8.7.4	Modelling Viscous losses .....	110
9.	References .....	111
	Appendix A: A method for numerically testing if an acoustical waveguide admits one- parameter waves .....	113

# Glossary

Glossary of symbols	
$\rho_0$	Density of air
$c$	Speed of sound (assumed to be 343m/s)
$k$	Wavenumber $\frac{\omega}{c}$
$u$	Solution to Laplace's equation, See Eq. (12)
$p$	Pressure
$U$	Volume velocity
$Z_t$	Throat impedance
$SPL$	Sound pressure level
$s$	Stretch metric, see Eq. (13)
$s_n$	Stretch metric with minimum normalisation, see section 5.3
$s_a$	Stretch metric with average normalisation
$s_o$	Stretch metric offset, see section 6.2.1
$\xi$	Physical arc length of path which follows $\nabla u$ , see section 3.2
$\xi_r$	Mapped arc length referenced to the longest relative pathlength, see Eq. (35)
$\xi_n$	$\xi_r$ normalised to one, see Eq. (36)
$f$	Flare metric, see Eq. (16)
$a_f$	Felt area, see Eq. (18)
$\kappa$	Curvature, see Eq. (34)
$L$	Corrugation period or wavelength
$d$	Corrugation arc length
$A$	Corrugation amplitude
$n_{mod}$	Number of corrugations
$a_t$	Target cross sectional area through a device
$w$	Domain width
$w_n$	Normalised relative change in width. see Eq. (50)
$t_b$	Base thickness. see Eq. (49)
$t_c$	Thickness correction. see Eq. (51)
$t_o$	Optimised thickness. see Eq. (52)

# 1. Introduction

Since the dawn of loudspeakers for public address, horns have been used to enhance audience coverage and improve the efficiency of the system. Now that loudspeaker drivers and amplifiers which are comfortable handling high power are more common and cheap, there is not such a demand for the increase in efficiency gained in horn loaded loudspeaker systems for midrange and low frequency sound reproduction. However, horns are still used extensively, especially in professional audio to control the directivity of the sound radiation and improve the radiation efficiency of high frequency compression drivers. The shape and design of a horn is an important design problem as it has a big influence on the driver, and therefore the frequency response of the combined system.

In this dissertation we choose to follow the waveguide definition by Geddes, as is done by Kolbrek & Dunker. They define a waveguide as “A type of horn design primarily to guide and shape the sound waves, the main purpose of a waveguide is directivity control rather than loading” (Kolbrek & Dunker, 2019, p.1021).

Another device used for shaping sound waves is an ‘acoustic lens’. An acoustic lens is a mechanical device used usually to improve dispersion at high frequencies by focusing the sound waves, similar to how an optical lens focuses light. Kolbrek & Dunker (2019) discuss two different types of acoustic lenses which focus sound waves using different techniques: The obstacle type, which relies on modifying the effective density of air by filling part of the space with obstacles smaller than a wavelength, and the path length type where the sound travels through separate channels giving different pathlengths.

Horns, waveguides, and acoustic lenses are all, therefore, names for devices which are used to sculpt sound waves to control directivity and match impedance. This is achieved by manipulating the velocity or pressure and phase distribution throughout the device.

There are many situations where it is desirable to be able to effectively sculpt sound waves or convert them from one shape to another. For example, advances in waveguide technology have improved the capabilities of professional audio line arrays, which are nowadays the most popular choice for large scale sound reproduction because they have useful directivity characteristics for equal coverage over large areas. Line arrays consist of many separate cabinets which are designed to sum together creating a line source that produces a cylindrical waveform. At high frequencies each cabinet is large compared to the wavelength, so the directivity of each individual cabinet must mimic a line source, in the near-field at least.

This means at high frequencies the sound wave generated by the compression driver diaphragm must somehow be converted into a wave that exits from a thin rectangular slot shape with equal velocity distribution and phase coherence across the mouth, with an aim to form neat cylindrical sound wave radiation. This is not easily done.

To try and achieve this, line arrays generally use waveguides that attempt to morph a sound wave by coupling a circular aperture compression driver to a linear slot, hoping to create a waveform with the correct velocity distribution across the mouth. This complex optimisation problem has considerable application in the audio industry, and many contrasting approaches are seen in different products (Heil, 1992) (Spillmann & Riemersma, 2017).

Many designs arise from an overly geometrical mindset, so may not produce the desired performance when faced with real acoustic waves. Notably the possibility of modal effects in the waveguide is ignored, which are quite possible given their large size when compared to the wavelength and how modes are known to be problematic in compression drivers. If the 'equal velocity distribution and phase coherence across the mouth' condition is not met, it will lead to problematic interference patterns and uneven audience coverage.

The aim of this project is to create a physics-led methodology for designing waveguides, horns, and acoustic lenses that can meet this condition over a limited bandwidth. This means to create optimised geometries that maintain a phase coherent wavefront as the wave propagates through the device, and which satisfies the required input and output port shapes and expansion profiles.

Controlling the phase, pressure distribution, and expansion throughout a device allows both the throat impedance and the far field pressure distribution to be manipulated. If a reliable design method can be formulated, it would not only help with the circular to rectangular transition problem in line array sources but would allow horns and waveguides of many shapes to be optimised.

This project investigates the potential of two waveguide metrics proposed by Oclee-Brown as tools for both analysing a waveguides performance and as a guide for modifying the waveguides geometry to improve it. The metrics "stretch and "flare" measure the localised error in relative pathlength and change in area through the domain respectively. If both metrics indicate no change, or error, then the waveguide should support perfect single parameter (1P) wave propagation at any frequency. The metrics are calculated from the solution to Laplace's equation, which is computed on different test domains using Finite Element Analysis (FEA).

To correct for the difference in relative pathlength shown by the stretch metric, a technique outlined in the GP Acoustics patent EP3806086A1 (Dodd & Oclee-Brown, 2021) and presented in the follow up paper (Dodd & Oclee-Brown, 2022) is investigated. The method

works by offsetting regions of a thin domain in the direction normal to the surface to warp the channel and add pathlength to specific regions. The limitations of this technique are then explored through acoustic simulations of the optimised waveguides.

The main research questions for this project are therefore:

- How effective are the stretch and flare metrics at characterising problematic regions within a waveguide?
- How much correlation is there between the error shown by the metrics and the acoustic performance of a waveguide?
- How useful are the metrics as guides for modifying a waveguides geometry to make it more capable of supporting 1P wave propagation?
- How well does the pathlength equalisation technique outlined in the GP Acoustics patent EP3806086A1 work for reducing differences in the relative pathlength through a device?
- What are the limitations to the pathlength equalisation method?

## 1.1 Outline of the dissertation

This section contains a short outline of the contents of this dissertation

- Chapter 2 reviews the literature related to horns and waveguides. Research on modelling curved ducts is explored and different techniques used for sculpting the wavefront shape as it propagates through a device are discussed.
- Chapter 3 covers the relative mathematical theory fundamental to the research project. First the governing equations are discussed, then the maths behind single parameter (1P) wave propagation is examined.
- Chapter 4 considers the methodology used for this research project. This starts with the waveguide metrics proposed by Ocle-Brown. Then the required methods for calculating and processing the metrics over an arbitrary shaped geometry are covered, this involves finite element analysis (FEA), its approximations, tracing streamlines through an FEA mesh, and finally numerical calculus techniques.
- In chapter 5, additional understanding and meaning is brought to the waveguide metrics through analysing numerical FEA simulations of them on different test case geometries. Using traced streamlines of  $\nabla u$  it is found that the metrics can

be manipulated further. For instance, a method for the normalisation of the stretch metric is proposed. Streamline integration is performed which allows for both an abstract arc length coordinate,  $\xi_r$ , to be calculated and for the “flare” metric  $f$  to be converted into  $a_f$ , the ‘felt area’, a measurement of the relative change in area through a domain. The chapter also investigates the effect of curvature in channels of constant cross-sectional area on the metrics.

- Chapter 6 commences the study of how best to optimise a waveguide, with the intention of reducing the error shown by the metrics and improving a waveguide’s capability for supporting single parameter wave propagation. Compensating for error in the relative pathlength (stretch metric) is attempted through distorting regions of a thin shell domain with periodic corrugations. The relationship between the amplitude and arc length of different corrugations is investigated and is then used to add corrugations with the correct amplitude to each part of a geometry. Some issues with mesh gradient calculations which arise from distorting thin shell meshes are identified, and where possible techniques to reduce this calculation error are implemented.

To determine whether the pathlength compensation offers an improvement, the distorted shell meshes are re-analysed using the same waveguide metrics to see if their values have reduced. In all the test cases, the stretch metric shows reduced error on the pathlength-optimised geometry. Interestingly, it is found that correcting the relative pathlength also reduces the area error indicated by the felt area metric  $a_f$ .

- In Chapter 7 three-dimensional geometries are considered. The chapter starts by iteratively optimising a distorted cuboid to reduce the area error shown by  $a_f$ . The optimisation process reduces the magnitude of the distortion, and the shape of the domain increasingly resembles a perfect cuboid on each iteration.

Next two-dimensional simulations of the acoustic performance of a single thickened corrugation are studied to gain insight into the impact of forcing sound waves of different frequencies through a corrugation shape. Different geometric corrugation parameters are tested to help understand the effect of domain thickness, corrugation amplitude, and corrugation shape.

The methods and mathematics behind thickening (lofting) a shell mesh into a three-dimensional mesh are discussed. Acoustic simulations of the Helmholtz equation are performed on three-dimensional models with and without pathlength and area optimisation. The ‘half sine’ is studied with different

geometric design parameters, then the 'channel-wedge' and 'S-bend' test case geometries are also analysed. The rate of onset of curvature is identified as a possible issue, so extra channels are added to each end of the S-bend geometry; this is optimised and the metrics and acoustic performance re-analysed. A more complex model, the circle to square plane wave converter, is optimised using the same techniques and the acoustic performance is shown to significantly improve.

The chapter ends by re-analysing a 3D modulated domain with the waveguide metrics. The thickness of the domain causes strong banding in the waveguide metrics through the domain which is most intense at the peaks and troughs of the corrugations. A method for mitigating this is proposed but remains to be investigated as future work.

- In chapter 8 some of the approximations to the simulations are considered. General conclusions on the waveguide optimisation process are made, and some of the limitations to the corrugation based relative pathlength equalisation method are discussed. To finish off, future work and interesting directions with which to carry on the research project are explored.

## 2. Background & literature review

To investigate optimising acoustic horns, lenses, and waveguides, an understanding of various acoustical and mathematical topics is first necessary. This includes loudspeaker horns, directivity control, waveguides, the effect of bends in horns and ducts, and methods of wavefront manipulation.

### 2.1 Loudspeaker horns

Horns have been used in loudspeaker systems for a long time. They were very popular in the 1900's as they help increase the radiation efficiency of a system, which was particularly important then as the drivers and amplifiers of that era had very low power handling compared to the systems of today. Loudspeaker horn design took off in the 1920's after Webster's horn equation (Webster, 1919) which introduced the concept of acoustic impedance for loudspeaker horns and allowed the characteristics of horn systems to be predicted using simple analytical models.

$$\frac{1}{S} \frac{d}{dz} \left( S(z) \frac{dP}{dz} \right) + k^2 P(z) = 0. \quad (1)$$

Webster's horn equation is a simplified version of the wave equation that takes into account the cross-sectional area of a horn  $S$  and the one-dimensional spatial coordinate  $z$ . While it works as a good approximation at low frequencies, it assumes that the propagating pressure waves are planer, normal to the axis of the horn  $z$ , and have equal sound energy distribution across the wavefront. This assumption can lead to errors especially at high frequencies where small discontinuities in the horn can cause the wavefronts to become disturbed. A concise description of basic horn theory, including how to calculate the acoustical input impedance of infinite horn expansions, is presented in Kinsler & Frey (2000). An extensive bibliography of literature on horns can also be found in Kolbrek & Dunker (2019).

1D analytical models based on Webster's horn equation are commonly used for modelling horns at low frequencies. Due to their simplicity when compared with the full wave equation, insightful analytical relations can be easily derived. However, they are of limited use in the analysis of waveguides and acoustic lenses as they do not model the pressure distribution or wavefront shape throughout the horn, or at the horn mouth, so cannot be used to predict the directivity of a device.

## 2.2 Waveguides and 1P waves

The concept of an acoustic waveguide became widespread after it was used by Geddes (1989) to describe particular shapes which are co-planer with the coordinate surfaces of a coordinate system where the wave equation is separatable. Geddes (1989) uses the concept of single parameter (1P) solutions to the wave equation that satisfy:

$$\frac{\partial}{\partial v} \frac{\partial}{\partial w} \psi(u, v, w) = 0. \quad (2)$$

Here  $\psi$  is the scalar velocity potential function and  $u$ ,  $v$ , and  $w$  are the coordinates in a general 3D space. Eq. 2 means the propagation of  $\psi$  is purely in the  $u$  direction and will not intersect either of the other two spatial coordinates, travelling always perpendicular to them.

Geddes wrote that “If the wave fronts are not 1P, then the waves, as they propagate down the horn, will not move parallel to the bounding contours but instead will be forced to either intersect the waveguide contour, reflecting off the walls as they travel; or cease to remain in contact with the walls, propagating freely into space, unconstrained and uncontrolled”. For neat 1P wave propagation to take place, the waveguide must be excited at the throat by the correct waveshape for that waveguide, otherwise transverse modes will become excited.

Geddes then created an axisymmetric waveguide which uses an oblate spheroidal (OS) coordinate system to morph from a circular plane wave into a spherical wave. Using the 1P assumptions he was able to predict the acoustic impedance and velocity across the radiating surface.

Putland challenged this idea in 1993, showing mathematically that there are only three coordinate systems which will allow for true 1P wave propagation, and the oblate spheroidal coordinate system is not one of them. He shows that for a 1P wave within these three coordinate systems the wave equation will reduce to Webster’s horn equation exactly, and in all other scenarios Webster’s horn equation is an approximation.

In a follow up paper Geddes (1993) re-visited the OS waveguide but without using the 1P assumptions from his initial paper. This makes the mathematics required to model the sound propagation considerably more complex, so a numerical relaxation technique was used. Different modes were calculated independently, making the exact final solution the sum of an infinite series. Fortunately, modelling just the first few modes was sufficient as they were by far the most important. Geddes (1993) found that for an OS waveguide with narrow dispersion ( $<15^\circ$ ) the sound propagation is very close to 1P. However, for wider dispersion waveguides, at high frequencies especially, higher order modes begin to disrupt the sound waves.

While the OS waveguide proposed by Geddes (1989) may not support perfect 1P wave propagation, his insight and reasoning for building devices which are capable of supporting 1P wave propagation is fundamental to the development of the design techniques explored in this dissertation.

It is very easy to accurately predict the acoustic field in a domain which has 1P wave propagation, as the acoustic wavefront shape is the same regardless of the frequency. However, in many real-world acoustic problems it is not possible to create geometries which meet Putland's (1993) conditions for 1P wave propagation. For example, in horn design the horn area usually expands to give the transducer a better acoustic load, and sometimes, especially in the case of low frequency horns, it is required that the horn path is curved as well. The next section looks at literature on modelling the acoustics inside of a curved duct.

### **2.3 Acoustic models of curved ducts**

A straight duct of constant cross-sectional area excited by a plane wave will theoretically support 1P planer wave propagation forever if there are no losses. However, if there is a bend or curve in the duct, this may cause the sound waves to be partially reflected off the boundaries when the wavelength is small enough that it is comparable to the width of the duct. This can quickly turn neat plane wave propagation into a modal mess in which the wave shapes are much more complex and difficult to predict or model. It will also affect the input radiation impedance to the duct, which may be an issue depending on the intended use.

Kolbrek & Dunker (2019) investigated the input impedance of a duct with various types of 90° bend using Boundary Element Method (BEM) simulations. The duct was terminated with a  $\rho_0 c_0$  boundary condition on the exit and excited by a plane wave at the other end. The different 90-degree bend shapes are shown in Figure 1 and the simulated throat impedance

is plotted in Figure 2. The letters indicate which throat impedance result is related to which 90° bend shape.

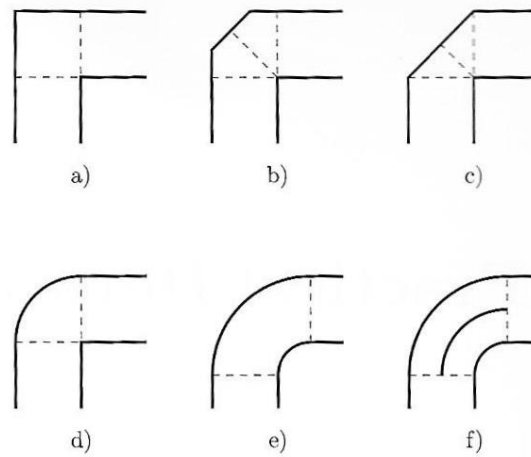


Figure 1: Example 90-degree bend duct geometry (reproduced from Kolbrek & Dunker, 2019)

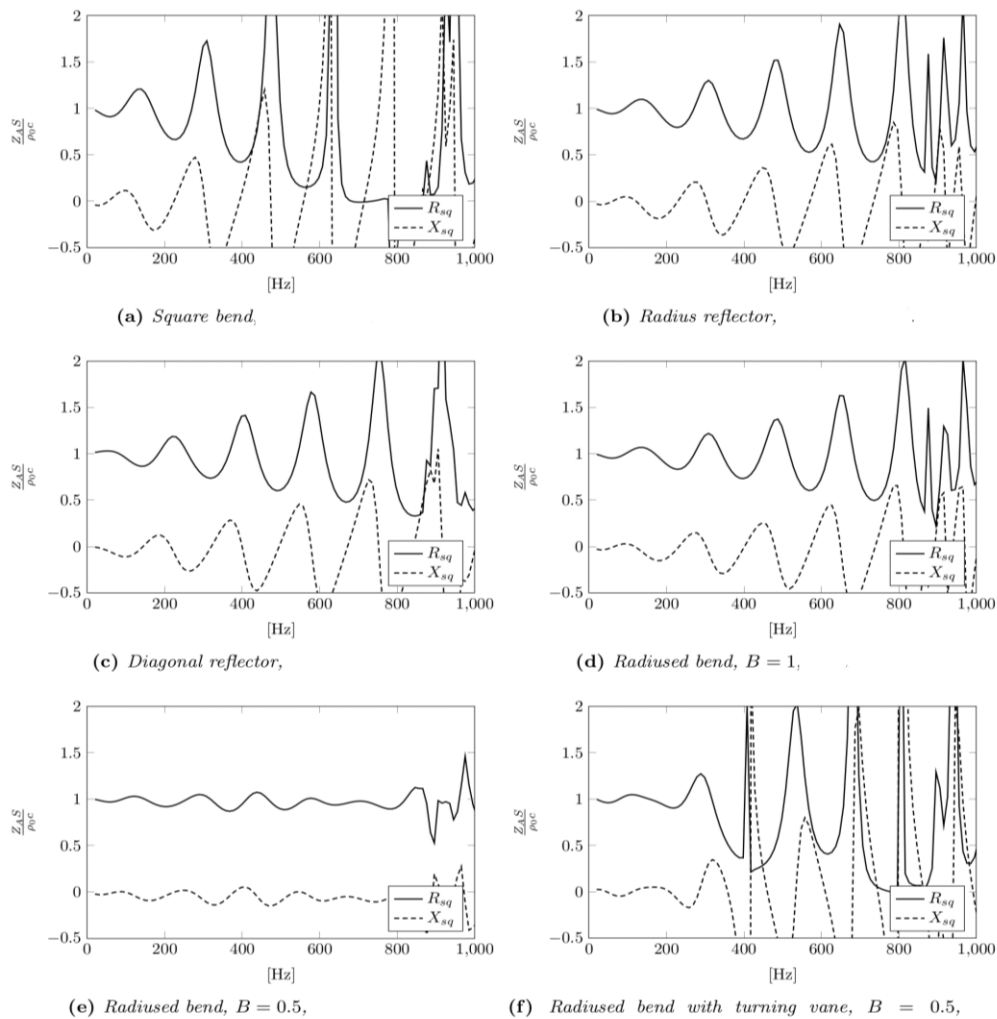


Figure 2: Normalised Acoustic Impedance comparing different 90-degree bends in a duct, (reproduced from Kolbrek & Dunker, 2019)

Figure 2 shows how strongly the shape of the 90-degree bend affects the throat impedance. The spikes seen in the throat impedance arise from disruption to the propagating sound waves due to reflections off the boundaries of the duct during the bend. Bend (a), the square bend, causes large spikes in the throat impedance, which indicates particularly severe internal reflections and modal excitement. The radiused bend, (e), has the flattest throat impedance which suggests that a smooth arced bend is the best option for reducing internal wall reflections in the duct.

Numerical techniques such as Finite Element Analysis (FEA) and BEM are well suited for modelling arbitrary shaped geometry such as the ducts seen in Figure 1. However, the methods give little analytical insight and can be computationally expensive, especially if a high frequency sampling density is required.

Several other techniques are available for modelling the acoustics inside a two-dimensional curved duct. The most traditional and purely analytical method is to find solutions which satisfy the wave equation with the specific domain shape and boundary conditions. However, this technique is limited to geometries where the equations of motion are known to be separable.

A more flexible “multi-modal method” (MMM) is proposed by Felix & Pagneux (2001), which can determine the wave propagation in finite two-dimensional rigid circular bends of any dimension or frequency, even if the width of the duct changes throughout the curve. Their method works by characterising the impedance using a first order differential Riccati equation with the particular geometric design parameters and boundary conditions. From the impedance, the pressure and velocity can then be computed throughout the geometry. Felix & Pagneux (2001) use numerical Runge-Kutta algorithms to integrate the Riccati equation down the inlet of the curved duct. Their multi-modal method is shown to be very accurate when validated against an analytical solution of the Helmholtz equation in a circular bend, for which the acoustic pressure can be solved through separation of the variables.

The analytical formulation of the equations in the MMM technique can give useful insights into the acoustic properties of a curved duct which might not be obtained when using FEA or BEM.

Both the BEM simulations by Kolbrek & Dunker (2019) and the multi-modal models by Felix & Pagneux (2001) show that the acoustic field inside of a curved duct is considerably more complex, especially at high frequencies, than the single parameter wave propagation that can be found in a straight duct.

If the acoustic wavefronts could be manipulated or shaped as they propagate round a bend, it might be possible to create a curved duct in which the wavefronts are more organised and closer to 1P. The next section investigates different techniques which have been used to try and sculpt the shape of the propagating sound waves.

## 2.4 Wave manipulation by changing the effective density of air

Yang, Jia, Lu, Sun, & Yang (2017) investigate designing an impedance-matching acoustic bend which uses perforated plates or side pipes to change the mass density and bulk modulus of parts of the duct. This is used to tune the refractive index causing the sound waves to bend around a corner. Their technique shows improved energy transmission when compared to an unoptimized bend, but it functions over a limited bandwidth which may be too small for practical use in waveguides or acoustic lenses designed for wideband sound reproduction.

Their technique is like the obstacle type of acoustic lens described by Kock & Harvey (1949) in which small obstacles are used to change the effective density of the air and control the velocity of the propagating sound wave. It is shown that for an array of  $N$  of spheres per unit volume, the effective density is:

$$\rho = \rho_0 + \frac{1}{2}N\rho_0V, \quad (3)$$

where  $\rho_0$  is the density of air and  $V$  is the volume of one sphere. The change in velocity is:

$$\left(\frac{v}{v_0}\right)^2 = 1 + \frac{2\pi}{3}Na^2, \quad (4)$$

where  $a$  is the radius of one sphere.

A similar method can also be used to manipulate the impedance of a horn, Shaw (1971) describes how to design an acoustic horn with a spatially varying medium which changes the effective density of air inside of the device and can be used to further improve the impedance matching properties of the horn. His paper suggests using, elastic tubes, flexible internal membranes, and perforated plates to control the effective density.

Other related devices use acoustic metamaterials, which use sub wavelength internal structures designed to manipulate the waves. An example acoustic lens of this type is the 'VARI-SOUND' (Memoli et al., 2019), which can be used to focus sound waves radiating in free air from a loudspeaker.

Controlling an acoustic wave through modifying the effective density of the air has a few issues. Firstly, it is likely to introduce losses to the system which will reduce the power transmission through the device. In some devices additional damping could be beneficial but in others it could be a problem. Secondly, it can be hard to create obstacles which will accurately control the effective density over a wide frequency band, especially if the effective density must smoothly change from position to position throughout the device.

## 2.5 Wave manipulation by path length control

Another method for waveshape manipulation is to use channels which control the pathlength through a device.

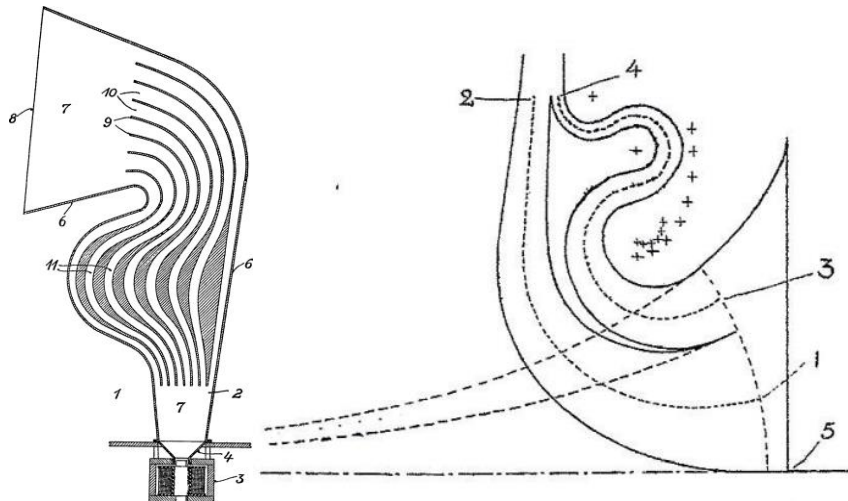


**Figure 3: Two Examples of Horn Path Length equalising (DE Patent 578 053 (1931) (reproduced from Kolbrek & Dunker, 2019))**

Two examples of this are shown in Figure 3. Both designs split the horn path into separate channels which seek to equalise the pathlength from the horn entrance to exit as it bends around a corner. There is no available data which reveals how well these designs work.

The approach of splitting the horn path into separate channels to add pathlength to specific regions of a device has been used in several commercial professional audio products. One example is the JBL-2935 acoustic lens shown in Figure 4 which uses thin slanted metal plates to add pathlength and delay specific parts of the wavefront with an aim to control the devices directivity.



**Figure 4: Example of a pathlength acoustic lens JBL 2935 (JBL Professional series acoustic lens family, 1954)**

Acoustic lenses of this style were most popular between the 50's and 70's and were usually designed to create wide horizontal dispersion and narrow vertical dispersion. The directivity control is mediocre when compared to modern constant directivity horns, and the large relatively complex design makes them expensive to manufacture which is probably why they are rarely used now.

The Turbosound 'Polyhorn' is a modern example of wave manipulation with pathlength control. Figure 5 shows section drawings of a coaxial driver mounted in the Polyhorn device. The high frequency sound path in front of the compression driver (label 11) is split up into many separate channels which aim to equalise the pathlength from the entrance (label 13) to the exit (label 23), which is a tall, narrow, and slightly curved rectangular shape which aims to create a toroidal sound source at high frequencies.

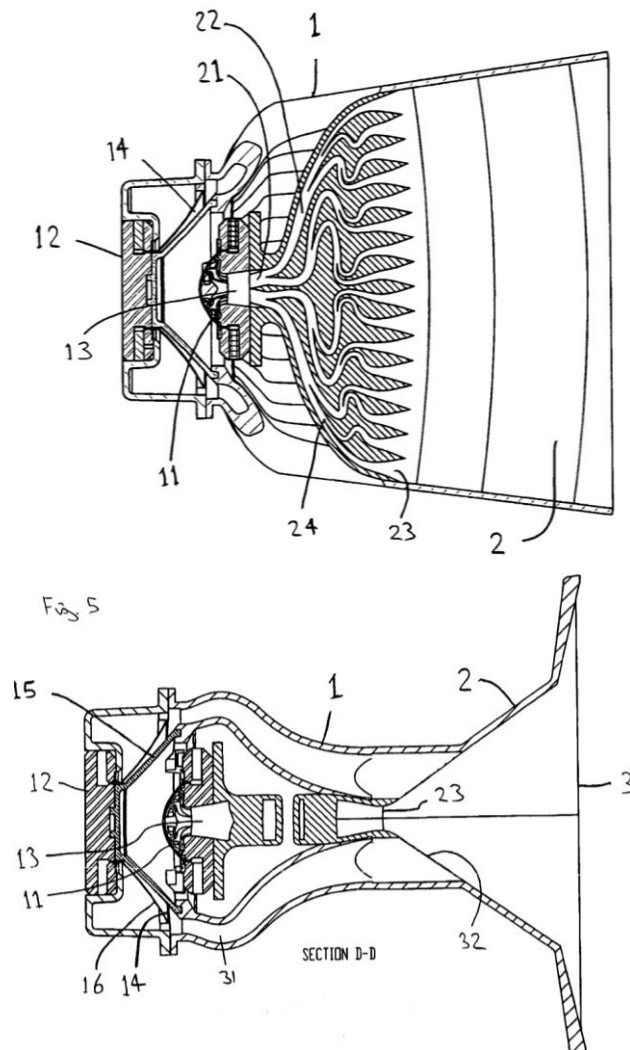


**Figure 5: Turbosound Polyhorn coaxial driver and horn section drawing, Top: Side View, Bottom, Top View (Dickie, L. (2009)).**

Sound sources which create toroidal or cylindrical wave shapes work well in arrays as there is less problematic interference between each source device.

The output from the midrange driver (label 15) is also directed through channels (label 31) which bend around the compression driver unit and join into the same horn mouth (label 32) to create a more localised sound source.

There are no available measurements which show how controlled the wave front is from the Polyhorn device over a large frequency range, but it remains a popular choice for professional audio sound reproduction.

## 3. Core mathematical theory

### 3.1 Helmholtz wave equation

Mathematical modelling of many situations involving natural phenomena leads to Partial Differential Equations (PDEs). Acoustics is no exception and assumptions of linearity and adiabatic behaviour lead to the linear wave equation (Kinsler & Frey, 2000, p 39).

The Helmholtz equation is the time-harmonic steady-state version of the linear wave equation and has a variety of applications in physics, including acoustics. It is stated as:

$$\nabla^2 p + k^2 p = 0, \quad (5)$$

where  $k = \omega/c$  is the wavenumber in radians per metre and  $p$  is pressure. In one, two and three dimensions the Helmholtz equation respectively is:

$$\frac{\partial^2 p}{\partial x^2} + k^2 p = 0, \quad (6)$$

$$\frac{\partial^2 p}{\partial x^2} + \frac{\partial^2 p}{\partial y^2} + k^2 p = 0, \quad (7)$$

$$\frac{\partial^2 p}{\partial x^2} + \frac{\partial^2 p}{\partial y^2} + \frac{\partial^2 p}{\partial z^2} + k^2 p = 0. \quad (8)$$

The PDE holds in a region called the domain. The solution of the PDE will depend on the frequency, the geometry of the domain and the boundary conditions. For a two-dimensional domain the boundary will be an edge, and for a three-dimensional domain the boundary will

be a surface. Some typical boundary conditions for the Helmholtz equation are sound-hard (rigid) boundaries (walls), impedance boundaries, and radiation boundaries.

### 3.2 1P Waves

Morse (1948), cited in Putland (1993), defined a one parameter (1P) wave as a solution to the Helmholtz wave equation which depends on only one of the three spatial coordinates. Putland (1993) states how this one spatial coordinate  $u$  may then be a function of other coordinates, for example three Cartesian coordinates  $x$ ,  $y$ , and  $z$ :

$$P = P(u(x, y, z)). \quad (9)$$

Putland then goes on to show how 1P waves exist only if  $|\nabla u|$  and  $\nabla^2 u$  are functions of  $u$  alone. This is expressed as:

$$\nabla u = M(u)\mathbf{e}_u, \quad (10)$$

$$\nabla^2 u = N(u). \quad (11)$$

Here  $M$  and  $N$  are real functions and  $\mathbf{e}_u$  is a unit vector in the direction of  $\nabla u$ . A 1P wave has an equal pressure magnitude across the entire wavefront as the pressure depends only on a single spatial coordinate, which is a convenient property in many acoustic design problems.

Putland also explains how  $u$  can be turned into another coordinate  $\xi$  which measures arc length along the path of surfaces of constant  $u$ . A  $\xi$  path is therefore any path which follows  $\nabla u$  and the value of  $\xi$  is the cumulative arc length of this path.

Putland concludes that the only coordinates systems which will support exact 1P propagation are cartesian, cylindrical, and spherical, which create planar, cylindrical, and spherical wave shapes respectively, and that no new 1P horn geometries remain to be discovered. He also shows how 1P wave propagation is the only scenario where Webster's horn equation (Eq. (1)) is perfectly satisfied without making any approximations as it also depends on a single spatial parameter.

If a waveguide supports 1P wave propagation, or close to it over a range of frequencies, it will generally have predictable organised wavefronts in this bandwidth. This leads to controlled directivity and good coupling capabilities at the mouth and throat as no cross modes are excited. Due to the lack of disruption in the waveshape, a device which supports 1P wave propagation will also have a smooth throat impedance which provides a good acoustic loading for a driver coupled to the throat. Therefore, in the scope of this project, a geometry that

produces more organised 1P-like wave propagation over a wide range of frequencies is assumed to have ‘better’ performance.

Cases can, however, be conceived where a waveguide that doesn’t produce 1P wave propagation might be desired. Waveguides of this type are outside the scope of this dissertation.

### 3.3 Stretch and Flare Metrics

Laplace’s equation, sometimes referred to as the heat equation, is a second order partial differential equation which is commonly used to simulate steady state heat conduction. Laplace’s equation is

$$\nabla^2 u = 0 \quad (12)$$

Laplace’s equation can be used to model an equilibrium situation that is non-oscillatory. The solution will depend on the geometry and the boundary conditions. Two important boundary conditions are the Dirichlet boundary condition, which specifies the value  $u$  on a boundary, and the Neumann boundary condition which specifies the value of the derivative of  $u$  normal to a boundary, often denoted  $\partial u / \partial n$ . Laplace’s equation is also a special case of the Helmholtz equation with  $k = 0$ .

Oclee-Brown has suggested an extension to Putland’s work that arises from applying it to solutions of Laplace’s equation. This is a reasonable approach because 1P solutions of the Laplace and Helmholtz equations have closely related forms. Furthermore, Oclee-Brown has proposed two metrics – ‘stretch’ and ‘flare’ – that quantify deviation of a solution  $u$  from Putland’s conditions for 1P waves. This work is unpublished at the time of writing but has been included in Appendix A with his permission.

The ‘stretch’ metric  $s$  is defined as:

$$s = |\nabla \xi|. \quad (13)$$

Here  $\xi$  is the cumulative path length along a loci running perpendicular to planes of constant  $u$ . Putland defined  $\xi$  as:

$$\xi(u) = \int \frac{du}{|\nabla u|} \quad (14)$$

Stretch  $s \neq 1$  therefore indicates regions where surfaces of constant  $\xi$  are too close together or too far apart compared to the norm.

The flare rate term from Websters horn equation is:

$$f = \frac{1}{S} \frac{dS}{d\xi}, \quad (15)$$

which describes how much the flare  $dS/d\xi$  changes with cross sectional area,  $S$ . Using Putland's conditions for 1P waves, Ocle-Brown showed that the flare rate is equal to:

$$f = \frac{1}{S} \frac{dS}{d\xi} = -\frac{\mathbf{e}_u \cdot \nabla |\nabla u|}{|\nabla u|}. \quad (16)$$

Here  $\mathbf{e}_u$  is the unit vector in the direction of  $\nabla u$ . See Appendix A for his derivation.

Another identity for the flare metric can be found using logarithmic differentiation:

$$f = \frac{1}{S} \frac{dS}{d\xi} = \frac{d}{d\xi} \ln S \quad (17)$$

By rearranging the right-hand side of eq. (17) the cross-sectional area  $S$  through the domain can be calculated to be:

$$a_f = e^{\int f d\xi}. \quad (18)$$

Because this involves integrating  $f$  down a  $\xi$  path,  $a_f$  can be thought of as the comparative change in cross-sectional area (relative to the start geometry) that a 1P wave *feels* as it propagates through a domain. Notably, it can differ from the physical change in cross sectional area though a domain because wavefronts may not align with the cross-section of a domain. In this dissertation  $a_f$  is therefore referred to as the 'Felt Area'.

## 4. Methodology

The primary methodology for this dissertation is to use FEA to develop a concrete implementation of Oclee-Brown's proposed waveguide metrics, allowing them to be explored and analysed by studying several test case geometries.

### 4.1 Finite element analysis – FEA

In complex geometries, it can be very difficult or sometimes impossible to find an exact mathematical solution to a PDE which satisfies the domain shape and boundary conditions. Numerical methods are an alternative tried-and-tested method for solving PDEs that are appropriate when a domains geometry is complicated. They are widely used in many areas of engineering and physics.

FEA is a numerical technique which discretises a complex continuous problem into many elements which can be solved collectively using linear algebra, usually by a computer. Zienkiewicz, Taylor, & Zhu (2013) describe FEA as a general discretization procedure of continuum mechanics problems posed by mathematically defined statements. In FEA just the domain in which the PDE is solved over is discretised, so the finite element method is best suited for interior problems like cavities and ducts. At the end of the duct an impedance condition or a perfectly matched layer (PML) can be used to absorb the outward propagating sound wave and prevent unphysical reflections. Another method is to couple the finite element mesh to a boundary element mesh that models the radiation.

The FEA algorithm works by minimizing the error between the exact solution to a PDE and its boundary conditions and an approximate solution defined on a mesh. FEA can be used to compute the solution to many different PDE's including Laplace's equation  $u$ , which means the quantities required for computing Oclee-Brown's waveguide metrics are readily available.

Finite element analysis can become computationally expensive as the number of elements, nodes, and degrees of freedom increases to model more complex geometry. When simulating Helmholtz problems, a certain ratio of element size compared to wavelength needs to be maintained in order to maintain accuracy. This causes the number of elements required to rise with the cube of frequency in 3D. This requirement does not apply to solutions of Laplace's equation because it is non-oscillatory and does not have a notion of 'frequency'. This is one of the advantages of the proposed methodology – the absence of wavelengths within the Laplace solution makes it much cheaper to calculate and make metrics on it smoother. The disadvantage is that it is not the PDE that sound behaves according to.

### 4.1.1 Meshes

A mesh is a way of dividing the domain into many smaller segments. This makes interpolation of the solution far more straightforward and codes more versatile. Meshes are usually constructed of two numerical arrays: a nodes array which stores the node locations in global coordinates, and an element connectivity array which contains the indexes of all the nodes in each element. Each element can have shared nodes which means a complex geometrical shape can be represented by many interconnected elements.

### 4.1.2 Shape functions and element shapes

Shape functions are used to interpolate the values in-between the nodes of an element, including position within a deformed element, hence the term ‘shape’. The type of shape function or interpolation is related to the shape and size of the element, which range from simple 1D linear elements to complex high order 3D elements.

Figure 6 shows an example linear quadratic element with the local coordinate system denoted as  $(\eta, \varepsilon)$ . Shape functions are usually defined in a local coordinate system which typically ranges from -1 to 1 at each boundary of the element with 0 being the centre. Using a local coordinate system means the shape functions are always the same for the same type of element, as the local coordinates are independent of the global geometry of the element.

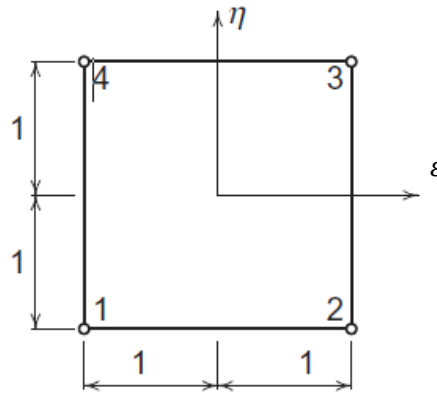


**Figure 6: Example local coordinate system for a 2D linear quadratic element. (reproduced from Zienkiewicz, Taylor, & Zhu, 2013)**

Figure 6 shows a 2D linear quadratic element. Its shape functions are:

$$\begin{aligned} N_1 &= \frac{1}{4}(1 - \varepsilon)(1 - \eta), & N_2 &= \frac{1}{4}(1 + \varepsilon)(1 - \eta), \\ N_3 &= \frac{1}{4}(1 + \varepsilon)(1 + \eta), & N_4 &= \frac{1}{4}(1 - \varepsilon)(1 + \eta). \end{aligned} \quad (19)$$

These shape functions are an example of Lagrangian polynomial interpolation, meaning they have a value of 1 at their own node and 0 at all the other nodes.

The shape functions can be used to interpolate any value at the nodes to a point in or around the element, including the global coordinates themselves. The basis for this parametric mapping is

$$f = \sum_a N_a f_a, \quad (20)$$

where  $f \in \{x, y, z, p, u\}$ .  $N_a$  are the shape functions on each node for a point defined in the local element coordinate system. Eq. (20) therefore shows how a coordinate can be mapped from the local element coordinate system to the global coordinate system.

#### 4.1.3 Calculating the gradient over an FEA mesh

To calculate the gradient of a function defined at the nodal coordinates on a mesh the derivatives of the shape functions with respect to the global coordinates must be known. In two dimensions this transformation is

$$\begin{bmatrix} \frac{\partial N_a}{\partial x} \\ \frac{\partial N_a}{\partial y} \end{bmatrix} = J^{-1} \begin{bmatrix} \frac{\partial N_a}{\partial \varepsilon} \\ \frac{\partial N_a}{\partial \eta} \end{bmatrix} \quad (21)$$

Where  $\partial N_a / \partial \varepsilon$  and  $\partial N_a / \partial \eta$  are the partial derivatives of the shape functions with respect to the local coordinates and  $J$ , the Jacobian, is the partial derivative of the global coordinates with respect to the local coordinates (Zienkiewicz, Taylor, & Zhu, 2013):

$$J = \begin{bmatrix} \frac{\partial x}{\partial \varepsilon} & \frac{\partial x}{\partial \eta} \\ \frac{\partial y}{\partial \varepsilon} & \frac{\partial y}{\partial \eta} \end{bmatrix} \quad (22)$$

$J$  is therefore used to relate vectors in each coordinate system.

The gradient of a scalar  $f_a$  defined on the nodes is calculated as

$$\nabla f(x, y) = \sum_a f_a \nabla N_a(x, y). \quad (23)$$

Gradients may be discontinuous at element edges where different shape functions meet, but this is also where it is necessary to evaluate the gradient to get node values for subsequent interpolation for evaluation of the metrics. As a workaround, the nodal gradient values calculated from each element are averaged over each node to form a global gradient matrix that can be interpolated over the entire mesh.

#### 4.1.4 Finite element mesh types

For this project the finite element method was used to simulate both Laplace's equation and the Helmholtz wave equation using the PAFEC FEA package (PACSYS Ltd, 2008).

The PAFEC FEA solver used supports simulations of Laplace's equation on 2D meshes, 3D meshes, and shell meshes. The latter are a manifold of infinitely thin 2D elements in a 3D space. This meant it was also possible to compute the waveguide performance metrics ( $s$ ,  $f$ , and  $a_f$ ) over any of these types of mesh because the metrics are all functions of  $u$ , the solution to Laplace's equation.

A shell mesh is useful in certain situations where a 3D geometry can be well approximated by an infinitely thin domain using 2D elements in a 3D space. This can significantly reduce the number of degrees of freedom for the problem and lower the computation time. Conveniently, the thin nature of much of the geometry in this project meant that it was a suitable approximation, so shell meshes could be used.

The Helmholtz wave equation could be computed over 2D and 3D meshes but not on shell meshes. 3D simulations of the wave equation take significantly more computational power, both because a separate simulation is performed for each frequency and because there are many more degrees of freedom in a model with 3D elements than 2D elements.

The Helmholtz wave equation simulations in this project did not model any nonlinearities or viscous losses. These losses could have a significant effect on the performance of a physical waveguide particularly at high SPL or if the geometry is extremely thin.

## 4.2 Tracing streamlines

Streamlines are used in many different aspects of engineering, a common example is simulating flow in groundwater, oil, and gas reservoirs. For this research streamlines of  $\nabla u$ , the gradient of the solution to Laplace's equation, were required as integration of  $\xi$  down the traced streamlines meant quantities such as  $a_f$  could be calculated (see Eq. (18))

The general concept of tracing streamlines is to iteratively step through a domain using the vector quantity sampled at each step to direct the algorithm towards its next sampling position. This is similar to how ordinary differential equations are sometimes solved numerically, which means the same techniques, such as the Forward Euler method and the Runge-Kutta (RK4) method, are applicable to streamline tracing.

To trace a vector quantity, first a starting coordinate and a step size must be defined. A smaller step size usually traces a more accurate streamline but with more steps which takes longer. So, like many numerical techniques, there is a trade-off to between computation time and accuracy.

### 4.2.1 Forward Euler method

A simple algorithm is the first order forward Euler technique. On each step the algorithm samples the vector field once and then moves forward in the direction of the vector with the given step size. To trace streamlines in 3D, the Forward Euler method is

$$(k, l, m) = f(x_n, y_n, z_n) \quad (24)$$

$$\begin{aligned} x_{n+1} &= x_n + hk \\ y_{n+1} &= y_n + hl \\ z_{n+1} &= z_n + hz \end{aligned} \quad (25)$$

where  $h$  is the step size and  $f(x, y, z)$  is the 3D function being traced. If the step size is small enough the Forward Euler method can give satisfying accuracy.

### 4.2.2 RK4 method

Another method is the Runge-Kutta 4 method, which is part of the Runge-Kutta family of iterative techniques. The RK4 method is a popular choice for solving ODE's as It uses the weighted average of the vector quantity at four sample points to decide where the next step should be.

For this project the RK4 method was modified to work in three dimensions for streamline tracing. Eq. (26) demonstrates how the sample point locations are calculated and Eq. (27) shows how the algorithm uses the weighted values to step forward to the next iteration.

$$\begin{aligned} (k_1, l_1, m_1) &= f(x_n, y_n, z_n) \\ (k_2, l_2, m_2) &= f\left(x_n + h\frac{k_1}{2}, y_n + h\frac{l_1}{2}, z_n + h\frac{m_1}{2}\right) \\ (k_3, l_3, m_3) &= f\left(x_n + h\frac{k_2}{2}, y_n + h\frac{l_2}{2}, z_n + h\frac{m_2}{2}\right) \\ (k_4, l_4, m_4) &= f(x_n + hk_3, y_n + hl_3, z_n + hm_3) \end{aligned} \quad (26)$$

where each step is taken by

$$\begin{aligned} x_{n+1} &= x_n + \frac{h}{6}(k_1 + 2k_2 + 2k_3 + k_4) \\ y_{n+1} &= y_n + \frac{h}{6}(l_1 + 2l_2 + 2l_3 + l_4) \\ z_{n+1} &= z_n + \frac{h}{6}(m_1 + 2m_2 + 2m_3 + m_4) \end{aligned} \quad (27)$$

The RK4 method has the advantage over the Forward Euler method that it is more accurate with the same number of steps because the function is approximated by a smooth curve instead of linear sections.

### 4.2.3 Tracing streamlines through an FEA mesh

To trace streamlines through the FEA mesh the discrete nodal data which approximates the continuous function  $\nabla u$  over the domain was interpolated to each streamline sample point. This meant a smooth path could be traced through the domain.

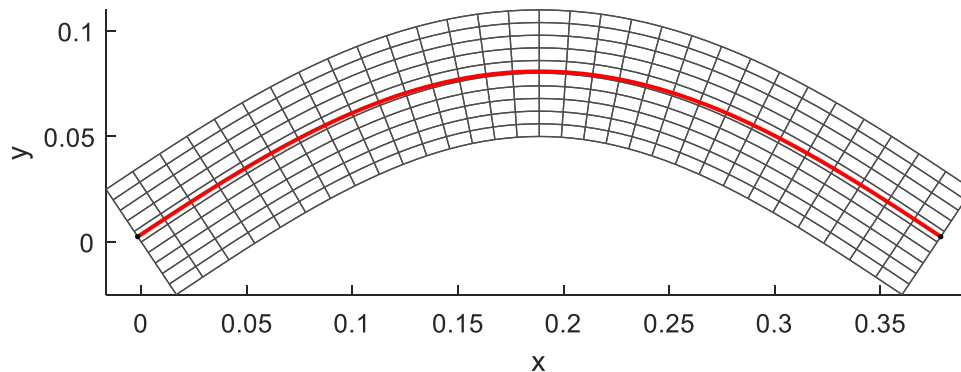


**Figure 7: Example streamline in red traced through an FEA mesh shown in black**

Figure 7 shows an example streamline traced through an arc shaped mesh. The streamline tracing algorithm samples the mesh at points defined in the global coordinate system. This means that for each streamline sample point, first the element which contains the sample point needs to be found. The global coordinate was then inverse mapped to the local coordinate of the point within the element. Once this was known, the vector values defined on the nodes of the element were interpolated using the shape functions and local coordinates. Figure 8 shows a flow map of the streamline tracing loop which continues until a stopping criterion is met, for example the streamline falling off the mesh.

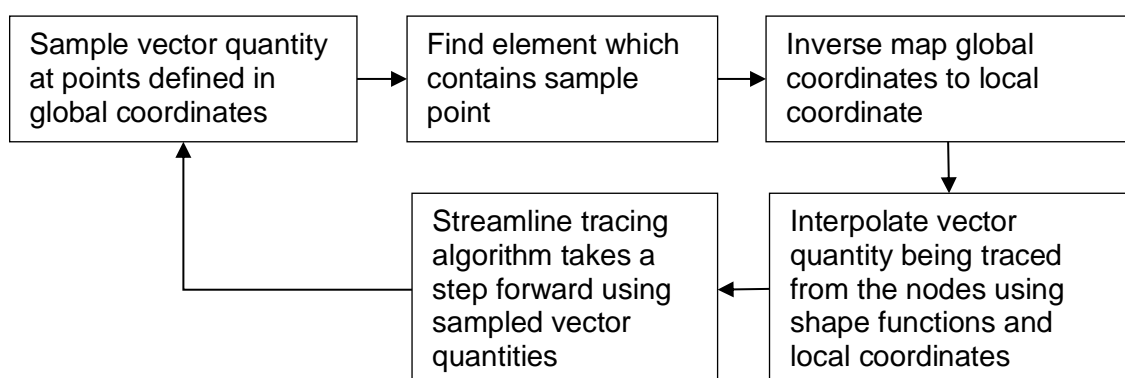


**Figure 8: Flow map showing steps in tracing streamlines through a mesh**

This technique was used to trace streamlines of the steepest ascent of  $\nabla u$  through an FEA mesh.

#### 4.2.4 Inverse coordinate system mapping

Inverse mapping can be done analytically by re-arranging the shape functions to find the local coordinates. This usually requires finding the roots of a polynomial, the size of which depends on the number of nodes and dimensions in the element. But this is not always efficient. Silva, Le Riche, Molimard & Vautrin (2007) wrote that “In applications where the shape functions are more complex than QUAD4 elements, an analytical inversion of the shape functions may become too tedious to be carried out”. Hence, an iterative approach is used instead.

To inverse map using numerical methods first an initial guess of the local coordinates is made, and then the error between the goal global coordinate and the forward mapped global coordinate is reduced iteratively. The forward error function to be minimised is:

$$f_{\varepsilon} = \delta_x^2(\vec{\varepsilon}) = (x^T(p) - N_a(\vec{\varepsilon})x_a)^2, \quad (28)$$

where  $x^T(p)$  are the target coordinates and  $\vec{\varepsilon}$  are the unknown local coordinates. Silva et al. (2007) suggest using a Newton-Raphson method to minimise the mapping error. This method requires the Hessian matrix of  $f$ , which is all combinations of the second order partial derivatives in each dimension. The iteration step is then:

$$\Delta \vec{\varepsilon} = \frac{1}{2} \mathbf{H}^{-1} \vec{g}, \quad (29)$$

where  $\mathbf{H}$  is the Hessian matrix of  $f$ , and the individual partial derivatives can be computed from Eq. (28). This carries on iteratively until:

$$g_i = \frac{\partial f}{\partial \varepsilon_i} = 0 \quad (30)$$

is satisfied at the solution point.

For this research project the Newton-Raphson numerical technique was used to inverse map the coordinates because it is a flexible method that works with complex high order elements. Fortunately, the MATLAB symbolic maths toolbox used has special algebraic tools for computing the Hessian matrix, since with complex high order 3D elements it becomes rather large and can be very time-consuming to work out by hand.

#### 4.2.5 Mapping data between nodes and streamlines

Once the streamlines were traced, it was necessary to be able to map data from the nodes onto the streamline points and vice-versa. By constructing a global shape function matrix  $N$  which stores the fully defined shape functions for each traced streamline point, a mapping of large sets of data between the nodes and streamlines was possible with a single matrix operation

$$N \times \mathbf{f}_n = \mathbf{f}_s \quad (31)$$

where  $\mathbf{f}_n$  is a vector of data defined on the nodes and  $\mathbf{f}_s$  is a vector of the data defined on the traced streamline points. Using a global shape function matrix also allowed for easy reverse mapping of data from the streamline points back to the nodes. However, for the reverse mapping to work the inverse of the global shape function matrix had to be stable and not rank deficient. This was achieved by ensuring there were enough streamline points in each element so that each node was well defined in  $N$ .

### 4.3 Numerical calculus techniques

To compute the metrics in section 3.3, it is necessary to perform calculus operations on functions defined on the streamlines. The discrete format and uneven spacing of the streamline data meant numerical calculus techniques had to be used. This section discusses some of the different numerical differentiation and integration methods.

#### 4.3.1 Cumulative trapezoid numerical integration

The trapezoidal algorithm for integration approximates the area under a curve by finding the area of a trapezium from point  $(a, f(a))$  to  $(b, f(b))$

$$\int_a^b f(x) dx \approx \frac{1}{2}(b-a)(f(a) + f(b)) \quad (32)$$

The MATLAB function `cumtrapz` approximates the cumulative integral using the trapezoidal method in Eq. (32) for each interval and then calculates the cumulative sum.

The trapezium method has the disadvantage that a continuous curve is approximated by linear sections. By reducing the interval size a better accuracy can be achieved, but in the case of streamlines this means tracing more points, which may take significantly longer.

#### 4.3.2 Central difference numerical gradient

The central different numerical gradient algorithm is a numerical technique for differentiation.

The central difference formula works by looking at the slope of the line formed from looking at data points either side of the point in question.

$$\frac{df(a)}{dx} \approx \frac{f(a+h) - f(a-h)}{2h} \quad (33)$$

Again, a better accuracy can be achieved by having a smaller interval size. The MATLAB function `gradient` uses the central difference formula to approximate the gradient.

## 4.4 Metric calculation methods

To calculate Ocle-Browns metrics the FEA package PAFEC was used to compute the solution to Laplace's equation,  $u$ , over a domain. The nodal data was then imported to MATLAB for further processing and manipulation. The entrance and exit of the waveguide are represented by Dirichlet boundary conditions with values  $u = 0$  and  $u = 1$  respectively. Thus, the Laplace solution climbs from zero at the entrance of the waveguide to one at the exit, and the streamlines as lines of steepest ascent. For computing the stretch metric  $s$  the gradient operation in eq. (13) was done using the mesh gradient calculation technique discussed in section 4.1.3

The flare metric  $f$  could be calculated over an FEA mesh using two different techniques, the nodal method, and the streamline method. Both methods follow Eq (16). The difference is that nodal method computes the gradient operations using the approach shown in section 4.1.3, whereas the streamline method maps  $u$  to the streamlines and then uses the central difference numerical gradient technique discussed in section 4.3.2. The values can then be mapped between the nodes and streamlines using a global shape function matrix  $N$  (see section 4.2.5). For the streamline method the  $e_u$  unit vector term is not needed as the streamlines already follow  $\nabla u$ .

For two-dimensional flat meshes the differences in the two techniques were insignificant, but for some three-dimensional problems using a shell mesh the streamline method proved more accurate because it avoids the possible calculation error from taking the gradient of a function over a coarse shell mesh. This effect is explored in section 6.1.5. For this reason, the streamline technique was used to compute  $f$  in all of the examples.

The integration in Eq. (18) for computing the felt area metric was performed down the streamlines from the entrance to the exit of the geometry using the cumulative trapezoid numerical integration technique discussed in section 4.3. The values were then mapped between the nodes and the streamline points using the global shape function matrix  $N$ .

## 5. Understanding the metrics

This section first explores calculating the metrics proposed by Ocle-Brown on several test case geometries. It then investigates methods for further manipulating the metrics using traced streamlines which follow the steepest ascent of the vector field  $\nabla u$ , the gradient of the solution to Laplace's equation.

Oclee-Brown's metrics measure how much a Laplace solution computed for a specified geometry deviates from Putland's (1993) 1P conditions (eq. (10) and (11)). They therefore indicate how effective regions of a domain are at supporting 1P wave propagation. To help avoid confusion, it is necessary to clarify that in this dissertation the terms "metric error" and "error in the metrics" are used to describe how the metrics suggest a geometric deviation from Putland's conditions for 1P wave propagation. These terms are not used to imply that there is error in the calculation of the metrics themselves.

To make this document clearer to the reader, when possible different colours have been used to plot the separate waveguide metrics. Table 1 is a guide which shows which colours represent which metrics or values.

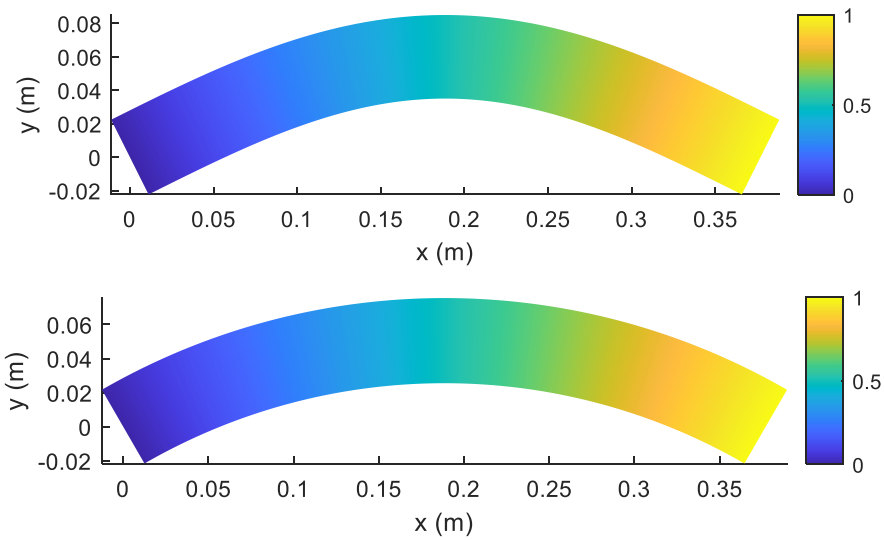
**Table 1: Waveguide metric colour guide**

	$u$ – solution to Laplace's equation
	$f$ – flare
	$s$ – stretch (also used for $\nabla u$ )
	$a_f$ – felt area (also used for $t_c$ )

## 5.1 Test geometries

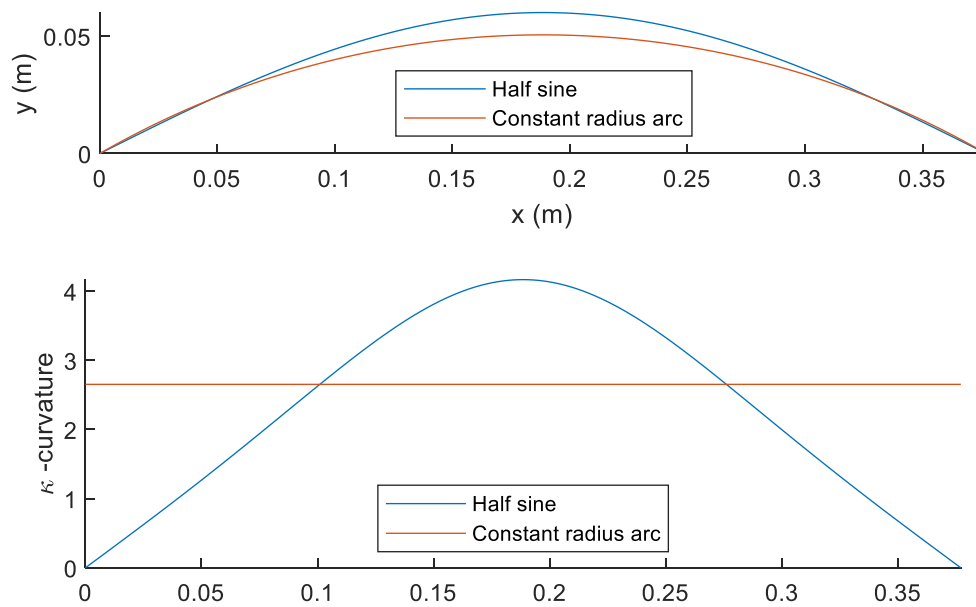
Several test case geometries are used throughout this dissertation. Looking at different geometries helps to clearly illustrate what the metrics signify and to explore the effectiveness of the waveguide optimisation method in different situations. This section introduces the test case geometries.

Figure 9 shows the 'half sine' and the 'constant radius arc'. Both shapes are in-plane curves with no expansion in width of the channel. Both geometries have an entrance around  $x = 0$  and exit around  $x = 0.38(m)$ . The channels were created by adding 50mm of thickness to the centre line (25mm in the +/- normal directions).



**Figure 9: solution to Laplace's equation  $u$ , top: 'half sine', bottom: 'constant radius arc'**

The initial lines used to build the geometry are shown in the top of Figure 10 and the curvature  $\kappa$  is shown below.



**Figure 10: half sine and constant radius arc comparison, top: central line geometry, bottom: curvature  $\kappa$**

The signed curvature  $\kappa$  for a parametric equation is (Kreyszig, 1991)

$$\kappa = \frac{\frac{dx}{dt} \frac{d^2y}{dt^2} - \frac{dy}{dt} \frac{d^2x}{dt^2}}{\left( \left( \frac{dx}{dt} \right)^2 + \left( \frac{dy}{dt} \right)^2 \right)^{\frac{3}{2}}} \quad (34)$$

where  $t$  is a parametric representation of the curve.

The 'half sine' is constructed from half of a sine curve, which means the curvature starts at zero, has a maximum in the centre of the curve and then decreases to zero at each end. In contrast the 'constant radius arc' has a constant (non-zero) curvature throughout the curve because it is an arc of constant radius. These subtle differences have interesting effects on the waveguide metrics and make them a good test case for investigating the effect of duct curvature.

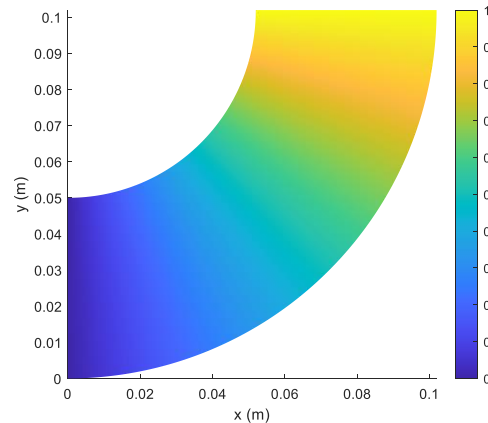


**Figure 11: Solution to Laplace's equation  $u$  on the '90-degree bend' geometry**

Figure 11 shows  $u$  on the 90-degree bend geometry. The 90-degree bend is a constant radius arc which turns a full 90-degrees. The entrance is at  $x = 0$ , and the exit is at  $y = 0.1$ . The 90-degree bend is similar to the constant radius arc except that it is shorter, wider, and turns a larger angle.

Figure 12 shows the S-bend geometry which is constructed of two arcs of constant radius which bend in opposing directions. It has no expansion in area from the entrance to exit, so no flare is expected. But each bend causes a change in the relative pathlength through the domain, which make it a good test case for the stretch metric  $s$ . The entrance is on the boundary at  $x = 0$ , and the exit is on the boundary around  $x = 0.13$  (m).

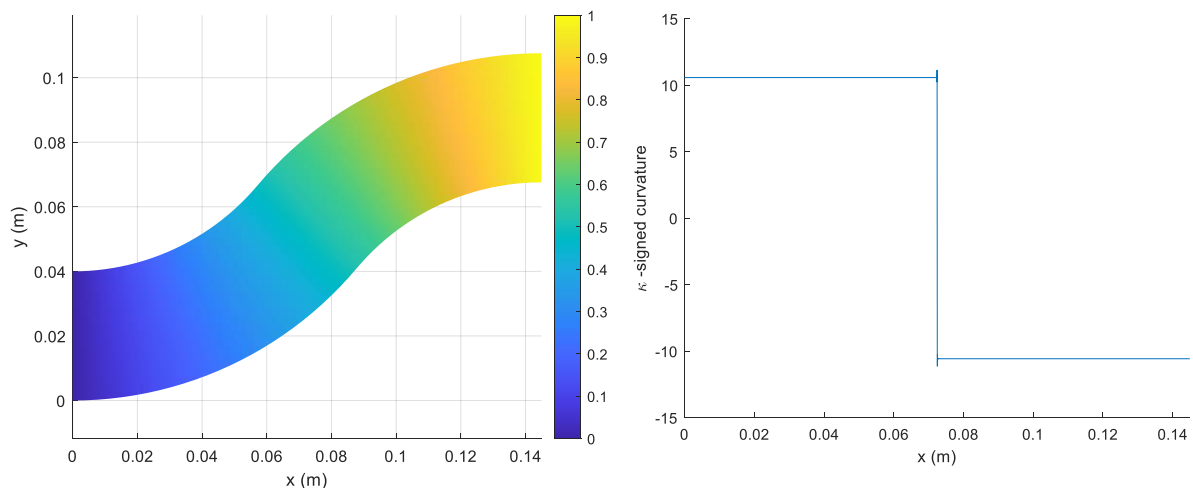


**Figure 12: ‘S-bend’ Geometry, Left: solution  $u$  to Laplace’s equation, Right: signed curvature of central line**

The right side of Figure 12 is the curvature of the central line through the S-bend geometry. It is constant for each arc section, and it rapidly changes at the transition point between the two arcs. The curvature was calculated using piecewise polynomial numerical differentiation, which is why there are some small artifacts (overshoots) in the curvature at the transition point.

Figure 13 is a plot of  $u$  on the wedge geometry and channel wedge geometry. The wedge geometry has an arc shaped entrance and exit, starting at  $x = 0$  and  $x = 0.065$  respectively. The two connecting side walls are straight and perpendicular to the entrance and exit surfaces. The wedge geometry is a 2D slice of a cylindrical waveguide and the perpendicular distance from entrance to exit is constant everywhere, therefore there is no change in relative pathlength through the geometry. There is however a large expansion in area from entrance to exit.

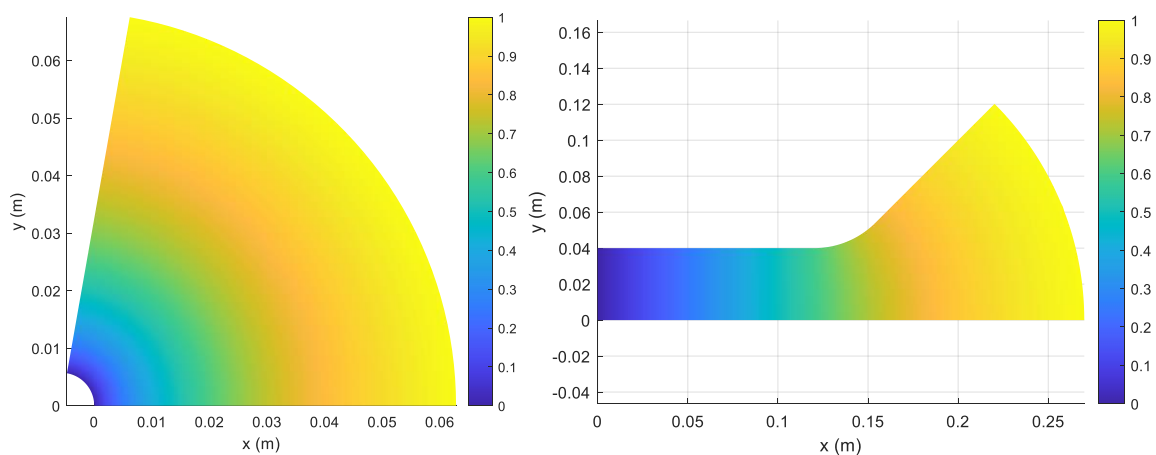


**Figure 13: solution to Laplace’s equation  $u$ , left: ‘wedge’ geometry right: ‘channel-wedge’ geometry**

The channel-wedge geometry has a constant thickness for the first section (like a channel of constant thickness) and then an expansion in area for the second section (like a 2D wedge-shaped horn). These properties mean it is a useful test case for investigating the flare metric  $f$ . The entrance is on the boundary at  $x = 0$ , and the exit is on the curved boundary which starts at  $(0.27, 0)$ . The initial channel section can support 1P plane wave propagation and the wedge section can support 1P cylindrical wave propagation, but the area that joins them does not. This makes the channel-wedge shape an interesting test case because it attempts to convert sound waves from one 1P waveshape into another.

## 5.2 Stretch $s$

Stretch  $s$  measures the gradient of  $u$  as a proxy for wavefront propagation distance. However, whereas for a Helmholtz problem this could be related to the speed of sound, the gradient of  $u$  in the Laplace problems is rather arbitrary. The main thing that defines it is the length of the duct. Hence, relative stretch compared to a reference path is instead considered. Figure 14 shows  $u$  on the S-bend with 50 isolines of surfaces of constant  $u$  overlaid. The distance between the isolines is related to  $\nabla u$  and it illustrates how there is a steeper (higher)  $\nabla u$  close to the inside edge of each curve.

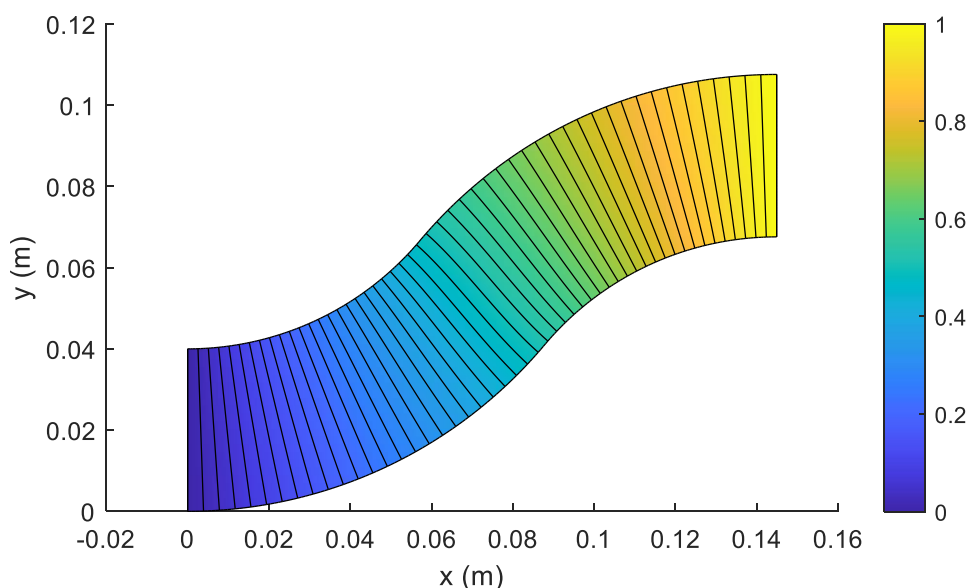


**Figure 14: solution to Laplace's equation  $u$  on s-bend with 50 isolines of surfaces of constant  $u$  overlaid**

To calculate the stretch  $s$  over a domain, a reference path through the domain is chosen. so that the relationship of arc length  $\xi$  to the solution to Laplace's equation  $u$  can be used to analyse the rest of the geometry. The rest of the domain is then compared to the reference  $\xi$  path, so depending on the  $\xi$  path chosen different values of  $s$  will be obtained, which may be greater or less than one depending on whether the path is shorter or longer (giving steeper or flatter gradients respectively).

Streamlines which trace the steepest ascent of  $\nabla u$  were traced through the domain, starting on the entrance boundary where  $u = 0$ . The streamlines were traced through the FEA mesh using the RK4 algorithm and the methods outlined in section 4.2.

Because the streamlines follow  $\nabla u$  they are  $\xi$  paths following Putland's conditions (1993). Figure 15 shows 60 streamlines of  $\nabla u$  traced through the S-bend geometry.

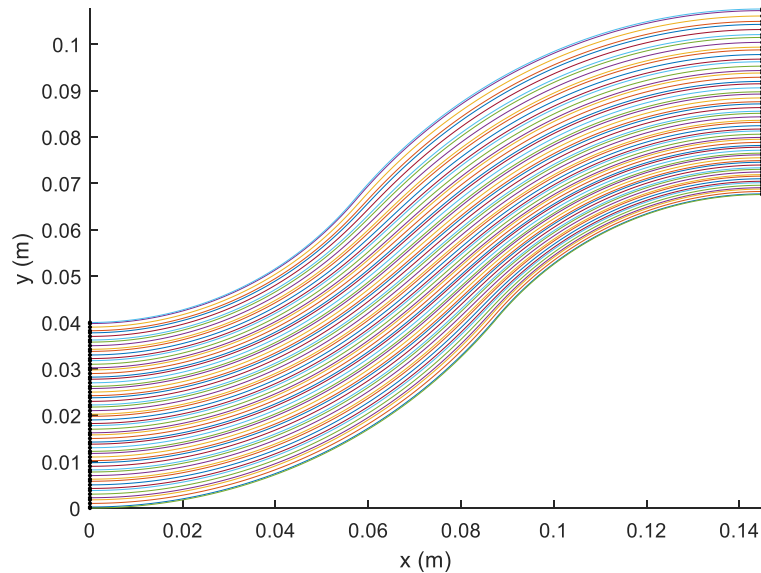


**Figure 15: 62 Streamlines of the vector field  $\nabla u$  traced through the S-bend geometry**

By definition, a  $\xi$  path is always perpendicular to a surface of constant  $u$  and follows  $\nabla u$ , this means that a rigid edge boundary parallel to  $\nabla u$  is a  $\xi$  path. Because of this, a boundary edge makes a straightforward initial choice of reference path.

The arc length  $\xi$  of the chosen reference path was found by integration. This value was then mapped to all the nodes in the domain with matching  $u$  (since Putland defined path-length  $\xi(u)$  to be a function of  $u$ ) and the Stretch metric was then calculated as  $|\nabla \xi|$ .

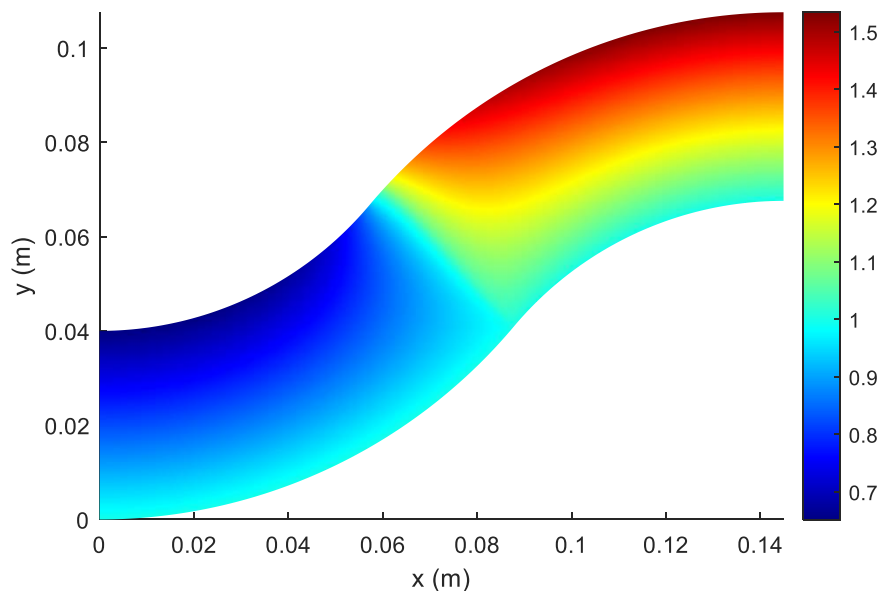


**Figure 16: Stretch  $s$  on the S-bend geometry using the bottom boundary as the reference  $\xi$  path**

In Figure 16, the bottom curved boundary which starts at  $(0,0)$  was used as the reference  $\xi$  path to calculate  $s$ . Therefore, on this boundary  $s = 1$ , and indicates no error in the relative pathlength. For the first bend in Figure 16 the reference edge is the outside edge of the curve.

On the opposing boundary, the inside edge starting at  $(0,0.04)$ ,  $s$  is around 0.7 which indicates that the relative pathlength is around 0.7 times shorter than the reference edge.

Then, vice-versa, on the second part of the geometry when the channel bends in the other direction. Here,  $s > 1$  indicates that the relative pathlength is longer than the reference edge.

To help bring more understanding to the metric it was useful to study some other geometries as well. Figure 17 is the stretch metric comparing the 'half sine' and 'constant radius arc' geometries. In both examples the reference edge chosen is the top edge so  $s = 1$  on this boundary.

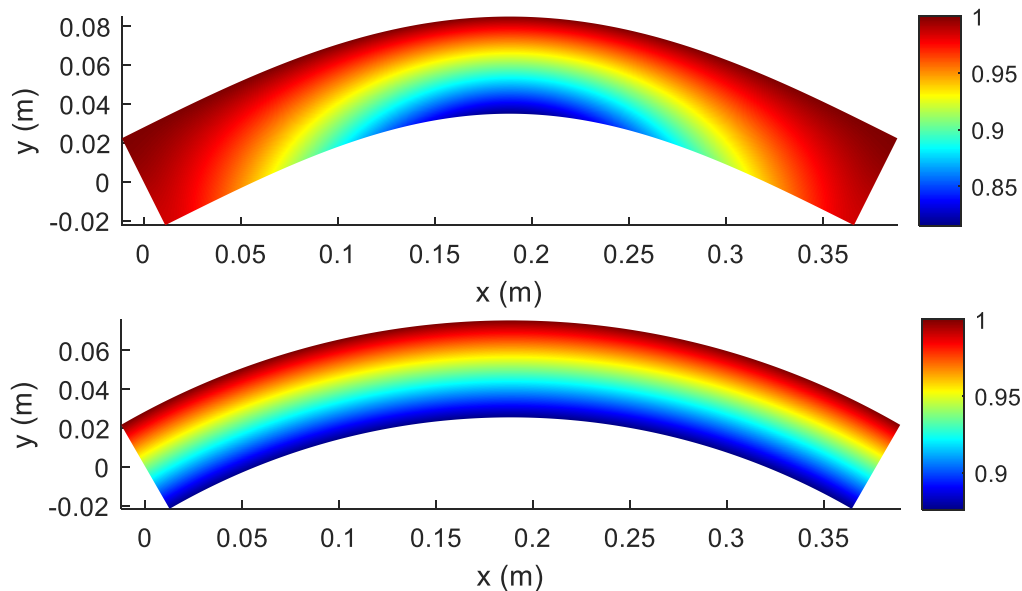


**Figure 17: stretch metric  $s$  with top boundary used as the reference edge, Top: Half sine, Bottom: Constant radius arc**

The constant radius arc has constant stretch error through the geometry and the half sine has higher values of stretch error concentrated around the middle of the domain where the curvature is highest (see Figure 10). This is logical as the pathlength difference is largest when there is most curvature.

Figure 18 shows  $s$  on the wedge geometry, because the relative pathlength from entrance to exit is constant across the domain, there is no error shown in the metric.

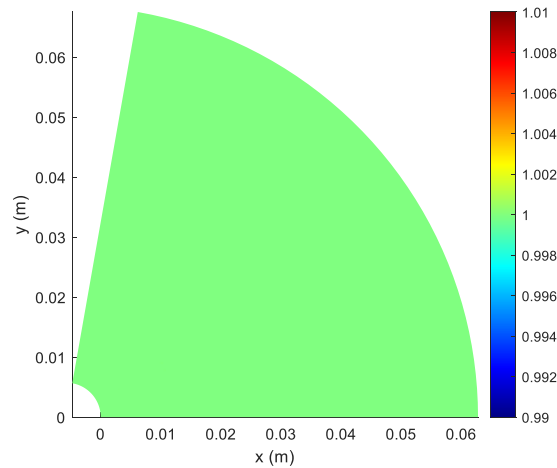


**Figure 18: stretch metric  $s$  on the wedge geometry**

### 5.3 Normalising stretch

It is far easier to add pathlength to a waveguide than it is to take it away – indeed this is what patent GP Acoustics patent EP3806086A1 and the other reviewed approaches provide methodologies for. For example, in Figure 16 the flat domain could be distorted somehow to add pathlength when  $s < 1$ , but a problem arises when the domain is too long, i.e. when  $s > 1$ , since no mechanism exists to take pathlength away. In other words, the stretch metric is most useful when it shows how much shorter part of the domain is than it should be, as the domain can then be modified to add pathlength to these regions to compensate. A method of normalisation is required that uses the longest part of the domain at each point as the reference  $\xi$  path.

#### 5.3.1 Minimum-normalised stretch $s_n$

By calculating the stretch metric multiple times using each of the traced rays as the reference  $\xi$  path and then taking the minimum calculated stretch value at each node a minimum-normalised stretch metric  $s_n$  was computed.

Essentially this method of normalisation means that an abstract reference  $\xi$  path is constructed, which is made up of sections of the streamlines with the longest relative pathlength or biggest  $d\xi/du$  in each region of the domain.

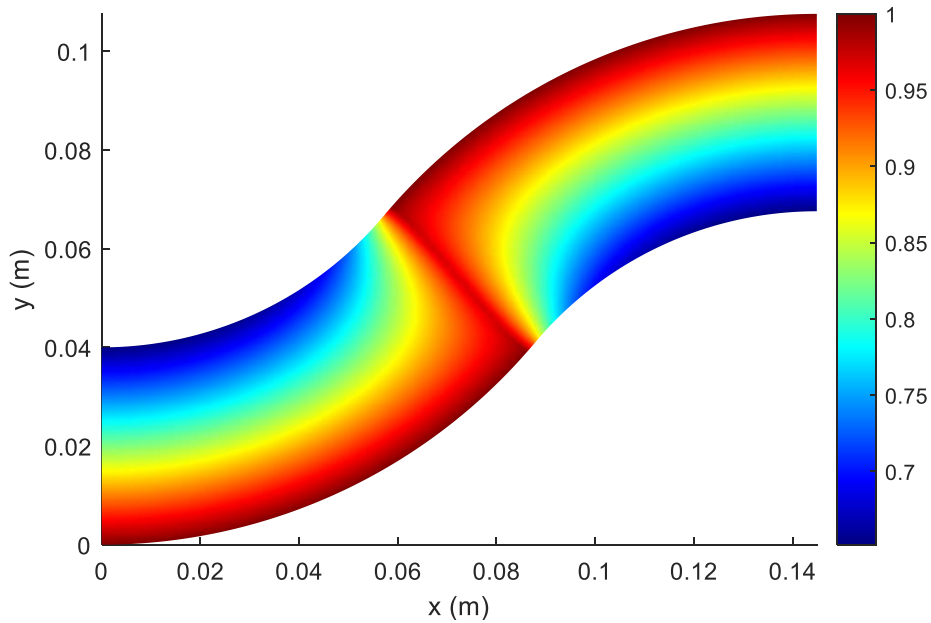


**Figure 19: Minimum-normalised stretch  $s_n$  on s-bend geometry**

Figure 19 shows the normalised stretch on the s-bend geometry. A maximum value of one is found on the outside edge of each curved section. This is where the reference path has fallen, since it was the maximal path length in Figure 16. This approach creates a useful result because pathlength can be added to the domain in areas where the metric is less than unity. It is interesting to note how the normalised stretch  $s_n$  fades to unity in the middle at the intersection between the two curved sections.

It can also be revealing to look at the metrics on the streamlines. The left side of Figure 20 shows 7 streamlines traced through the S-bend geometry, and the right side shows  $s_n$  on the streamlines plotted against  $u$ . Streamlines 1 and 7 are on the boundaries.

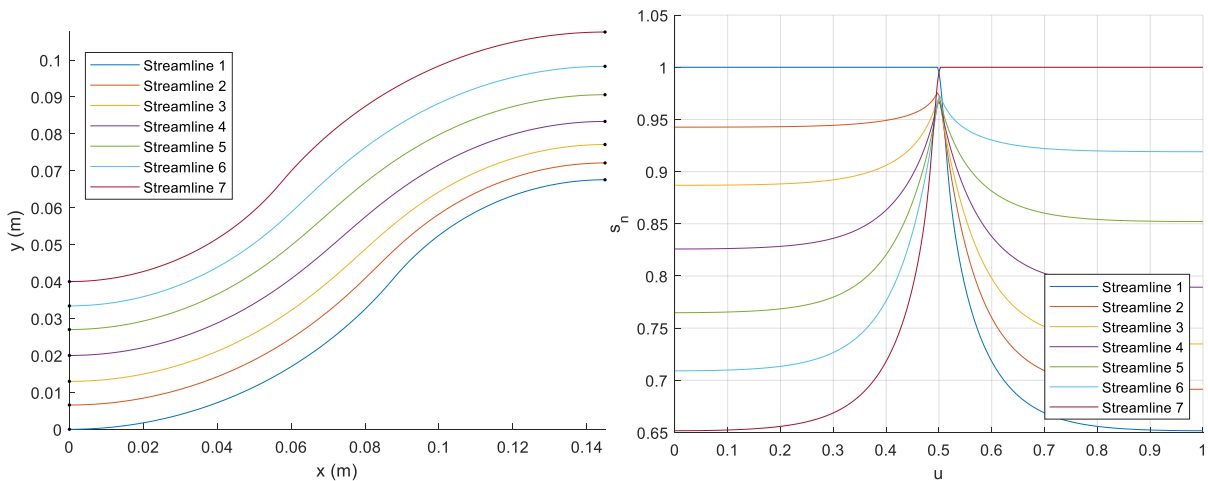


**Figure 20: S-Bend, left: 7 streamlines of  $\nabla u$ , right: normalised stretch  $s_n$  on streamlines vs the solution to Laplace's equation  $u$**

For the first half of the geometry streamline 1 has the longest relative pathlength so  $s_n = 1$  and for the second half of the geometry this switches to streamline 7. On the other streamlines which have a shorter relative pathlength  $s_n < 1$ .

Since the normalisation acts as a scaling, the ratio of the maximum and minimum values of stretch on a surface normal to the  $\nabla u$  (a wavefront) will always be the same regardless of it. For example, comparing the range of  $s$  on Figure 19 and Figure 16, the ratio of  $s$  between the top to bottom boundaries at  $x = 0.14$  is around 1.51 in both cases.

### 5.3.2 Average-normalised stretch $s_a$

By calculating the stretch reference to every streamline and calculating the average value on each node instead of the minimum, an average normalised stretch  $s_a$  could also be calculated.  $s_a$  is therefore created using an abstract reference  $\xi$  path which is constructed of sections of the streamlines which have the average relative pathlength through each region of the domain.

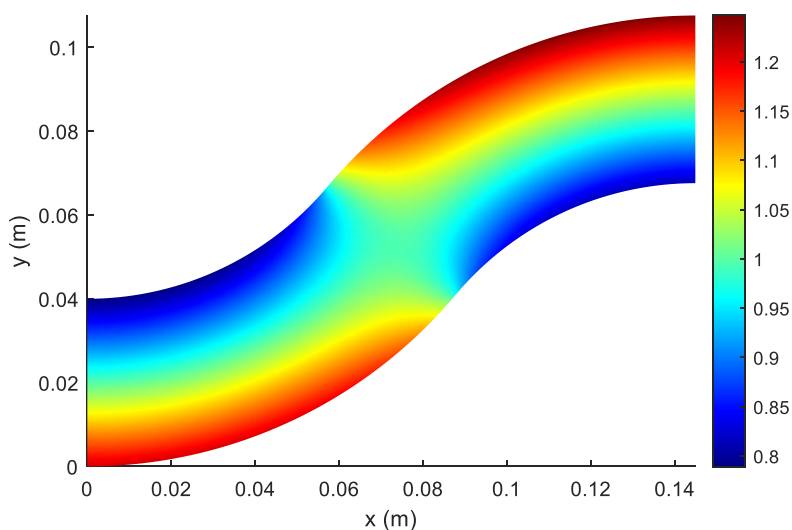


**Figure 21: Average-Normalised stretch  $s_a$  on S-Bend geometry**

Figure 21 show  $s_a$  for the s-bend geometry – note the different scale compared to Figure 19. The region with a value of one is now down the centre of each curved section and the metric indicates how much shorter or longer the relative pathlength is than this central path. This is less useful for waveguide optimisation, but it can be more intuitive in certain situations. For example, when trying to visually understand how the relative pathlength is changing through an intricate shape.

### 5.4 Cumulative required pathlength $\xi_r$

When using the minimum-normalised stretch  $s_n$  defined in section 5.3.1, the longest path through the geometry (the one that all other paths will be extended to mimic) is now a function

of the Laplace solution, not any simple property of the geometry. It is, therefore, useful to define a ‘cumulative required pathlength metric’  $\xi_r$ , that shows how much distance should have been travelled to reach this location, were 1P waves to be correctly supported.

$\xi_r$  can be found by integrating the normalised minimum stretch  $s_n$  down each streamline:

$$\xi_r = \int \frac{1}{s_n} d\xi. \quad (35)$$

$\xi_r$  is therefore a measurement of arclength which is referenced to the longest  $\xi$  path at each point through a domain and mapped to the rest of the domain using the relationship  $\xi(u)$ . Consequently, if there is no pathlength error in the domain then  $s_n = 1$  and  $\xi_r = \xi$ .

$\xi_r$  was computed by mapping  $s_n$  to the streamlines and then integrating using the cumulative trapezoid numerical integration technique discussed in section 4.3. The left-hand side of Figure 22 shows 6 traced streamlines through a 90-degree bend geometry and the right-hand side is a plot of  $\xi_r$  against  $\xi$  (the physical arc length of the streamlines).

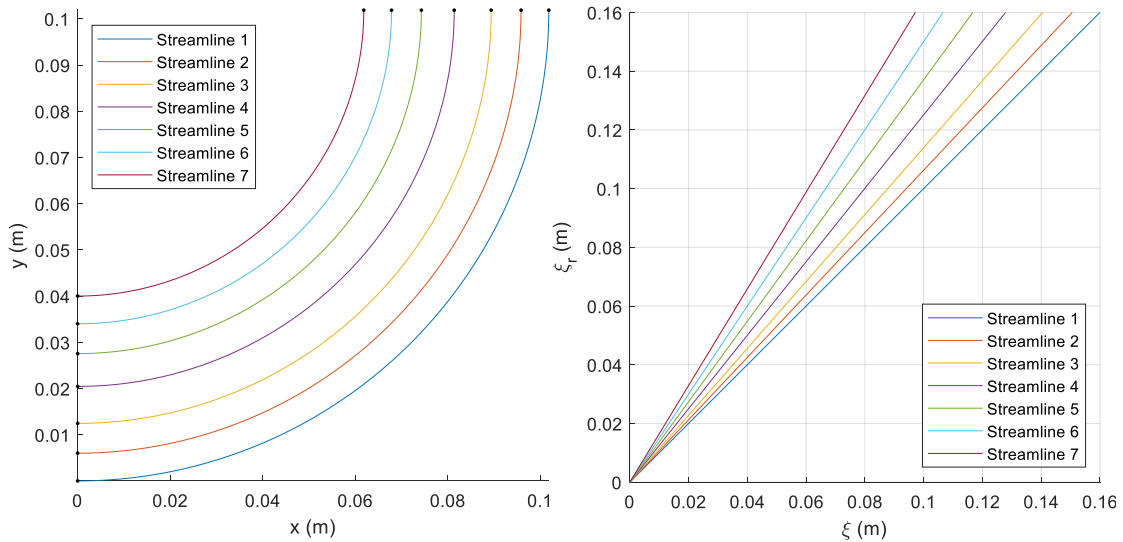


**Figure 22: 90Deg bend geometry - left: traced streamlines, right:  $\xi$  (arc length) vs  $\xi_r$**

$\xi_r$  could be interpreted as the cumulative “required” pathlength at each point down a streamline if the domain is to support 1P wave propagation. Streamline 1 in Figure 22 has the longest pathlength compared with the rest. This causes a 1:1 relationship between  $\xi_r$  and the physical arc length  $\xi$  throughout the domain. In contrast streamline 7 on the inside of the curve has a steeper gradient of  $\xi_r$  because it has the same cumulative  $\xi_r$  value even though it has less physical arc length  $\xi$ . All of the streamlines have the same total  $\xi_r$  length regardless of the domain shape.

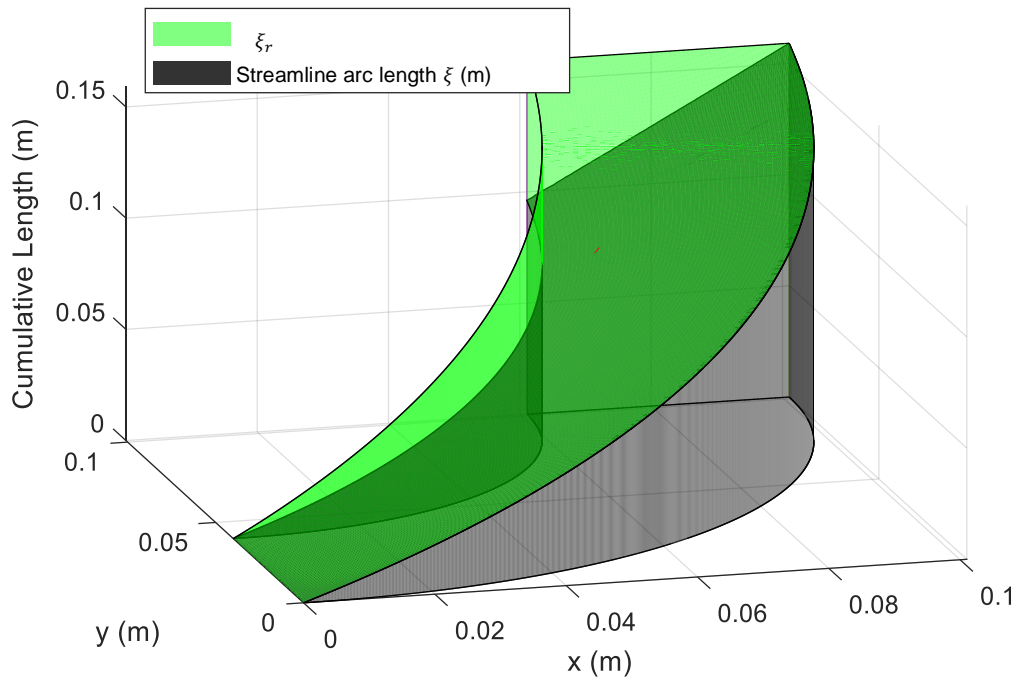


**Figure 23:**  $\xi_r$  and physical arc length  $\xi$  plotted in 3D for 90-degree bend geometry

$\xi_r$  on a 2D surface can also be visualised in 3D. Figure 23 is a plot of the cumulative arc length  $\xi$  and  $\xi_r$  for a 90° Bend geometry. The Green area in the plot is  $\xi_r - \xi$ , so it shows how much extra pathlength would need to be added if there was to be no pathlength error. It also illustrates how on the longest path through the domain  $\xi_r$  is equal to the physical arc length  $\xi$ , and in regions where the relative pathlength through the domain is shorter (in this case for the inside of the curve)  $\xi_r$  increases to compensate.

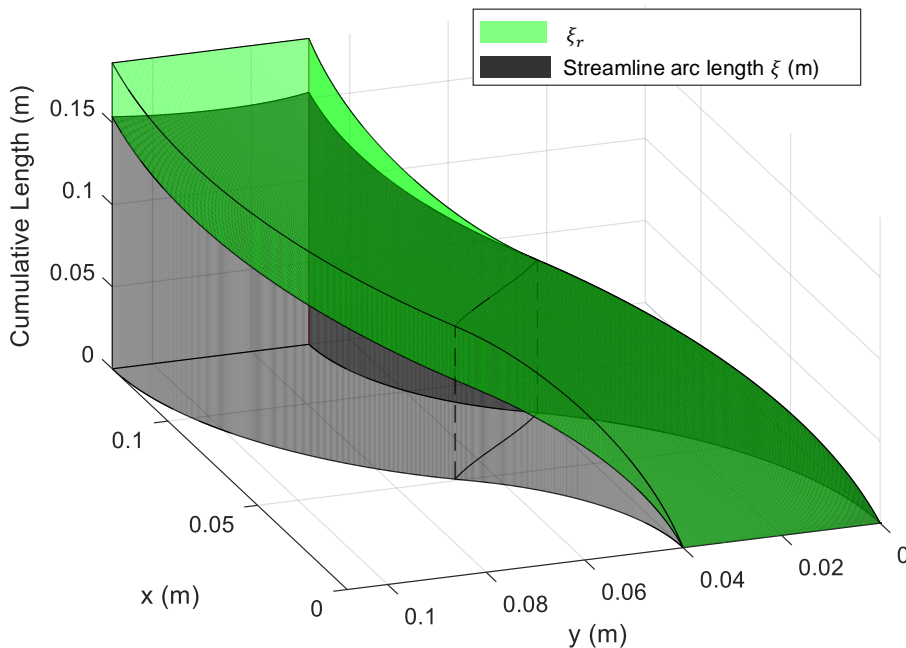


**Figure 24:**  $\xi_r$  and physical arc length  $\xi$  in 3D for s-bend geometry

Figure 24 is a similar 3D plot but for the S-bend. The dotted lines in the middle show where the geometry begins to bend the other way. On the first bend (starting at  $x = 0$ ) the longest

edge is on the right side (starts at  $y = 0$ ). Along this edge  $\xi_r = \xi$  and across the rest of the channel  $\xi_r > \xi$ .

In the second half of the s-bend the channel bends in the other direction and the reference edge (longest  $\xi$  path) is now on the left side. This causes  $\xi_r$  to increase to more than  $\xi$  across the entire width of the channel towards the end around  $x = 0.14$  (m).

## 5.5 Normalised required pathlength $\xi_n$

$\xi_r$  can also be normalised to one to create a new quantity  $\xi_n$  defined as:

$$\xi_n = \frac{\xi_r}{\max(\xi_r)} \quad (36)$$

This is an easier way of indexing position within the waveguide (as a 1P wave would experience) since it is bounded between zero at the entrance and one at the exit.  $\xi_n$  is similar to  $u$ , in fact, for a domain with no expansion, such as the 90-degree bend shown in Figure 25,  $\xi_n$  and  $u$  are the same.

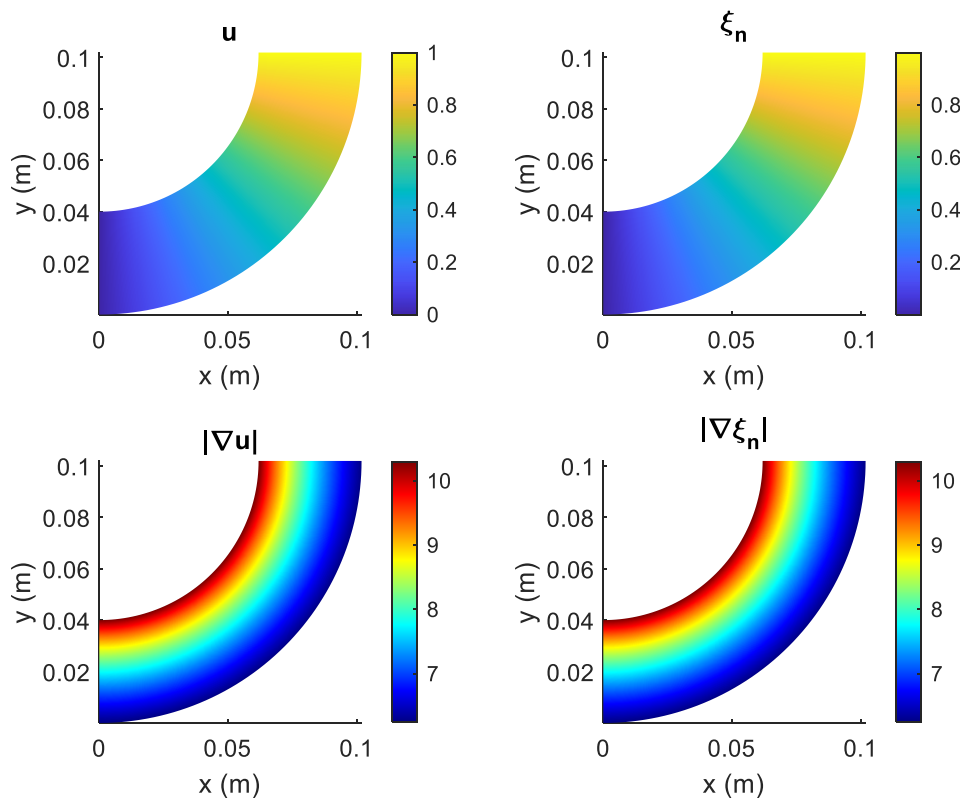


**Figure 25: Comparison of  $u$  and  $\xi_n$  on 90-degree bend geometry.**

However, in a domain which has expansion in cross sectional area, such as the wedge geometry in Figure 26, there is a significant difference between  $\xi_n$  and  $u$ .

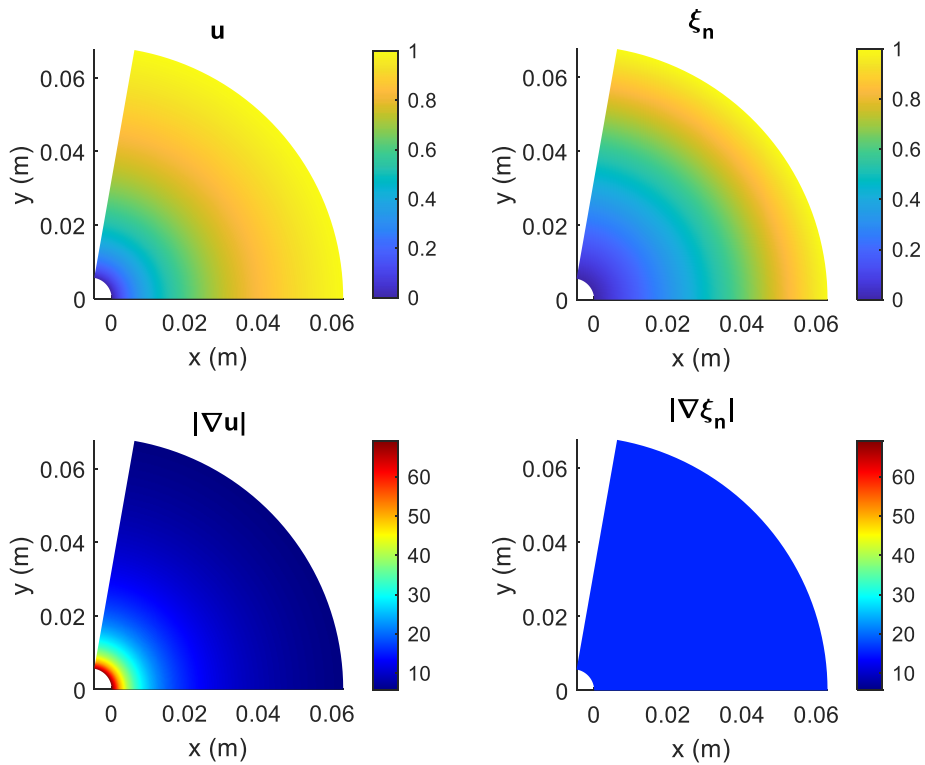
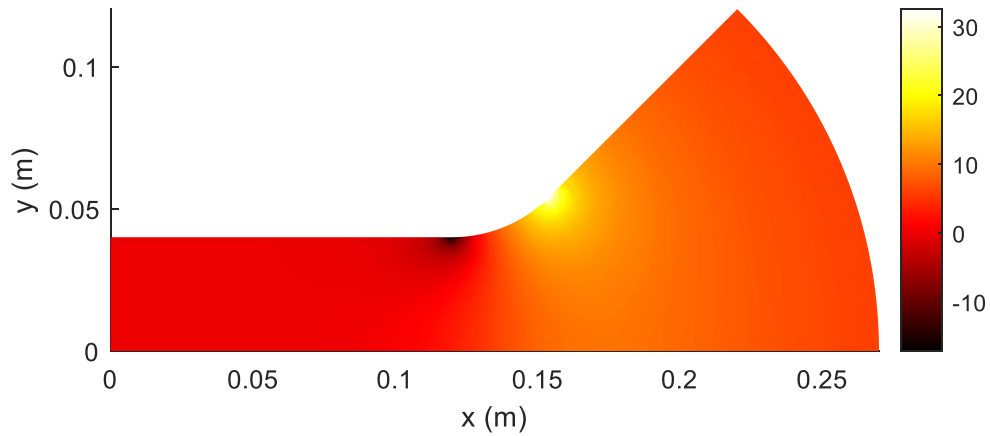


**Figure 26: Comparison of  $u$  and  $\xi_n$  on a conical wedge-shaped geometry**

In Figure 26,  $|\nabla u|$  changes due to the expansion in the domain but  $|\nabla \xi_n|$  stays constant. This makes  $\xi_n$  a useful coordinate system for moving through a domain from entrance to exit as it is equally spaced with reference to the longest streamline ( $\xi$  path) regardless of if the domain expands or not.  $\xi_n$  is therefore used in this project both as a coordinate system and as a reference point for plotting data down the streamlines.

## 5.6 Flare and felt area, $f$ and $a_f$ – the area metrics

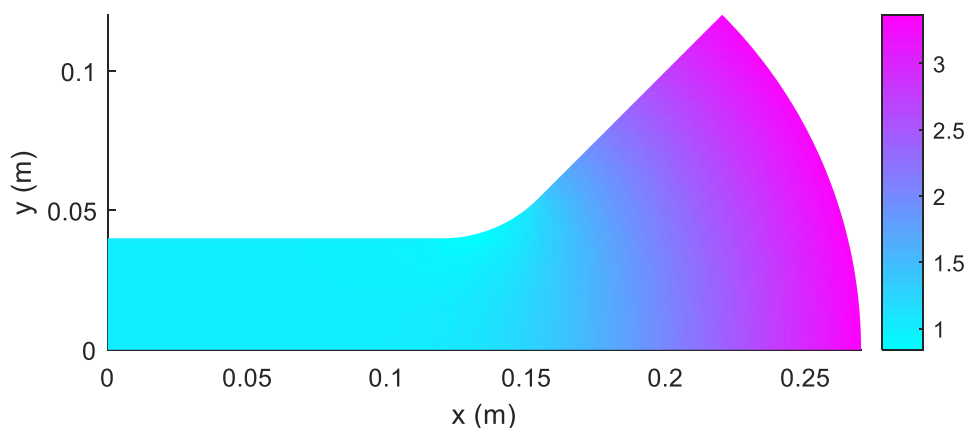
The flare  $f$  indicates the relative expansion in area. Figure 27 is a plot of  $f$  on the channel-wedge geometry. For the initial channel section  $f = 0$  and for the wedge section  $f > 0$  because of the increase in width.



**Figure 27: Flare  $f$  on the channel-wedge geometry**

Figure 27 also shows an interesting effect close to the top boundary at the transition between the channel and the wedge. Small, localised spots in  $f$  indicate that the expansion is decreasing before the corner and increasing after the corner. These spots are due to the change in curvature (and direction) of the channel, this effect is shown more clearly in Figure 41.

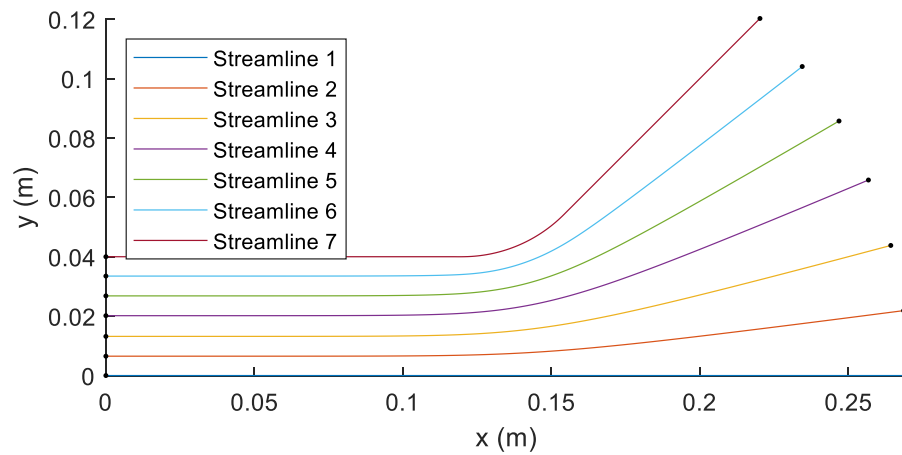
The relative change in cross sectional area or felt area ( $a_f$ ) was calculated from  $f$  using Eq (18). Because the integration is performed down the streamlines in the same direction as  $\nabla u$ , the entrance surface (with Dirichlet boundary condition of  $u = 0$ ) always has  $a_f = 1$ .  $a_f$  then indicates how the relative cross-sectional area changes through the geometry from entrance to exit.



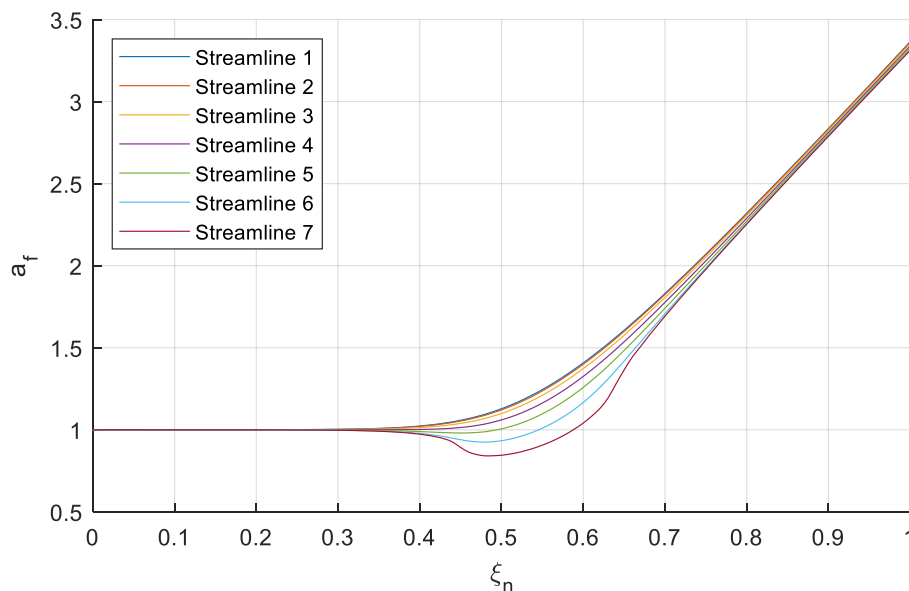
**Figure 28: Felt area  $a_f$  on channel wedge geometry**

Figure 28 shows the  $a_f$  on the Channel-wedge geometry. As expected,  $a_f$  indicates that there is no change in cross-sectional area for the channel section, and that it then increases in the wedge section.

Figure 29 shows 10 streamlines of  $\nabla u$  traced through the geometry, and Figure 30 shows the  $a_f$  on these streamlines.



**Figure 29: 10 streamlines of the vector field  $\nabla u$  traced through the channel wedge geometry**

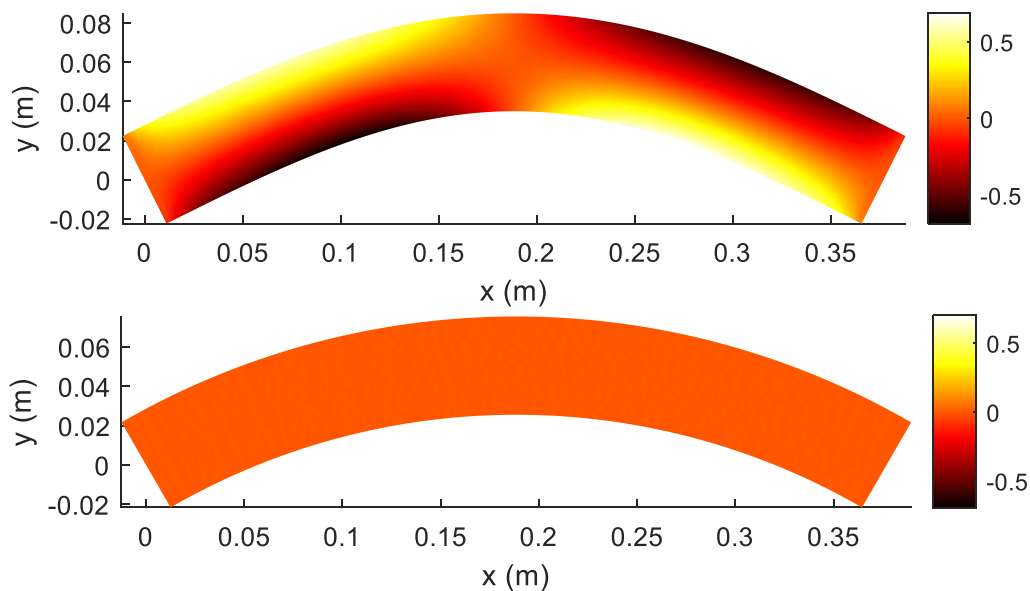


**Figure 30: 'Felt area'  $a_f$  down 6 streamlines calculated for the channel wedge geometry**

On all the streamlines  $a_f$  shows an increase in cross sectional area towards the end due to the wedge section. Interestingly there is some difference in  $a_f$  on the streamlines seen mostly around the transition point between the channel and the wedge.

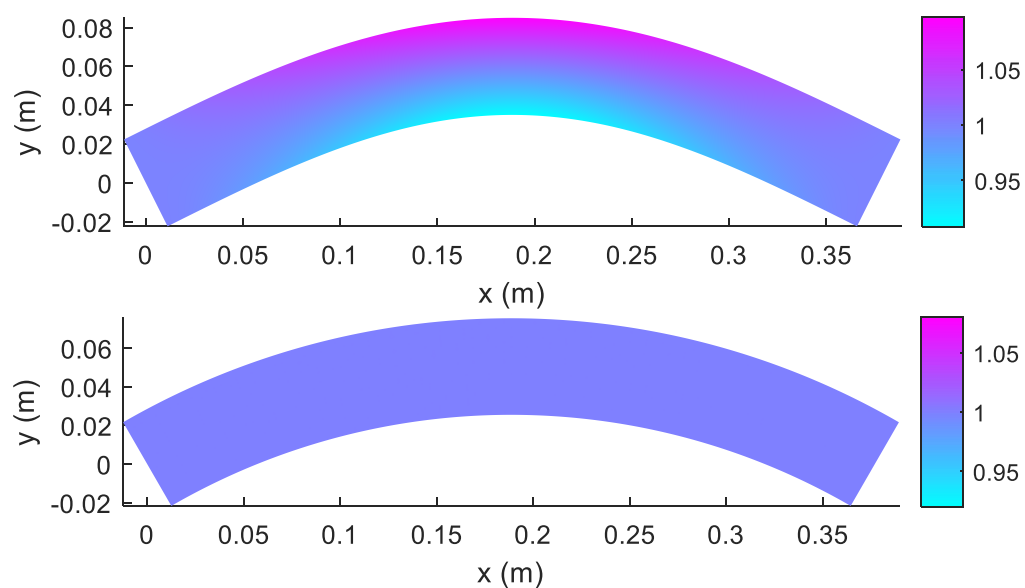
These differences in  $a_f$  are linked to the hot spots in  $f$  seen in Figure 27 and are due to the change in direction of the channel as it joins the wedge section. This effect is explored further by investigating the impact of the curvature on  $s$  and  $a_f$ , through analysing the half sine and constant radius arc geometries.

Figure 31 compares the flare  $f$ , and Figure 32 then compares the felt area metric  $a_f$ . The constant radius arc has no change in both  $f$  or  $a_f$ .



**Figure 31:  $f$  flare metric, top: half sine, bottom: constant radius arc**

In contrast, on the half sine,  $f$  moving from entrance to exit (left to right) indicates that close to the top boundary the domain expands and then decreases after the middle of the curve. The opposite effect is seen on the bottom boundary. This then causes  $a_f$  in Figure 32 to suggest that the area has slightly increased close to the top boundary (outside curved edge), where the curvature is at a maximum, and slightly decreased on the bottom boundary (inside curve edge). This is an interesting result as the domain has a constant width, so the physical cross-sectional area does not change. For a wave travelling through the duct, the change in curvature causes an apparent change in area which varies across the width of the channel.



**Figure 32:  $a_f$  (felt area metric), top: half sine, bottom: constant radius arc.**

The area metrics  $f$  and  $a_f$  were also computed on the S-bend geometry (Figure 33). The immediate transition between the two bends which creates a sharp change in curvature (see

Figure 12) causes intense concentrated spots in  $f$  close to each edge (note the different scales to Figure 31). This then causes  $a_f$  to indicate in the second half of the domain that the area has significantly increased close to the top boundary and decreased close to the bottom boundary.

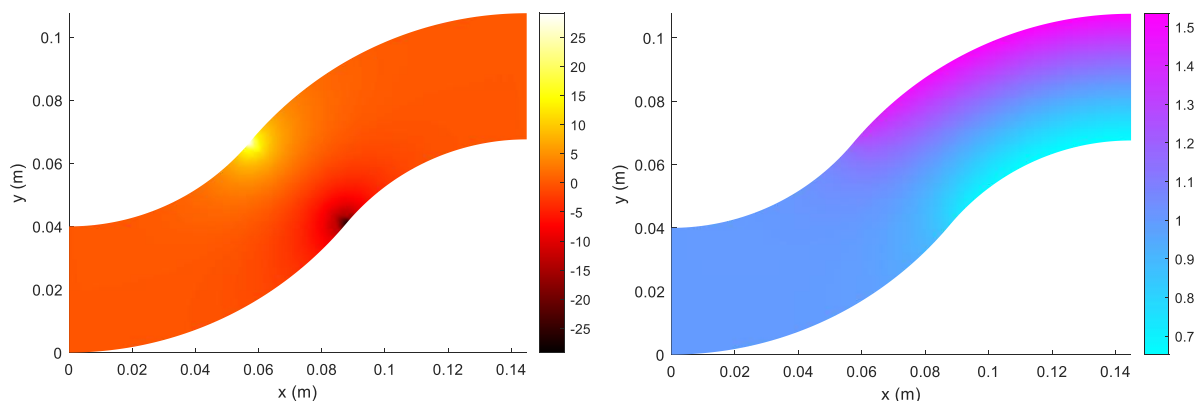


**Figure 33: s-bend geometry, left:  $f$  (flare), right:  $a_f$  (felt area)**

Figure 31 and Figure 33 illustrate how the metrics related to area,  $f$  and  $a_f$ , respond to changes in curvature in a duct of constant width. The S-bend simulation shows that sharp changes in the curvature of the central line through the geometry cause  $a_f$  to suggest a significant change in area. When practical, it may therefore be best to start with a prototype geometry which has continuous curvature to avoid this outcome. The effect on  $a_f$  from adding extra channels to either side of the S-bend is explored in section 7.5.2.

## 5.7 Conclusions

This chapter looked at the waveguide metrics on different test geometries to help more clearly understand what they mean. The stretch metric  $s$  indicates how the relative pathlength through a domain compares to a reference  $\xi$  path, which in its normalised forms  $s_n$  and  $s_a$  is the maximum or average streamline pathlength at each point through the geometry respectively.

The flare  $f$  and felt area  $a_f$  metrics are related to the change in cross sectional area experienced by a 1P wave propagating through the domain. The effect of the curvature of a duct of constant width has an interesting effect on both the metrics related to pathlength ( $s$ ,  $s_n$ ,  $s_a$ ) and the metrics related to area ( $f$  and  $a_f$ ).

For a domain to support single parameter wave propagation perfectly it should show unity in both  $s$  and  $a_f$ , which means the shape satisfies Putland's (1993) conditions for single parameter wave propagation.

## 6. Waveguide pathlength optimisation

Using the waveguide analysis methods covered in chapter 5, the spatial capability of a waveguide or acoustic lens to support 1P wave propagation can be quantified over a complex arbitrary shaped domain. The metrics not only describe where the geometry is problematic, but they give a good indication of how it could be modified to improve its support for 1P wave propagation. The felt area  $a_f$ , which is computed from flare  $f$ , can be used to adjust the cross-sectional area in parts of a domain. And the normalised stretch  $s_n$  shows if the relative pathlength through a domain is too short, so can be used to guide addition of the correct amount of pathlength to areas where it is required.

### 6.1 Adding path length with corrugations

The stretch metric shows the change in the relative pathlength through a domain. In a thin channel, one method of helping equalise the relative pathlength error shown by  $s_n$  is to distort the geometry in areas where the domain is too short ( $s_n < 1$ ). This concept of distorting a thin domain to equalise the relative pathlength is outlined in the GP Acoustics patent EP3806086A1 (Dodd & Oclew-Brown, 2021).

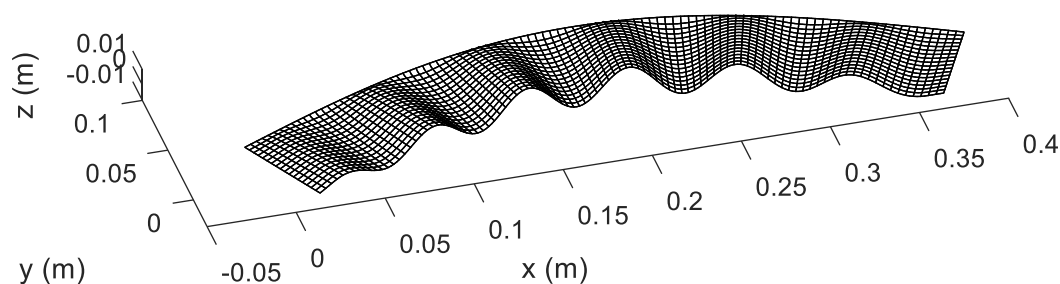


**Figure 34: Modulated half sine shell geometry**

Figure 34 is an example of how sinusoidal shape distortions can be used to add pathlength to regions of a shell mesh of the half sine geometry. It shows a curved duct of thin vertical cross-section, which naturally has a shorter path length on its inner edge. To equalise the relative pathlength, out-of-plane corrugations (ripples) have been added. These have the biggest amplitude on the inside edge of the bend where the relative pathlength is shortest.

This chapter focuses on how corrugations of different shapes can be used to add pathlength to a shell domain. First the relationship between added pathlength and corrugation amplitude was explored for a single 2D corrugation. Once this relationship was understood, it could be

used to distort regions of a thin geometry with the correct corrugation amplitude to add the right amount of extra pathlength where required.

### 6.1.1 Corrugation shapes

Potentially any shape could be used to distort a flat mesh and add pathlength. In this research triangular and sinusoidal wave shaped corrugations were investigated as they have convenient periodic characteristics.

Possibly the simplest way to add pathlength to a flat surface is to add triangular shape ‘crinkles’ like the folds in the bellows of an accordion. The equation of a triangle wave is

$$y = 2 \left| 2 \left( \frac{x}{L} - \left\lfloor \frac{x}{L} + \frac{1}{2} \right\rfloor \right) \right| - 1 \quad (37)$$

where  $L$  is the period of the corrugations and  $\lfloor \cdot \rfloor$  is the floor function. Figure 35 shows one period of a triangular shaped corrugation with  $L = 2\pi$  at different amplitudes.

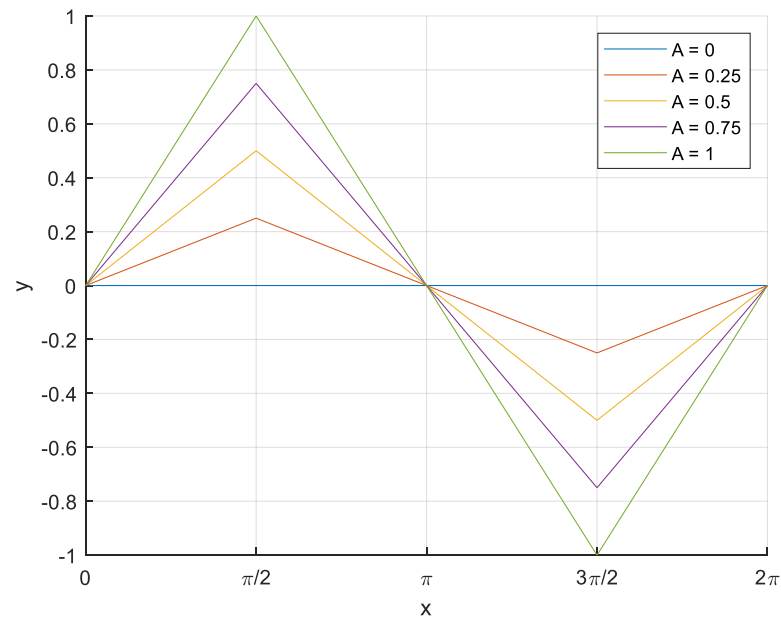


**Figure 35: Triangle waves of period  $2\pi$  and varying amplitudes**

Another possible distortion shape is the sinusoid shape, as was shown in Figure 34. Figure 36 shows some example sine waves of different amplitudes ranging from 0 to 1.

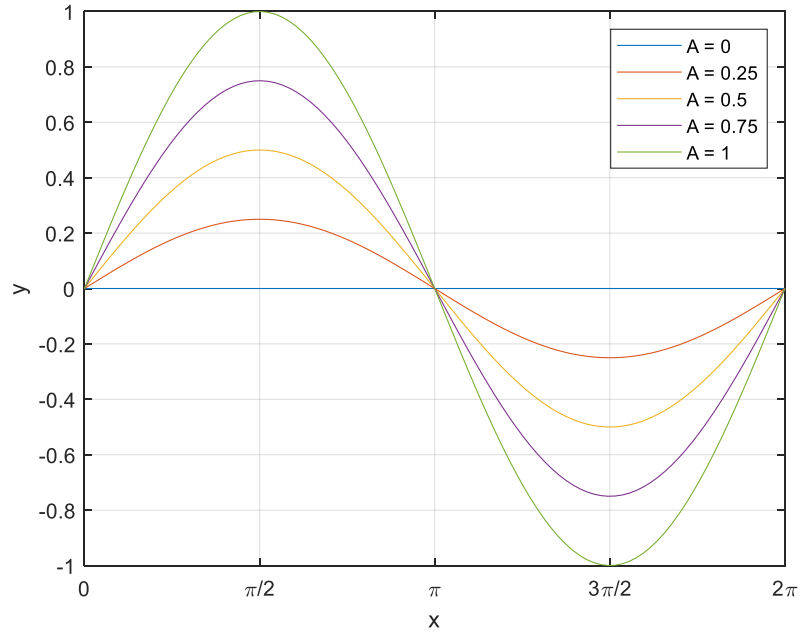


**Figure 36: Sine curves with different amplitudes**

Sine waves have continuous curvature and do not have the sharp corners at the peaks and troughs like a triangular wave possesses. The acoustic performance of thickened sinusoidal and triangular corrugation shapes is studied in section 7.2.3.

### 6.1.2 Arc length to amplitude relationship

The relationship between the amplitude and arc length of the corrugation shapes was investigated so that corrugations which add the correct amount of pathlength could be added to a surface. The added arc length is related to the gradient of the corrugation. For a triangle wave this has a constant magnitude, and the simple geometry leads to the following statement for the arc length  $d$  of a single period of a triangle wave:

$$d = L \times \sqrt{1 + \left(\frac{4A}{L}\right)^2}. \quad (38)$$

Here  $A$  is the amplitude and  $L$  is the period.

It is slightly more complex to calculate the arc length of a sine wave as the gradient changes continuously through the shape. Eq. (39) is the formula for the arc length of one period of a sine curve of amplitude  $A$  and period  $L$ .

$$d = \int_0^L \sqrt{1 + \left(A \frac{2\pi n}{L} \cos\left(\frac{2\pi n x_a}{L}\right)\right)^2} dx_a \quad (39)$$

Because of the complexity of the integral in Eq. (39), numerical methods were used to find the arc length  $d$ . Figure 37 illustrates the non-linear relationship between amplitude and arc length

for the sine and triangle waves of different periods  $L$ . Compared to the triangle wave the sine wave has slightly more arc length for the same amplitude.

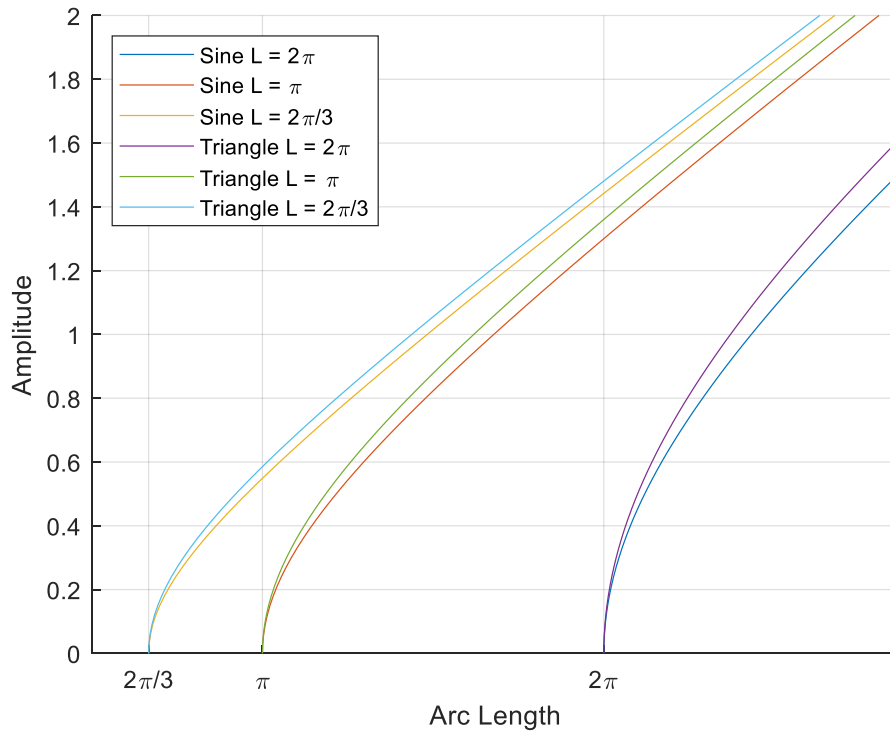


**Figure 37 Arc length to amplitude relationship of sine and triangle wave ( $L = 2\pi, \pi, \frac{2\pi}{3}$ )**

Figure 38 helps to visualise this relationship and shows sinusoidal and triangular waveshapes with periods of  $2\pi, \pi$  and  $\frac{2\pi}{3}$ . All of which have the same arc length of 7.64.

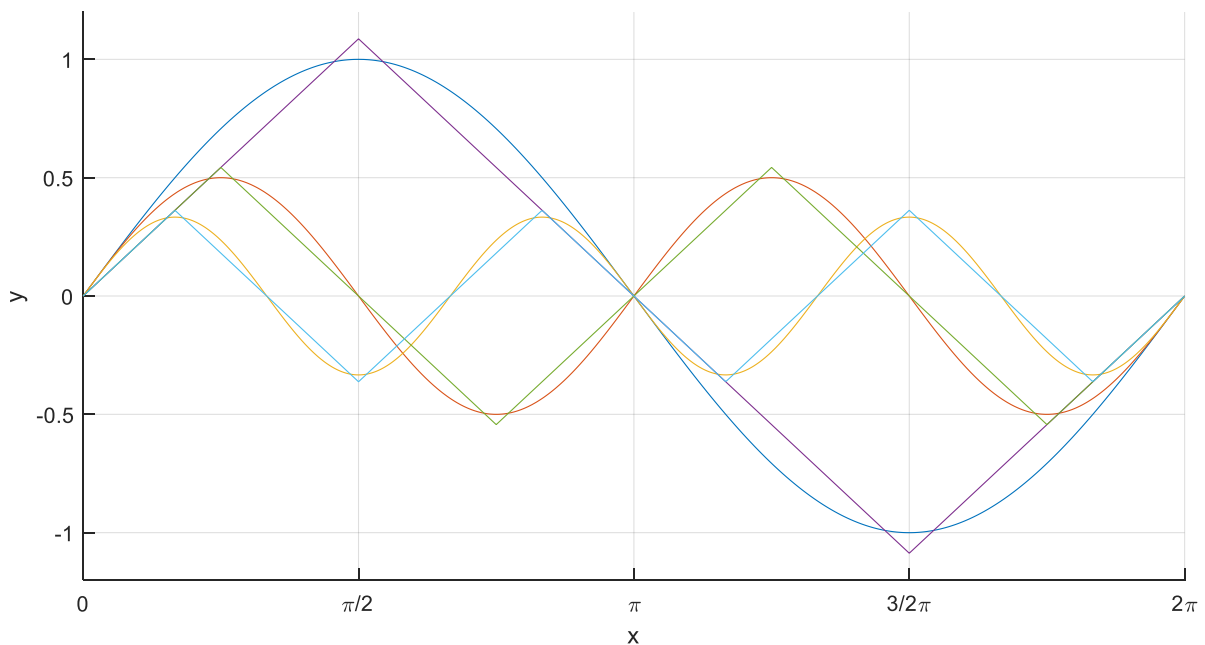


**Figure 38: example sinusoidal and triangular corrugations all with an arc length of 7.64**

It illustrates how the triangular shape corrugations require slightly more amplitude than the sinusoidal shape for the same arc length. It also highlights how an increased number of shorter corrugations (smaller period) require less amplitude to have the same arc length.

The normalised stretch metric  $s_n$  shows how much shorter regions of a domain are than the reference  $\xi$  path. When using corrugations to equalise the relative pathlength through a domain, the required arc length  $d$  of the corrugations can be calculated as:

$$d = \frac{L}{s_n}, \quad (40)$$

where  $L$  is the period or wavelenth of the corrugations. For a triangular corrugation, the required amplitude is therefore (from eq. (38)):

$$A = \frac{\sqrt{L^2(s_n^{-2} - 1)}}{4} \quad (41)$$

For sinusoidal corrugations,  $A(s_n)$  was found from using numerical methods.

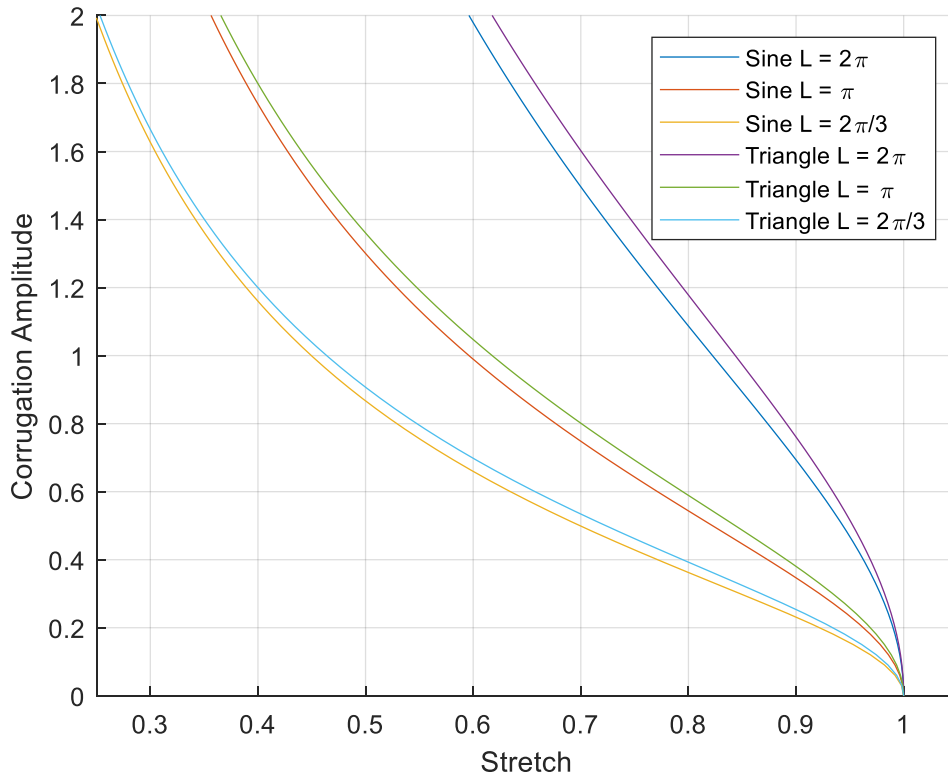


**Figure 39:**  $s_n$  to required corrugation amplitude  $A$  for sine and triangle wave ( $L = 2\pi, \pi, \frac{2\pi}{3}$ )

Figure 39 shows the relationship between the required corrugation amplitude  $A$  and  $s_n$  for sinusoidal and triangular shaped corrugations of different periods. This relationship could then be used to distort regions of a thin domain where  $s_n < 1$  with corrugations of the correct amplitude to help equalise the relative pathlength through the domain.

### 6.1.3 Error from adding pathlength with sinusoidal corrugations

Added pathlength is a function of the gradient of the corrugation function. For a triangular wave corrugation, the magnitude of the gradient is constant. This means that path length is added equally anywhere on the triangular shaped corrugation. In contrast the constantly changing gradient of a sine wave shape means that pathlength (relative to the x axis) is added non-linearly throughout the sinusoid shape.

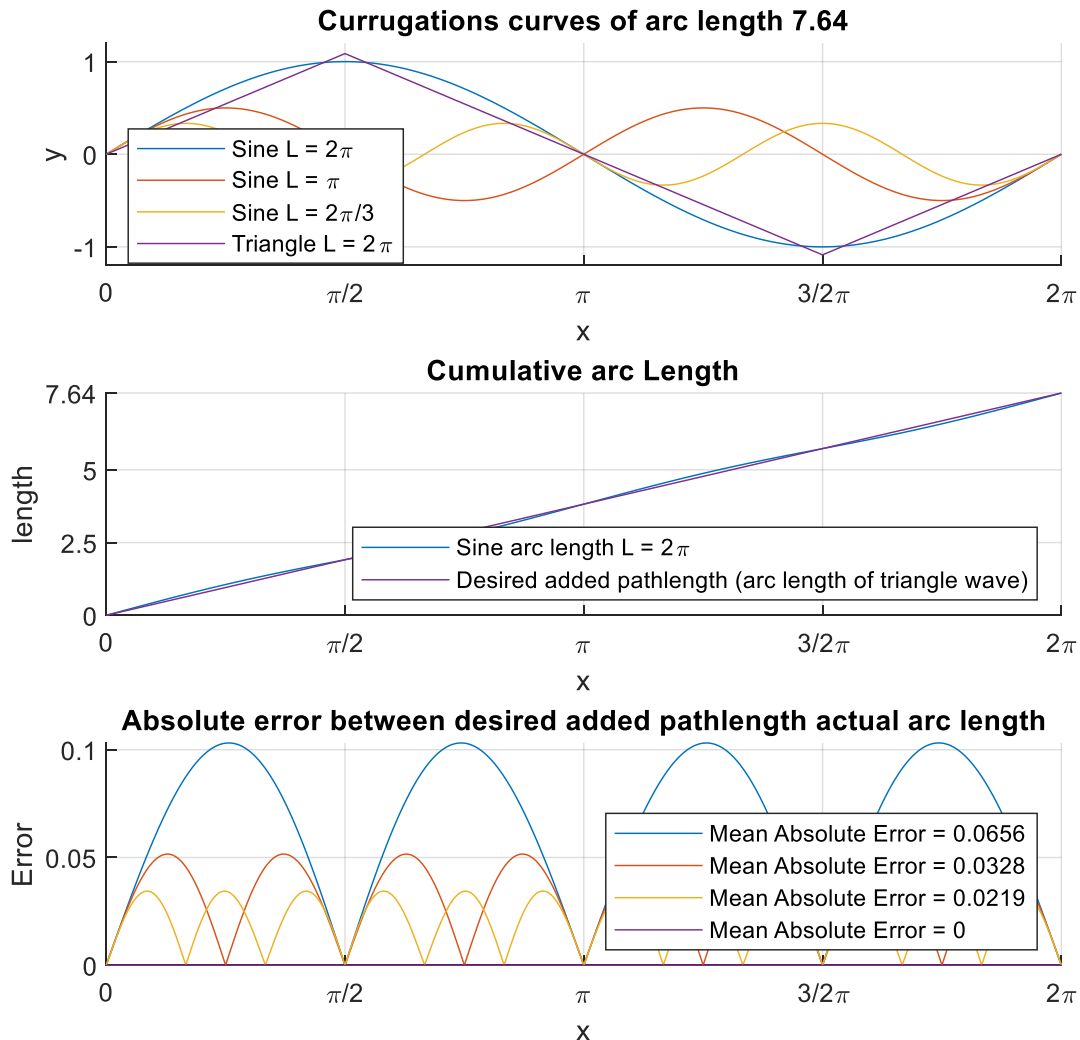


**Figure 40: Periodic error from adding pathlength with sinusoidal corrugations**

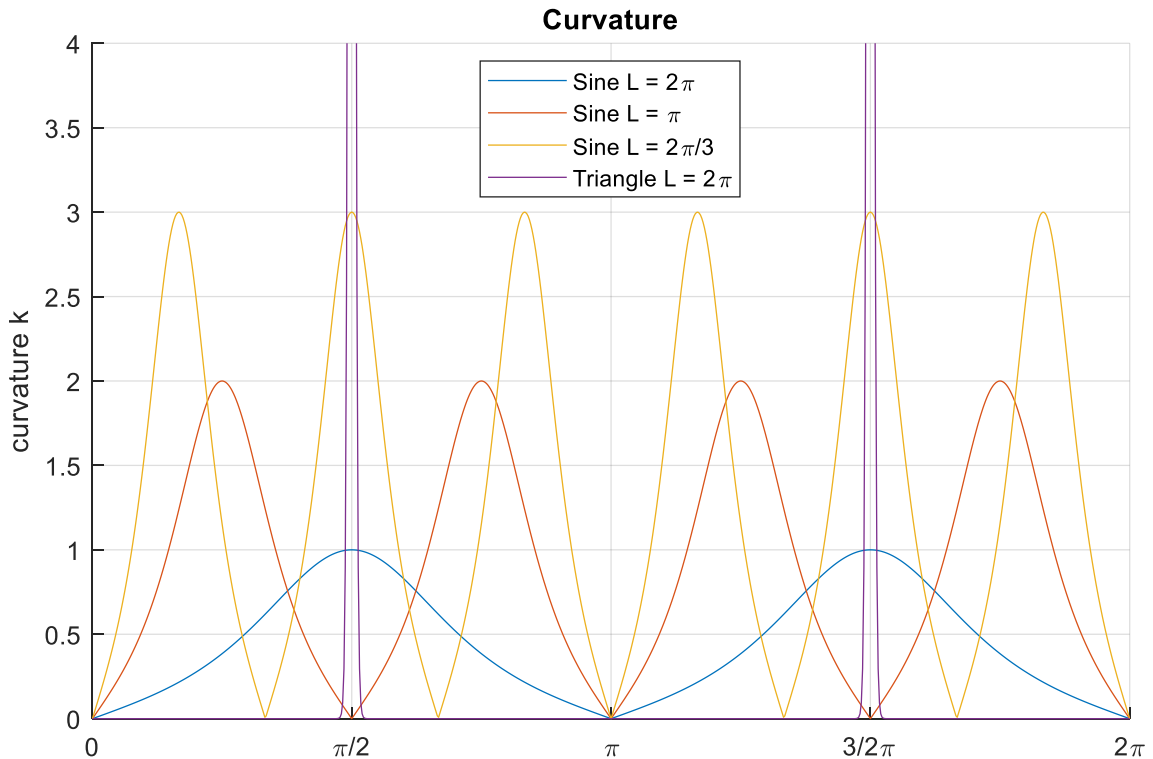
Figure 40 demonstrates this by examining different corrugations all with a total arc length of 7.64. The absolute error between the sinusoidal arc length and a desired linear pathlength is periodic and related to the period (length) of the waveshape. This error occurs because the sinusoidal corrugation does not add pathlength uniformly – none is added at the top and bottom of the curve, then more is added in the steep sections to compensate.

Figure 40 also shows that using sinusoidal corrugations with a smaller repeat period results in less error, which comes in shorter cycles. This means that to compensate for small spatial

details in  $s_n$  smaller period sinusoidal corrugations should be used so that the pathlength correction is more accurate and there is a better “corrugation resolution”.

#### 6.1.4 Corrugation curvature

A final characteristic of the corrugation shapes worth exploring is the curvature  $k$  (see eq. (34)). Figure 41 is the curvature of the modulation shapes in Figure 40 calculated using piecewise polynomial differentiation.



**Figure 41: curvature  $k$  of different corrugation shapes (see Figure 40 for original shapes)**

The triangle shaped corrugation has  $k = 0$  everywhere except for the turning points where  $k \rightarrow \infty$ . The sinusoidal corrugations with the longest period ( $2\pi$ ) have on average the lowest curvature and then the curvature increases for sinusoidal modulations with a shorter period.

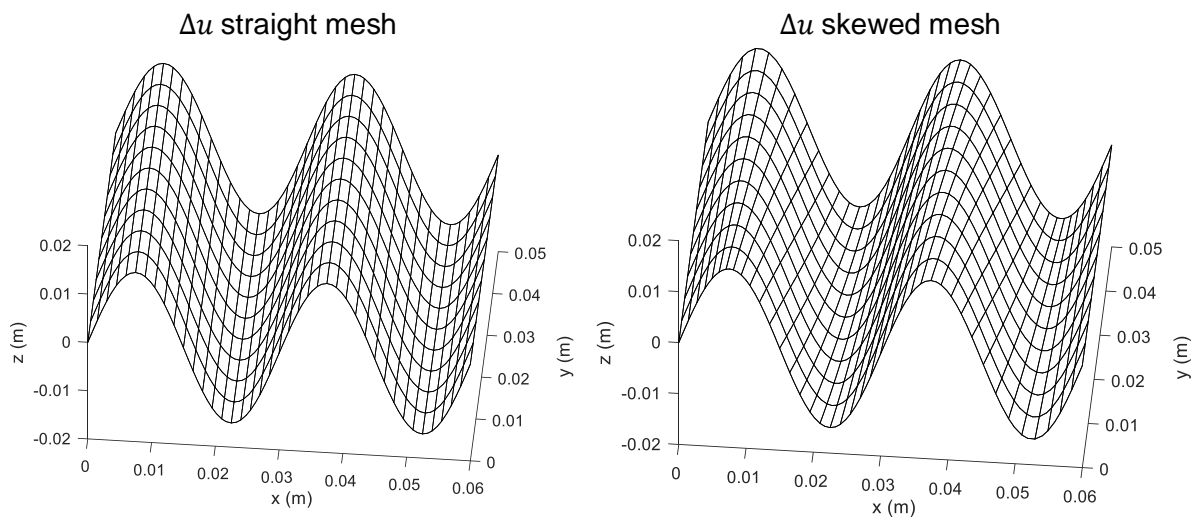
If high curvature in the sound propagation path is to be avoided, then using sinusoidal corrugations with a larger period is the best option. However, as was seen in Figure 40 larger period sinusoidal corrugations result in more periodic error in the added pathlength. This creates an interesting trade-off between minimising the curvature and periodic added pathlength error in the modulations.

#### 6.1.5 Problems with computing the gradient on corrugated meshes

It was found that large corrugations or distortions in a shell mesh could sometimes introduce error in the computation of the gradient of a function on the mesh. This can be an issue when

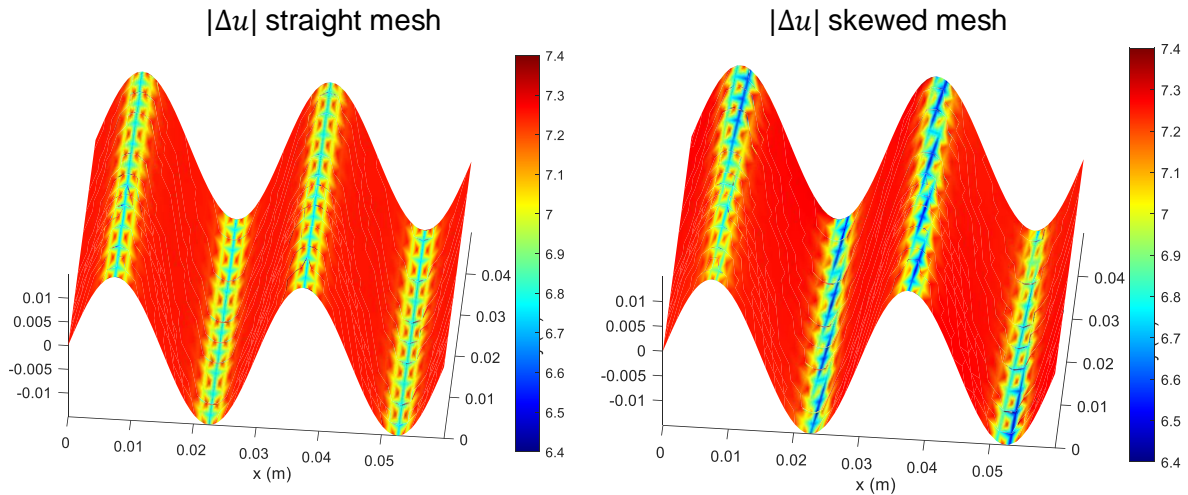
trying to re-analyse a mesh of a domain that has been corrugated according to the waveguide metrics, as computation of  $s_n$  and  $a_f$  both rely on mesh gradient operations (see section 4.1.3).

This section investigates the effect of shell mesh distortions on gradient calculations by analysing a coarse rectangular mesh that is deformed with large sinusoidal corrugations in the normal ( $z$ ) direction. Figure 42 shows two examples of this mesh. On the left-hand side the mesh is neatly aligned with the corrugations. In contrast, on the right-hand side it has been slightly skewed so that the mesh is no longer parallel to the crests and troughs of the corrugations.



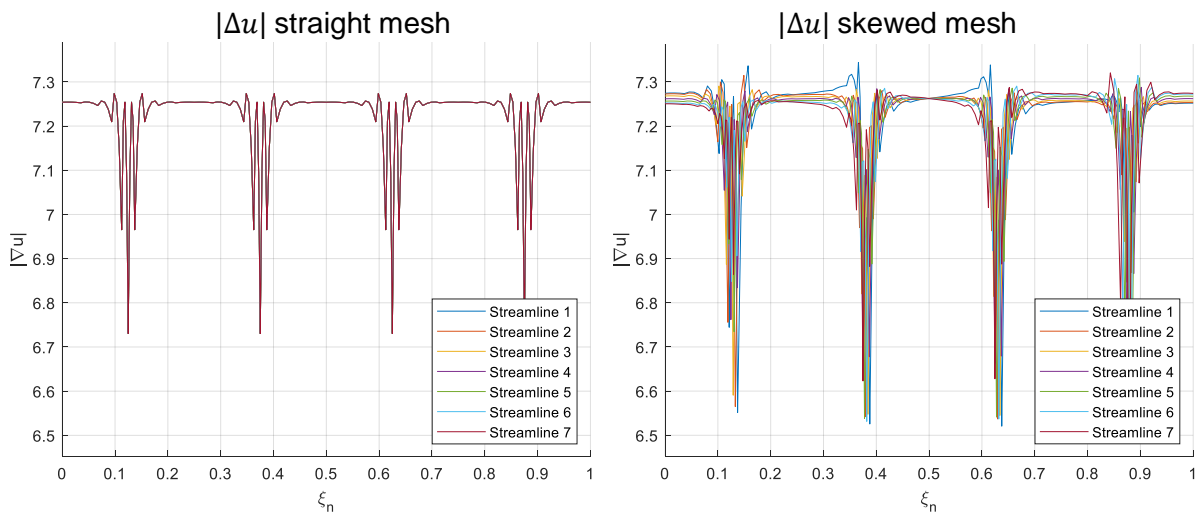
**Figure 42: Sinusoidal modulated rectangular mesh, left: straight mesh aligned with corrugations, right: skewed mesh which is not aligned with corrugations**

Figure 43 shows the  $|\nabla u|$  calculated over the two meshes from Figure 42. Like when computing the metrics in section 5, Dirichlet boundary conditions with values of 0 and 1 were imposed on each end of the domain (left to right) to mark the entrance and exit.



**Figure 43:  $|\Delta u|$  over modulated rectangular domain, comparing straight and skewed meshes**

Figure 44 shows the same result but interpolated to 7 traced streamlines of  $\nabla u$ . The example with a skewed mesh in relation to the corrugations has a bigger variation in  $|\nabla u|$  which also varies between each streamline.



**Figure 44:  $|\nabla u|$  on streamlines traced through modulated rectangle, comparing aligned and skewed meshes.**

If the modulated shell domain was to be pulled flat it would make a perfect rectangle, so  $|\nabla u|$  should be constant throughout. The fluctuations seen in the calculated values of  $|\nabla u|$  at the peaks and troughs of the corrugations is error due to the coarse mesh poorly representing the continuous curve of the corrugations. Because such a coarse mesh has been used for illustrative purposes, there is still a considerable error in  $|\nabla u|$  in the example where the mesh is aligned to the corrugations (left-hand side of Figure 44). However, the error is notably less than with the skewed mesh (right-hand side of Figure 44) which has especially warped elements because it is not aligned with the corrugations.

When modulating a shell mesh, the error introduced to the gradient calculations is therefore increased when the mesh is skewed in relation to the corrugations, because it causes especially warped elements where the curvature of the mesh is greatest. Therefore, it is best to have a mesh that is neatly aligned with the corrugations where possible.

Another problem from using a mesh which is skewed in relationship to the corrugations was that they occasionally caused streamlines to prematurely fall off the edge of the domain during the streamline tracing process. This is because the warped elements cause  $\nabla u$  to change direction as well as magnitude. Though this could possibly be avoided by using a finer mesh and lower amplitude corrugations, it demonstrates again why it is best to start with a mesh which is aligned with the corrugations.

### 6.1.6 $\xi_n$ spaced meshes

To avoid the problems found with gradient calculations discussed in section 6.1.5, each model was first re-meshed with equal spacing in  $\xi_n$  before calculating the metrics.

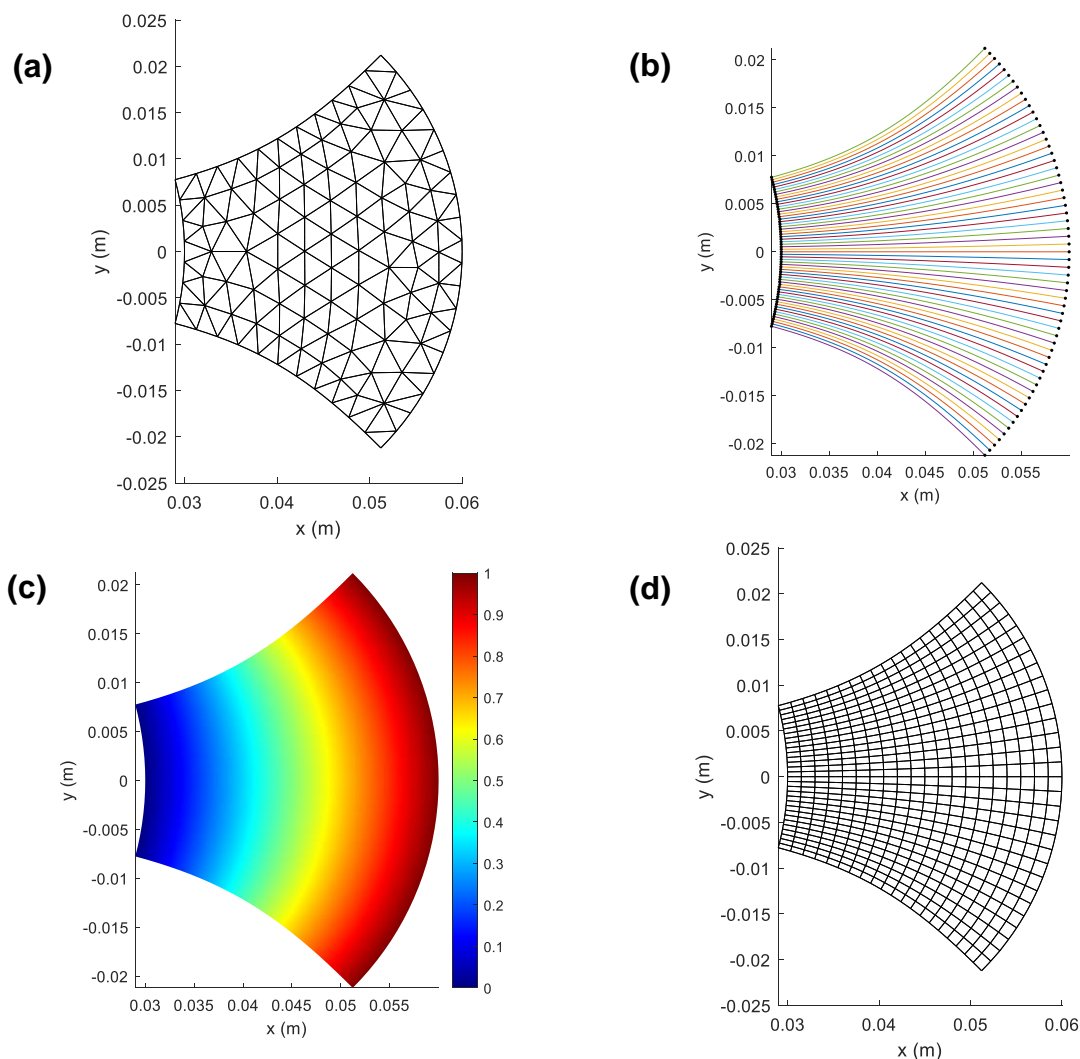


**Figure 45: (a) original arbitrary free tetrahedral mesh, (b) traced streamlines of  $\nabla u$ , (c)  $\xi_n$ , (d) new  $\xi_n$  spaced mesh**

This process followed the same steps for calculating  $\xi_n$  shown in section 5.5. After this a new mesh was built by placing nodes at a uniform spacing in  $\xi_n$  along the streamlines. Figure 45 illustrates this procedure for an arbitrary flared geometry which starts with a free tetrahedral mesh

$\xi_n$  was used for the spacing to build new meshes instead of  $u$  because  $|\nabla u|$  changes throughout the domain in a design which has expansion, while  $\xi_n$  does not (see Figure 26). Therefore, building a mesh based on  $|\nabla u|$  would produce a mesh with a bigger nodal spacing in the direction of  $\nabla u$  as the domain expands, which is undesirable.

Figure 45 (d) shows the resulting mesh which is equally spaced in  $\xi_n$ . Because corrugations were then added using  $\xi_n$  as a coordinate system to move through the geometry, it means the mesh is perfectly aligned with the corrugations. This produces a better representation of the modulated geometry with fewer mesh elements.

### 6.1.7 Further mesh problems caused by triangular shaped corrugations

Aligning the elements in a shell mesh with the corrugations helps the gradient calculations behave better. However, there can still be problems when using triangular shaped corrugations due to the sharp corners found at the peaks and troughs of the triangle wave shape. An example of this is shown in Figure 46.

The severe error in the calculation of  $|\nabla u|$  happens because the nodes at the peaks and troughs of the corrugations are shared between two elements with extremely contradicting normal directions. This causes error when averaging  $\nabla u$  calculated from each element on the shared nodes as the direction of the vector  $\nabla u$  in the global coordinates is different on each side of the crest or trough.

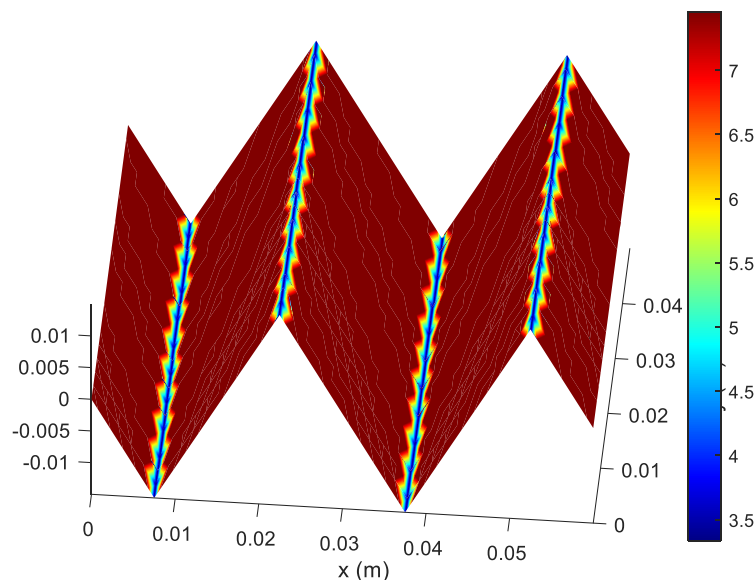


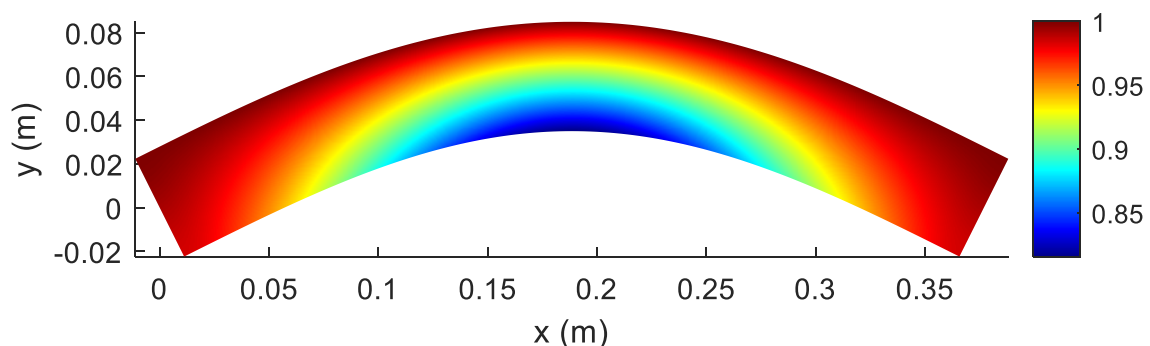
Figure 46:  $\nabla u$  with sharp triangular corrugations

Unfortunately, this means that when using triangular shaped corrugations to add pathlength, waveguide metric calculations on the modulated domain are unreliable at the peaks and troughs. This problem did not arise with sinusoidal corrugations because the quadratic mesh shape functions made an accurate enough approximation of the sinusoid shape that there was little difference in the direction of the gradient vectors from different elements to be averaged over each shared node. Of course, it is possible to conceive overlapping shape functions that overcome these limitations (e.g. NURBS), but shape functions of this type were not implemented in this project.

## 6.2 Optimisation test case – Half sine

This section investigates how to compensate for differences in the relative pathlength through a domain characterised by non-unity values in the normalised stretch metric  $s_n$ . To equalise the relative pathlength the mesh was distorted in specific areas with corrugations in the normal direction to the mesh. The amplitude of the corrugations  $A$  at each node was calculated from  $s_n$  using the number of corrugations  $n_{mod}$  and the  $s_n$  to amplitude relationship seen in Figure 39.

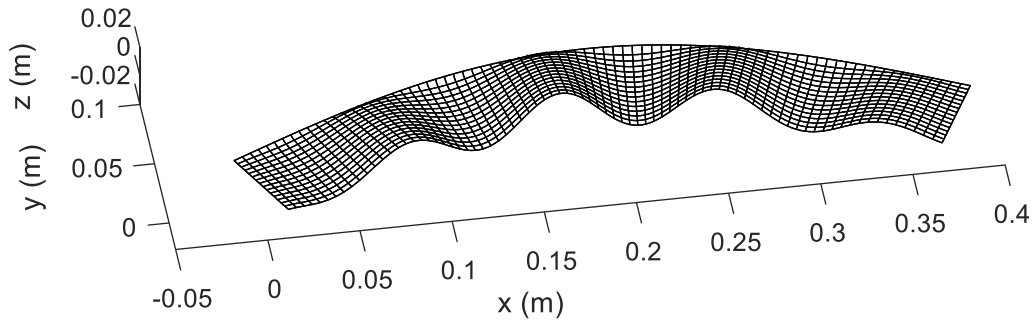
$\xi_n$  was used as the coordinate system with which to build the periodic corrugations and move through the domain from entrance to exit. This ensured that the corrugations were always perpendicular to the edges of the domain and parallel with surfaces of constant  $u$ . Using  $\xi_n$  as a coordinate system to build the periodic corrugations from means that the physical period or wavelength of each corrugation changes depending on  $s_n$ . This effect was accounted for when calculating the  $s_n$  to amplitude relationship.



**Figure 47:**  $s_n$  on half sine 2D flat domain

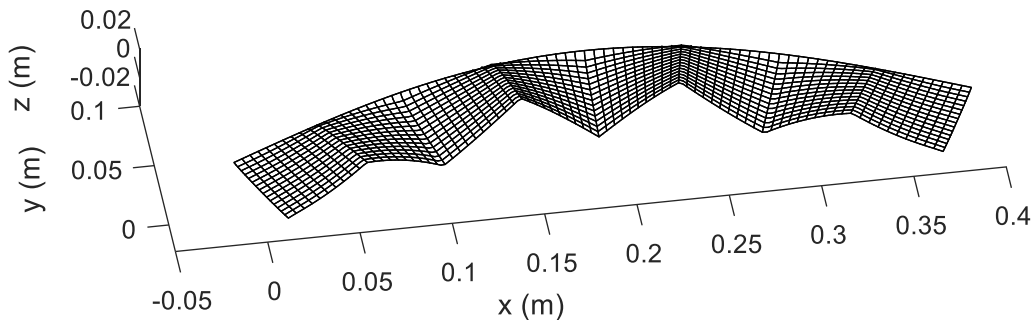
A good initial pathlength correction test case was the half sine, which is half a period of a sine wave widened to create a 2D geometry. Figure 47 shows how on the 2D geometry  $s_n$  indicates that the relative pathlength is shorter on the inside of the curve with the biggest difference in the centre of the domain where the curvature is highest. Figure 48 shows a shell mesh

created by modulating the 2D geometry in Figure 47. For this example, 4 sinusoidal corrugations were used.



**Figure 48: Half sine with 4 sinusoidal corrugations to equalise the relative pathlength**

$s_n$  causes the corrugations to have the largest amplitude on the inside edge of the bend around the centre of the model where the relative pathlength is shortest.



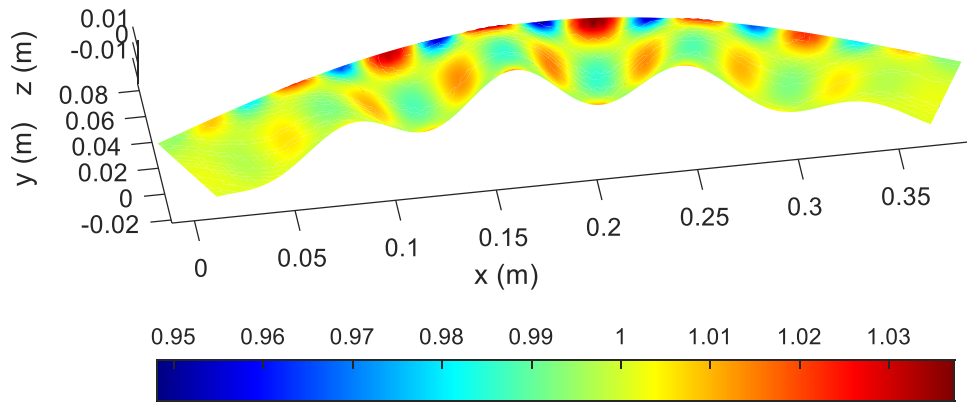
**Figure 49: Half sine with triangular corrugations to equalise the relative pathlength**

Figure 49 shows the same geometry but with triangular shaped corrugations. Because the corrugation amplitude  $A$  is a function of  $s_n$ , which changes along the inside edge of the half sine, it causes the triangular shaped corrugations to have slightly curved walls.

### 6.2.1 Re-analysing a modulated domain

To see if the pathlength compensation helped improve the geometry, the new corrugated shell domains were re-analysed with the stretch metric. If the corrugations are working as intended, and the geometry is more capable of supporting 1P wave propagation, the stretch metric should show less variation in the relative pathlength through the domain.

When reanalysing the modulated domain, instead of using stretch normalised to the longest  $\xi$  path,  $s_n$ , the average stretch  $s_a$  was used.  $s_a$  is the ratio of the relative pathlength to the mean  $\xi$  path length through the domain, which means it helps to highlight regions where too much or too little pathlength has been added by the corrugations.



**Figure 50: Average stretch  $s_a$  on half sine with four sinusoidal shaped corrugations**

When viewing the waveguide metrics on a shell mesh it is worth noting that they only show error parallel to the surface of the mesh and not perpendicular to it. This is because the mesh uses two dimensional elements in a three-dimensional space, which is equivalent to having an infinitely thin domain.

Figure 50 shows  $s_a$  on the half sine with sinusoidal corrugations. The range of  $s_a$  is significantly less than  $s_n$  on the 2D geometry (Figure 47) which suggests the modulated domain is an improvement. There is also a complex periodic pattern seen in the metric which is related to the gradient of the corrugations and is due to how the sinusoidal shape adds pathlength in a non-linear periodic manner. This effect is related to the findings in Figure 40 which highlight the periodic error in the added pathlength when using sinusoidal corrugations.

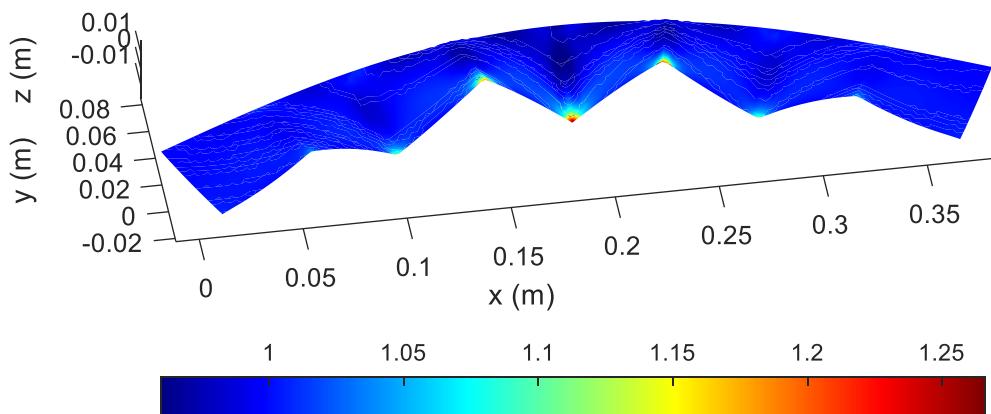


**Figure 51: Average stretch  $s_a$  on the half sine with four triangular shaped corrugations**

Figure 51 shows  $s_a$  on the half sine with four triangular corrugations. It is worth noting Figure 51 has a different scale to Figure 50. The sharp corners at the crests and troughs of the corrugations cause intense localised hotspots, which could cause problems for the performance of the waveguide. However,  $s_a$  appears closer to unity in other regions of the domain when compared with the 2D model (Figure 47).

In some situations, it can be more revealing to look at the metrics on the streamlines. Figure 52 shows 5 streamlines traced through the half sine geometry and should be used as a guide for understanding the streamline numbering in Figure 53.

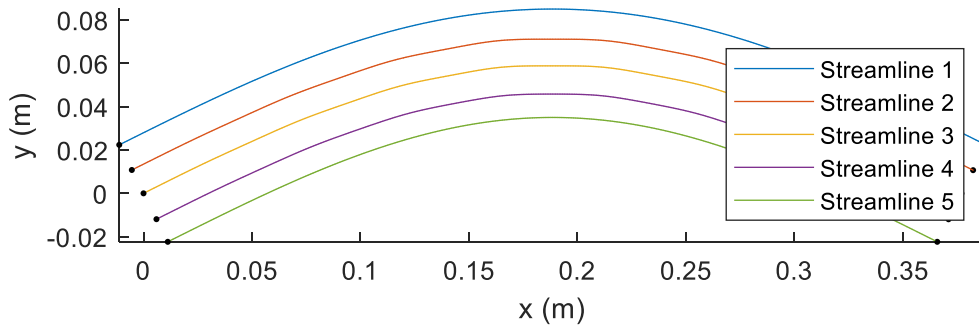


**Figure 52: Five streamlines traced through the half sine geometry**

Figure 53 compares the stretch values on five streamlines for the half sine with no pathlength optimisation, with sinusoidal shaped corrugations, and with triangular shaped corrugations. Overall, both modulated domains have less relative pathlength error than the original domain, which suggests the corrugations are successfully helping to equalise the relative pathlength.

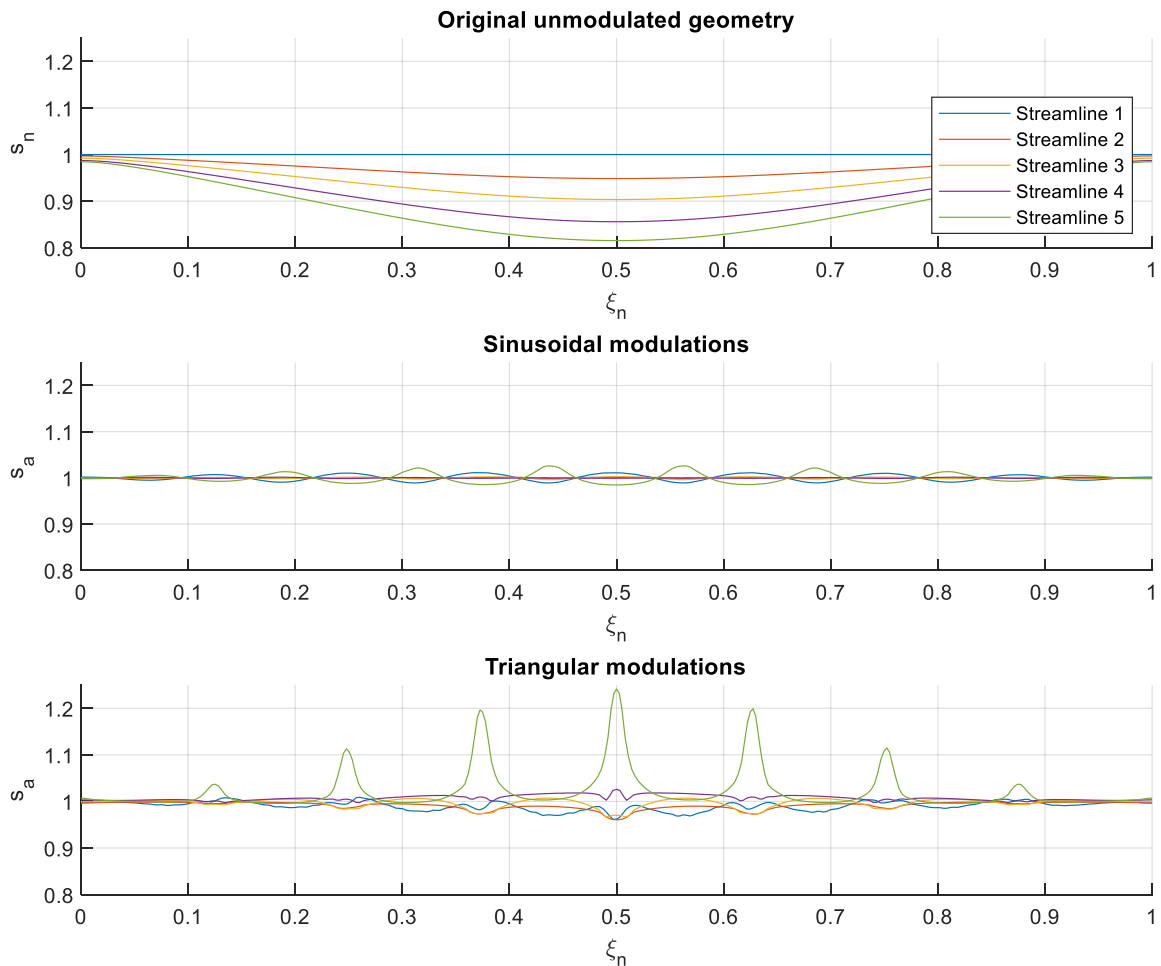


**Figure 53: Comparison of  $s_a$  and  $s_n$  on 5 streamlines through half sine geometry with and without triangular and sinusoidal corrugations**

The triangular shaped corrugations have most pathlength error on streamline 5 which is on the outside edge of the domain because this is where the sharpest corners from the corrugations are.

In contrast the sinewave modulated domain has most error on streamline 1 which is on the outside edge of the bend. It was found that this happens because, when using corrugations to go from adding no pathlength (zero amplitude) to adding a small amount of pathlength, a big change in the amplitude is needed. This causes the mesh to curl round abruptly at the outside edge towards being flat, where  $s_n$  is zero and no pathlength needs to be added. The warped elements which curl round then indicate significant error in  $s_n$ .

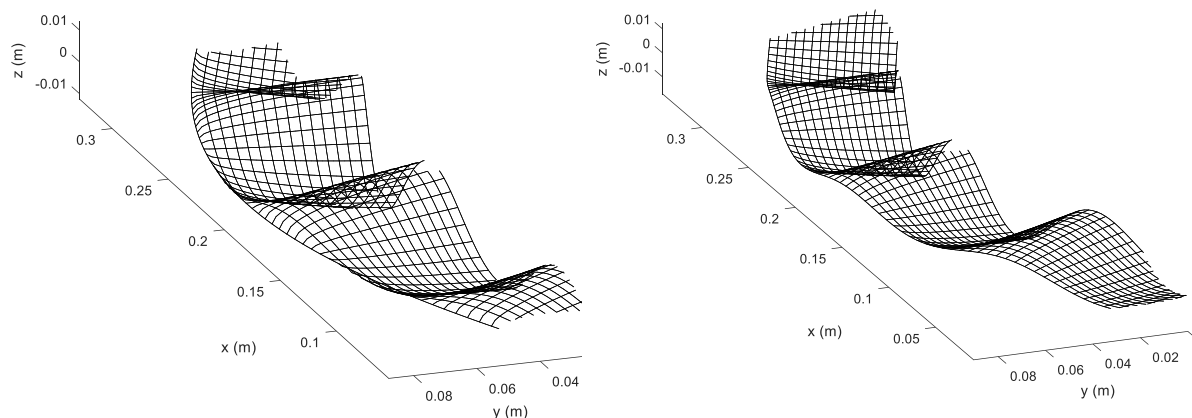


**Figure 54: Half sine corrugated mesh closeup, left:  $s_o = 0$ , right:  $s_o = 0.01$**

This curl in the mesh towards the outside edge can be avoided by subtracting a constant “stretch offset”  $s_o$  from  $s_n$  which is used to build the corrugations. An example of this can be seen in Figure 54. In other words, adding a small amount of corrugation amplitude to all the domain avoids the warped elements created by the sharp transition to zero amplitude on the outside boundary.

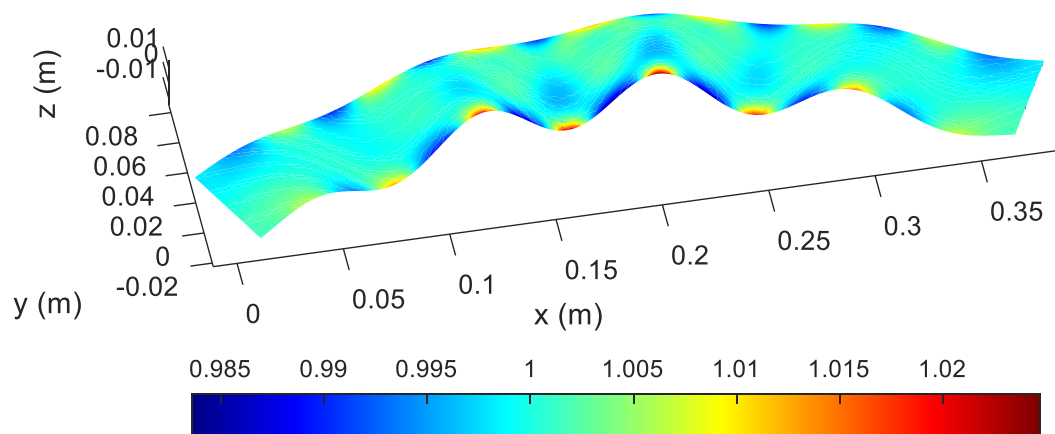


**Figure 55:  $s_a$  on in plane bend with 4 sinusoidal corrugations and  $s_o = 0.01$**

Figure 55 shows  $s_\alpha$  on the half sine with a stretch offset  $s_o = 0.01$ . Avoiding such a sharp curl in the mesh towards the outside boundary causes the pathlength error shown by  $s_\alpha$  to be even lower than in Figure 50. Because having  $s_o = 0.01$  was found to significantly reduce the severity of the warped elements close to the outside edge, it was used for all further pathlength optimised examples of the half sine in this project.

### 6.2.2 Effect of pathlength optimisation on felt area - $a_f$

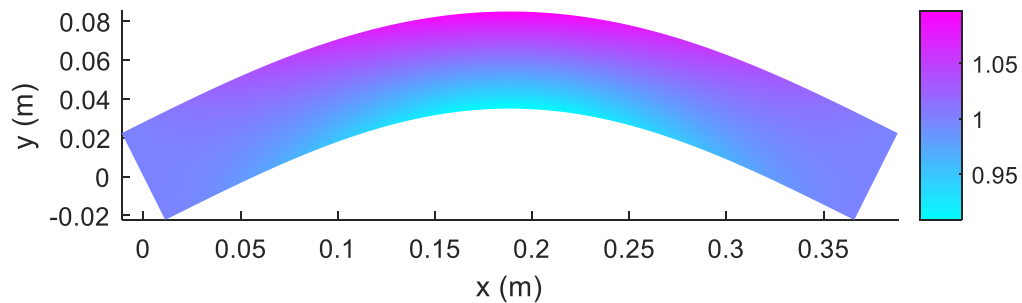


**Figure 56:**  $a_f$  on 2D half sine

Figure 56 shows the  $a_f$  on the 2D half sine before any optimisation. Because of the curvature of the channel, the metric suggests the area has decreased close to the boundary on the inside edge of the bend and increased close to the boundary on the outside edge.

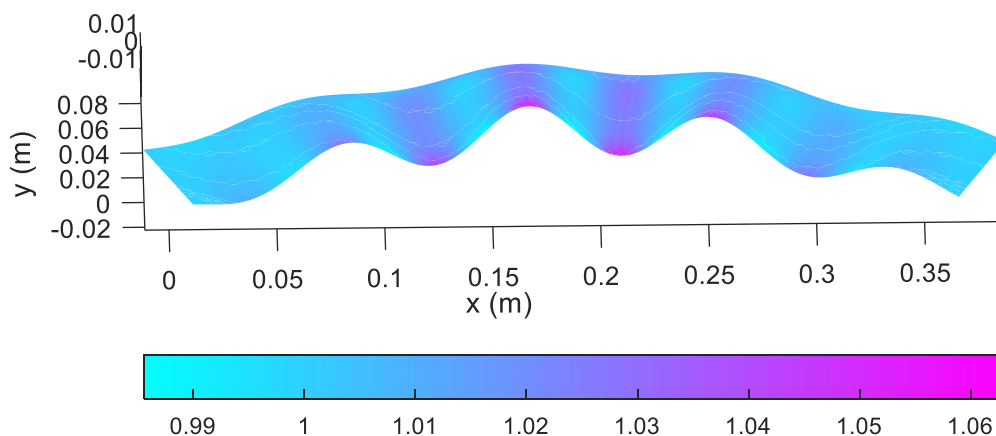


**Figure 57:**  $a_f$  on the pathlength optimised half sine geometry with four sinusoidal corrugations,  $s_o = 0.01$

$a_f$  was then calculated over the pathlength optimised in plane bend and is plotted in Figure 57. On most of the geometry  $a_f$  is between 0.98 and 1.04, except for a few hotspots at the turning points of the largest corrugations.  $a_f$  is therefore closer to unity than on the original flat two-dimensional geometry. This is an interesting result, as it shows that correcting the pathlength error shown by  $s_n$  also reduces the error in the felt area  $a_f$ .

### 6.2.3 Average squared metric error – Half sine

The mean squared error in the metrics was calculated by integrating over the surface of the shell mesh

$$\overline{error} = \frac{1}{S} \iint_S (m - 1)^2 dS \quad (42)$$

where  $S$  is the surface of the mesh, and  $m$  is the waveguide metric which is to be averaged.

**Table 2: Mean error in the metrics on the half sine geometry shell mesh with and without different pathlength optimisation**

Half sine geometry	$\overline{error}$ in $s_a$	$\overline{error}$ in $a_f$
No-pathlength optimisation	4.74e-03	1.14e-03
Triangular corrugations	2.89e-04	8.43e-04
Sinusoidal corrugations	8.18e-06	1.26e-04

Table 2 shows the average-square error for the two metrics and the three geometries. It can be seen that the models with pathlength optimisation corrugations show a reduction in the mean waveguide metric errors,  $s$  and  $a_f$ , for both sinusoidal and triangular shaped corrugations. The sinusoidal shaped corrugations gave the smallest mean error in both metrics, which suggests they are the best option for correcting the relative pathlength through a domain.

Because triangular corrugations resulted in extreme hotspots in the metrics, they make it hard to draw conclusions as to whether the undulated geometry is an improvement or not. Triangular corrugations are also shown to be worse acoustically in section 7.2.3. For these reasons, only sinusoidal shaped undulations are used in the other shell mesh test cases.

### 6.3 Optimisation test case – Channel Wedge

On the 2D channel wedge geometry in Figure 58,  $s_n$  shows that the highest pathlength error occurs around the transition point between the channel and the duct, close to the top boundary where the geometry turns the tightest corner. This causes the pathlength optimised shell mesh (Figure 59) to have corrugations mainly in this region too, with little to no corrugations in the rest of the geometry.

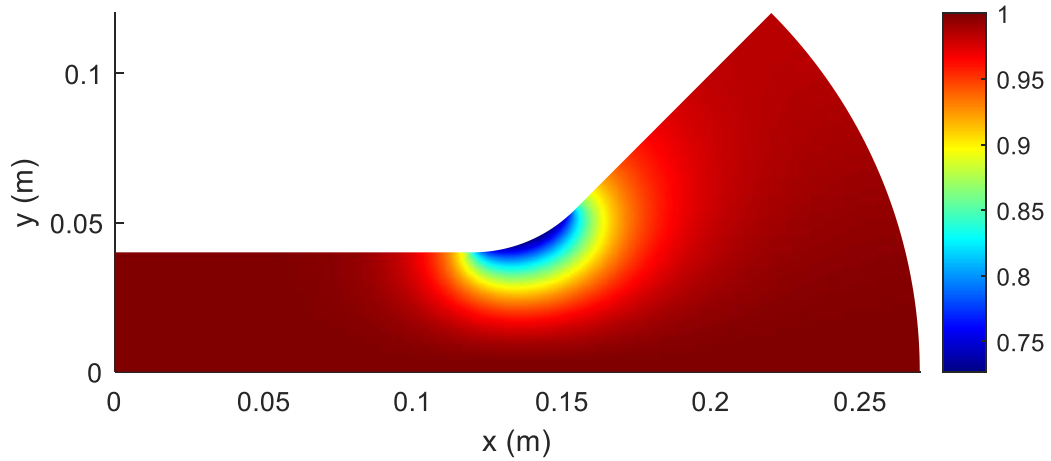


Figure 58:  $s_n$  on the 2D channel wedge geometry

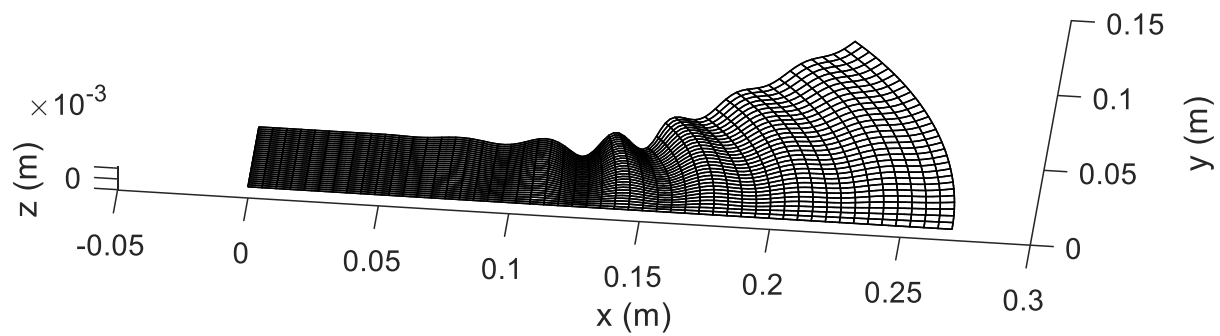


Figure 59: Channel-wedge geometry shell mesh with optimised sinusoidal corrugations

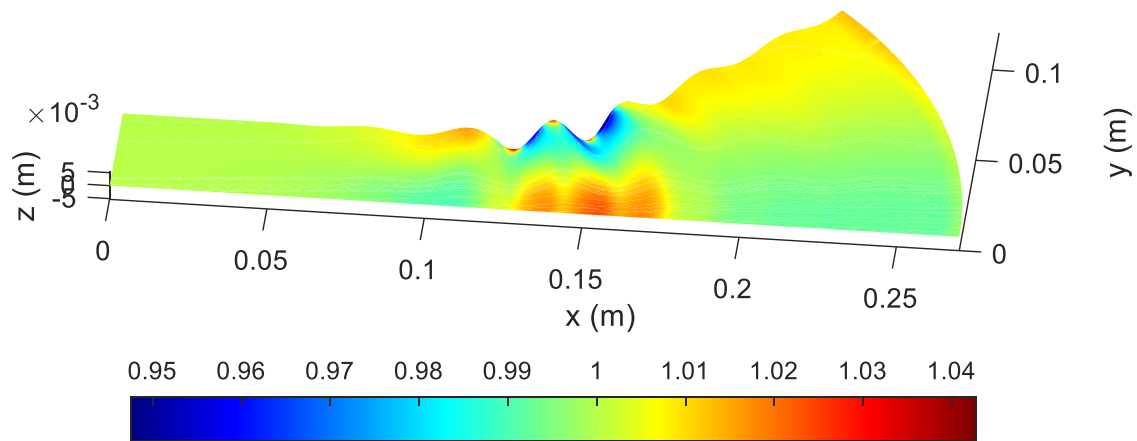
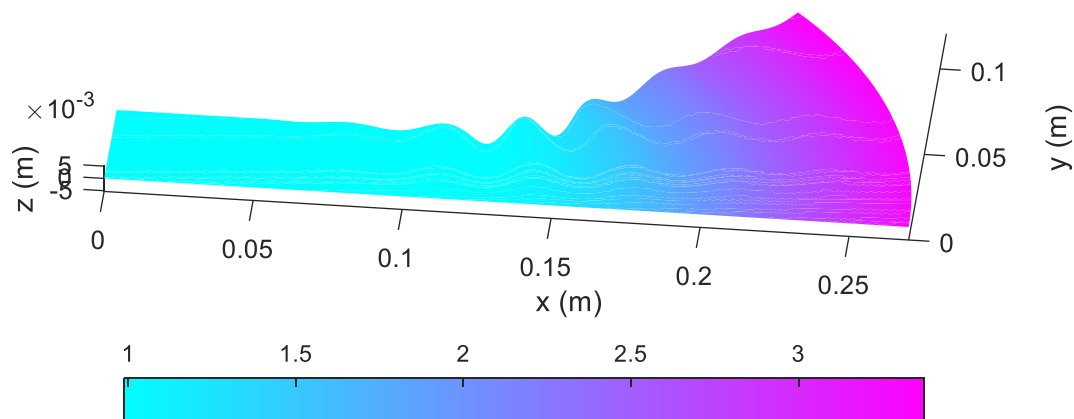


Figure 60:  $s_\alpha$  on channel-wedge geometry with optimised sinusoidal corrugations

Figure 60 shows  $s_\alpha$  computed on the pathlength optimised geometry. The range is significantly less than in the unoptimized geometry in Figure 58, which suggests that the corrugations are helping to correct the relative pathlength through the geometry. The biggest variations in  $s_n$  are seen at localised spots on the largest corrugations.



**Figure 61:  $a_f$  on channel-wedge geometry with sinusoidal shape pathlength optimisation**

$a_f$  on the optimised channel-wedge shell geometry is shown in Figure 61. It appears relatively unchanged compared to Figure 28, and indicates that the cross-sectional area increases in the wedge section.

## 6.4 Optimisation test case – S-bend

Figure 62 shows the S-bend geometry with pathlength optimisation using sinusoidal shaped corrugations. The sharp change in curvature between the two curved sections makes  $s_n$  rapidly switch sides at this transition point (see Figure 19). This causes the central corrugations to have a strange shape as they suddenly disappear and reappear on the opposite side of the channel.

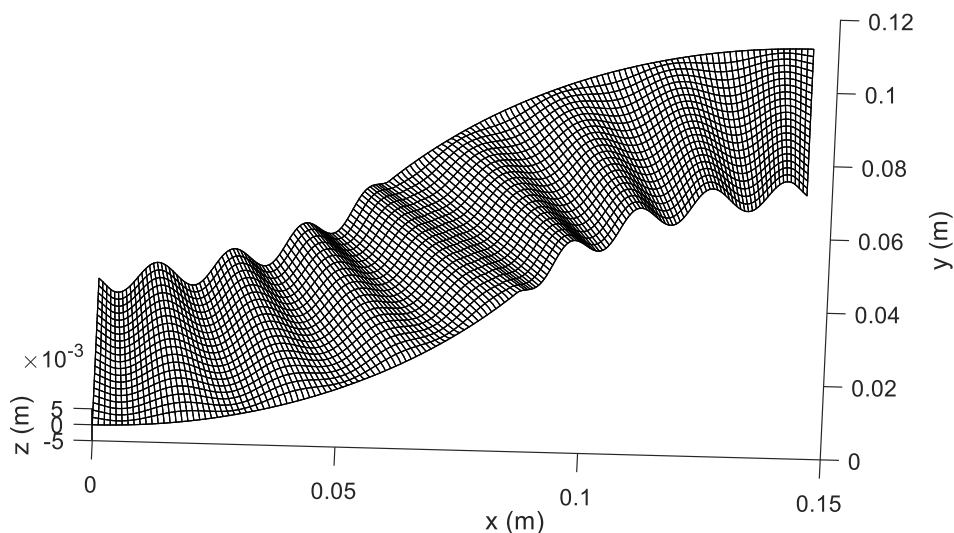


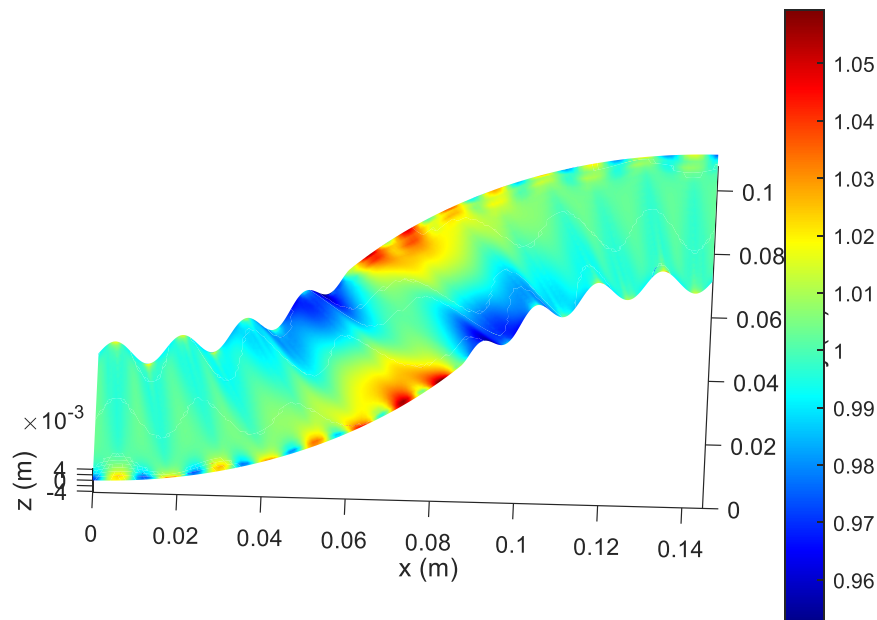
**Figure 62: Modulated s-bend shell mesh with sinusoidal shaped corrugations,**

Sharp changes like this in  $s_n$  can be problematic as the relative pathlength may not be accurately corrected for especially when using sinusoidal corrugations with a large period or wavelength (see section 6.1.3). This is most likely why much of the error shown by the  $s_n$  on

the pathlength optimised s-bend model in Figure 62 is near to the transition between the two curved sections.

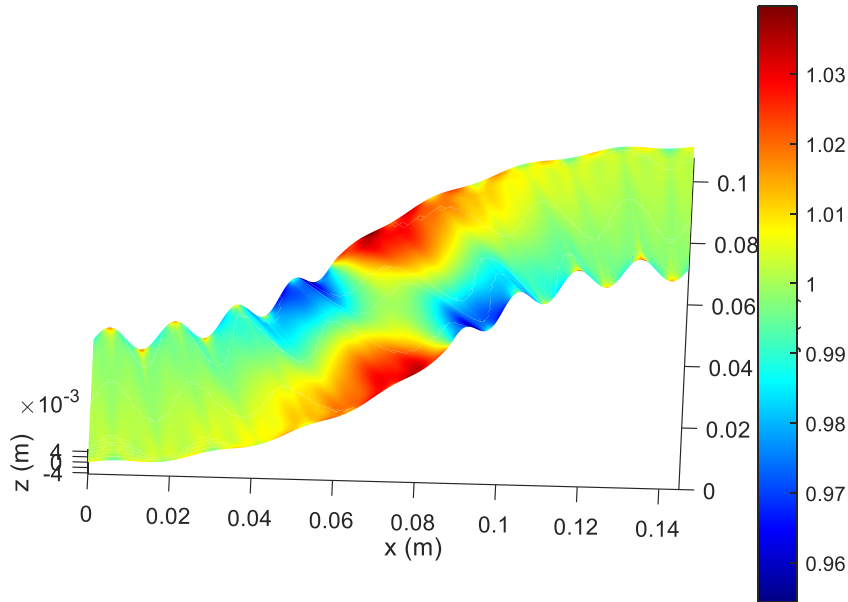
Due to this the S-bend is an awkward design to optimise. A test case with a continuous curvature like the half sine is much more forgiving when correcting the relative pathlength with corrugations.

Figure 63 shows that  $s_a$  is much closer to unity on the modulated shell mesh than on the 2D flat domain, which indicates error in the relative pathlength has been reduced and the design will be better at supporting 1P wave propagation.



**Figure 63: Average stretch  $s_a$  on s-bend with optimised sinusoidal corrugations,  $s_o = 0$**

Like with the other corrugation test cases there are underlying cyclic patterns seen in  $s_a$  because using sine wave shape corrugations adds pathlength in a cyclic manner. There are also intense spots close to the outside edges of each curved section due to the mesh curling around towards being flat.



**Figure 64: Average stretch  $s_a$  on s-bend with sinusoidal corrugations,  $s_o = 0.01$**

Figure 64 shows the average stretch  $s_a$  on the s-bend but with a stretch offset of  $s = 0.01$ . Similar to the in-plane bend example, the stretch offset helps reduce the mesh curling effect and there is therefore less error shown in  $s_a$  close to the edges.

## 6.5 Conclusions

This chapter investigates using the waveguide correction technique outlined in the GP Acoustics patent EP3806086A1 (Dodd & Oclew-Brown, 2021) on thin shell domains.

Triangular shaped corrugations can be used to add the exact amount of required extra pathlength at each point through a geometry due to the simple relationship between arc length and gradient or amplitude (see Eq. (38)). However, the sharp corners at the peaks and troughs of the triangular shape cause intense localised error in the waveguide metrics on the corrugated shell geometry.

In contrast, the ever-changing periodic gradient of sinusoidal shaped corrugations causes a periodic error in the added pathlength which is dependent on the period (length) of the corrugations. The smoother shape (marked by a lower maximum curvature) results in a bigger reduction in metric error on the corrugated shell mesh than with the triangular shaped corrugations. These results therefore suggest that sinusoidal shape corrugations are the best choice for equalising the relative pathlength through a geometry.

On a shell domain, the corrugation technique is consistently found to reduce difference in the relative pathlength through a domain highlighted by the stretch metric  $s$ , and is also found to reduce area error shown by  $a_f$ .

In some examples adding a stretch offset  $s_o$  can further reduce error in the waveguide metrics because it reduces the mesh curling effect found at the transition point between having (and not having) modulations at the edge of a domain.

## 7. Three-dimensional geometry

Unlike an infinitely thin 2D planer or shell domain, a 3D domain has a third dimension (its thickness) that can be used to adjust the cross-sectional area and correct changes indicated by the felt area metric  $a_f$ . This chapter first investigates iteratively adjusting the thickness to change the cross-sectional wavefront area and correct error shown by  $a_f$ . It then explores several other test cases.

### 7.1 Correcting for area – Iterative rectangular cuboid example

To experiment with optimising the change in area through a domain, a rectangular cuboid was modelled and deformed by adding a central lump in the  $z$  axis direction. Using this shape as a test case meant there was a clear end goal for the optimisation. If there was to be no change in felt area from entrance to exit, then the optimised geometry would tend to a simple cuboid. This makes it easy to tell if the iterative area correction process is converging and reducing the error in  $a_f$ .

Two opposing sides were chosen as the entrance and exit of the geometry and were given Dirichlet boundary conditions of 0 and 1 respectively for calculating Laplace's solution in the FEA solver. After the solution to Laplace's equation  $u$  was calculated, streamlines of  $\nabla u$  were traced through the domain. Using  $u$  and the streamlines, the felt area metric  $a_f$  was calculated over the domain. Finally, the thickness was adjusted using  $a_f$  to create the geometry for the next iteration. The process was repeated to try and reduce the change in area indicated by  $a_f$ . The thickness for each iteration was calculated as:

$$t_{n+1} = \frac{t_n}{a_f}, \quad (43)$$

where  $t_n$  is the thickness on the current iteration,  $t_{n+1}$  is the thickness on the next iteration and  $a_f$  is the felt area on iteration  $n$ .

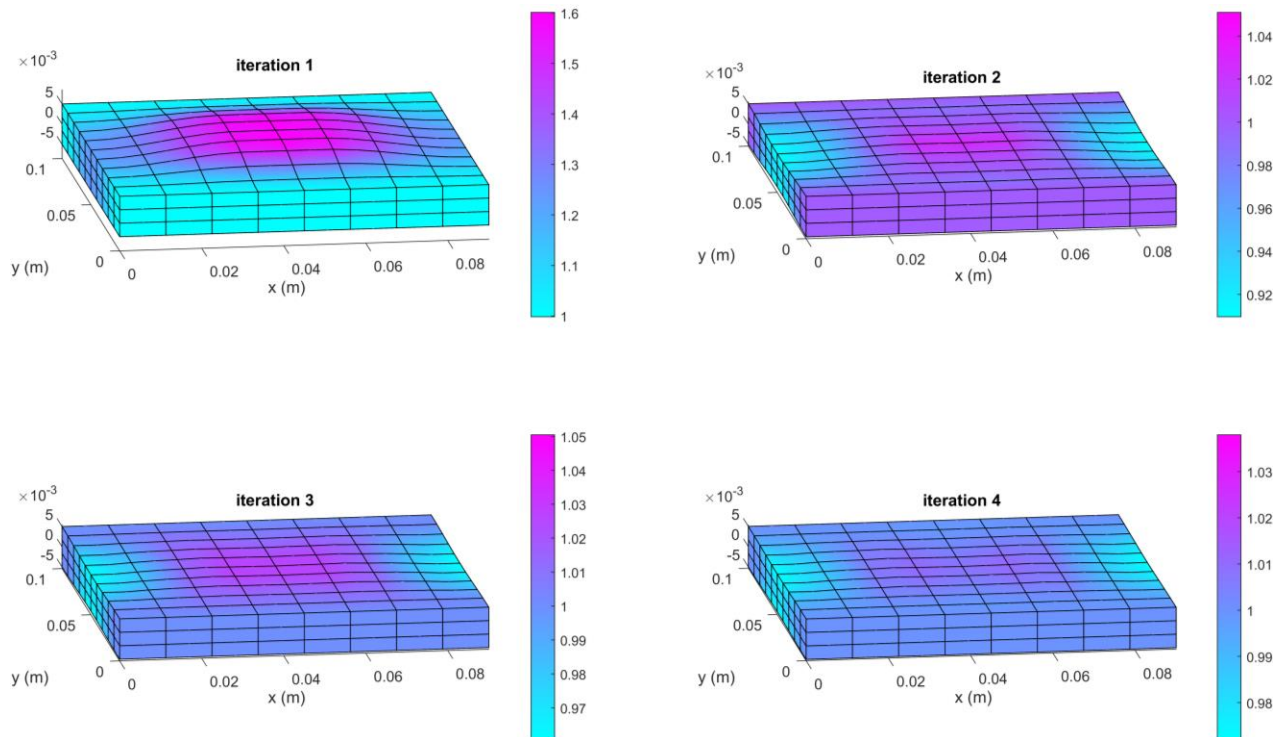


**Figure 65: Felt area  $a_f$  on four iterations of area optimisation of a distorted cuboid (note different scales on each plot)**

Figure 65 shows how the area correction causes the domain to become more like a perfect cuboid on each iteration.

One reason the optimisation works so well is that the cuboid's area deformation is only in the  $z$  direction and on each iteration the adjustment to the thickness is also just in the  $z$  direction. A model where the domain expands in multiple directions would be more difficult to optimise as it may be unclear in which direction to shrink or expand the geometry and correct the area. It is also interesting to observe the streamlines on each iteration. Figure 66 plots the streamlines on iterations one to four. Initially the streamlines bend inwards towards the bulge, but the distortion is reduced by each iteration and they become increasingly aligned.

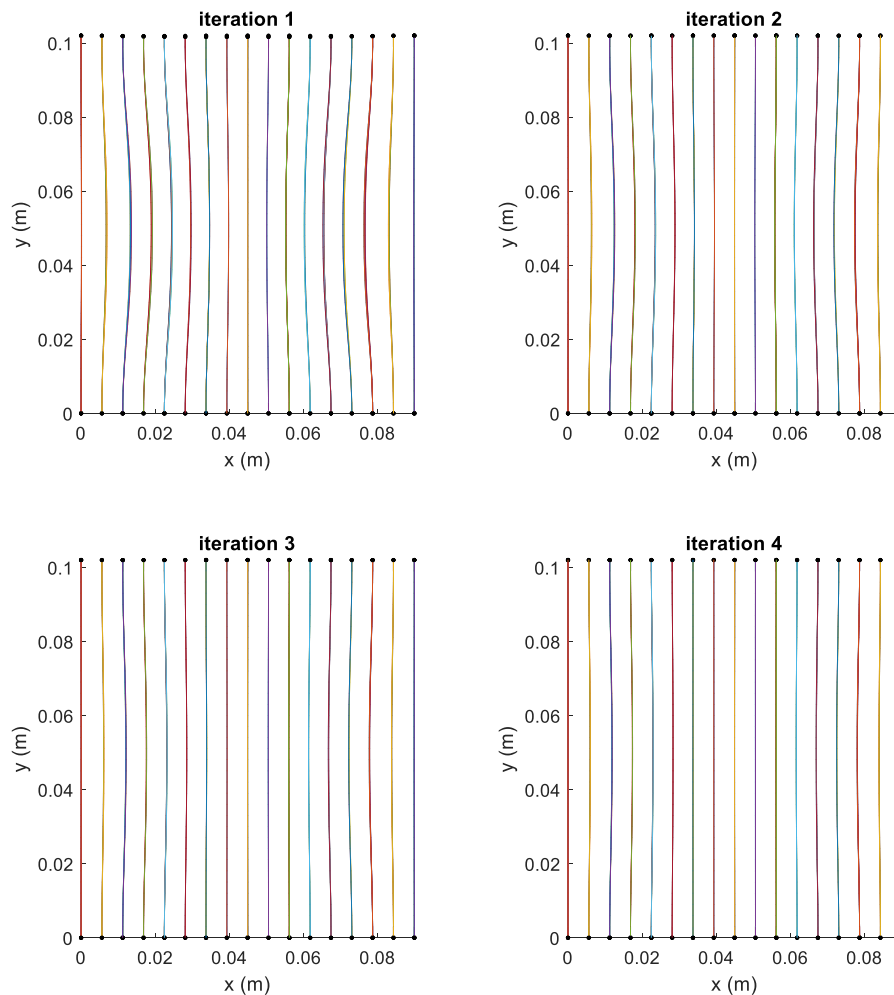


**Figure 66: Traced streamlines through distorted cuboid on iterations of area optimisation.**

## 7.2 Acoustic performance of a single thickened corrugation

Moving from shell meshes into 3D meshes allowed the acoustic performance of the optimised modulated domains to be simulated in the FEA solver. However, before looking at simulations of 3D pathlength optimised geometries it is first useful to investigate the acoustic performance of a single thickened corrugation in 2D, as this is fundamental to understanding how a corrugated geometry will behave acoustically. A 2D thickened corrugation is essentially a cross sectional cut of a corrugation in a 3D domain which makes it a particularly useful isolated test case for predicting the behaviour of more complex 3D models.

FEA was used to simulate the Helmholtz wave equation over a range of different frequencies. The entrance at one end of the corrugation was driven by a constant velocity. The exit on the opposing end was terminated with a  $\rho_0 c$  impedance. The test was repeated while changing the parameters which control the corrugation shape to build an understanding of their effect.

The absolute error in the mean sound pressure level  $SPL$  between the entrance and exit surfaces was used to characterise the acoustic performance of the corrugation. The mean sound pressure level  $\overline{SPL}$  was computed over each surface as:

$$\overline{SPL} = \frac{1}{S} \int_S SPL \, dS, \quad (44)$$

where  $S$  is the cross-sectional surface area. The Error in  $SPL$  was then:

$$Error \, in \, SPL = \sqrt{(\overline{SPL}_m - \overline{SPL}_t)^2} \quad (45)$$

where  $\overline{SPL}_m$  and  $\overline{SPL}_t$  are the mean sound pressure level on the entrance (throat) and exit (mouth) surfaces respectively. If  $\overline{SPL}_m = \overline{SPL}_t$  then error in  $SPL = 0$  and the corrugation shape has had no effect on the mean transmitted  $SPL$ . This implies that the acoustic wave has travelled through the domain without interference.

In a pathlength optimised 3D domain if the corrugation shapes are interfering with the acoustic wave propagation, then the 1P wave propagation conditions will be jeopardised.

### 7.2.1 Sine shaped corrugation – amplitude and thickness

A sine corrugation of arbitrary length 45mm was simulated whilst changing its geometric parameters. Figure 67 shows the sine wave corrugation with several different illustrative amplitude and thickness settings, denoted  $A$  and  $T$  respectively.

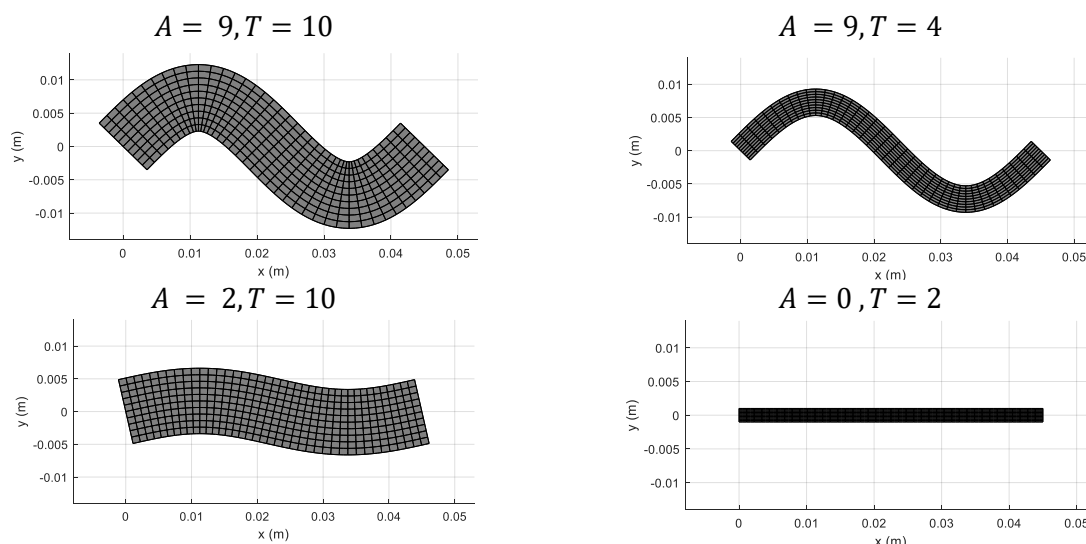


**Figure 67: A 45 (mm) Length Corrugation, A = Amplitude (mm), T = thickness (mm)**

Figure 68 shows the error in  $SPL$  through the simulated corrugation at different frequencies, amplitudes, and thicknesses, as a 3D plot. Errors are small, but it is worth bearing in mind that if a design had many corrugations the effect would be magnified. The simulated geometry was 45mm in length, but the results and frequencies could be scaled to a corrugation of any size.

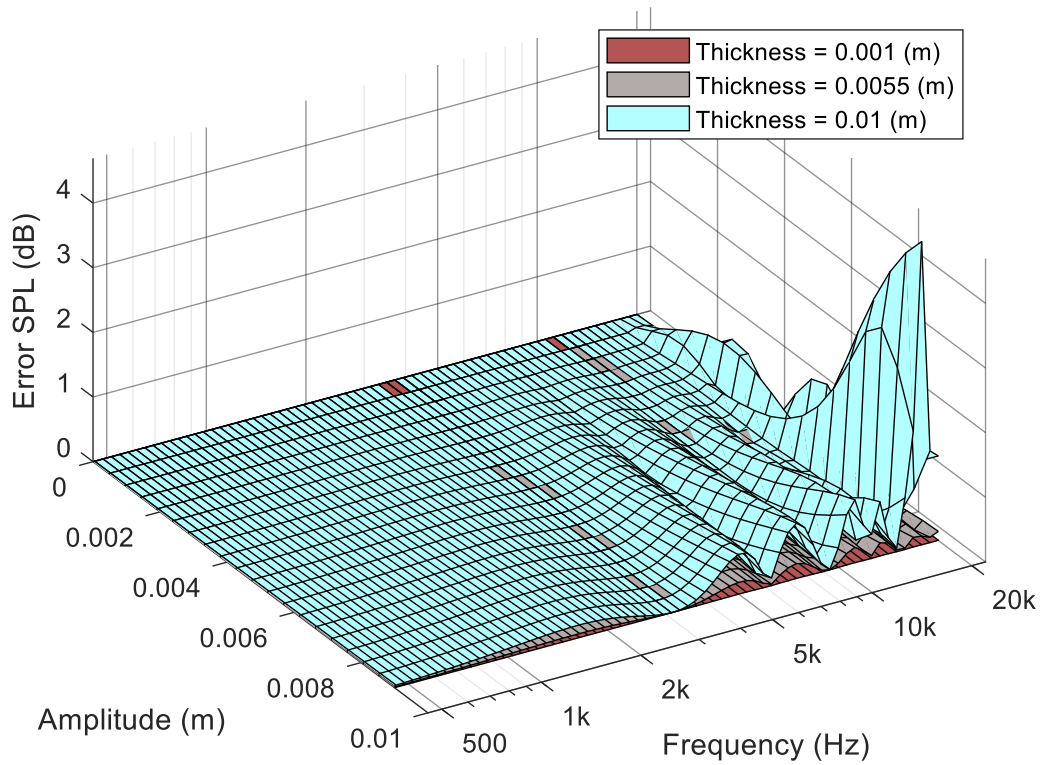


**Figure 68: Error in SPL through a single sinusoidal corrugation with different amplitude and thickness (45mm long)**

Error is significantly reduced at low amplitudes and low frequencies because the model is closer to a straight duct and wavelength is longer. A thinner domain has significantly better performance at all frequencies and corrugation amplitudes. This is because there is less room for transverse waves and interference. However, using a very thin duct may not be practical because of viscous effects, which aren't simulated here. Hence a compromised thickness must be found.

Another important quantity is the throat impedance of the waveguide, since this is what the compression driver has to couple to. A normalised throat impedance equal to the characteristic impedance of air ( $\rho_0 c$ ) is desirable. The throat impedance was calculated from the pressure and displacement on the surface at the entrance to the duct according to:

$$Z_t = \frac{p}{U}, \quad (46)$$

where  $p$  is the pressure and  $U$  is the volume velocity. This was then normalised to give:

$$Z_{tn} = \frac{Z_t S}{\rho_0 c}. \quad (47)$$

Figure 69 shows the normalised throat impedance. The resistance is plotted in lighter colours and is centred around one whereas the reactance is darker and centred around zero. It has similar characteristics to the absolute error SPL results in Figure 68. At low amplitudes and low frequencies, the throat impedance is fairly constant, implying the wave

propagation is more planer and less disturbed, whereas at high frequencies perturbations occur. Also, a thinner geometry (shown in red) has a much more constant throat impedance compared to a thicker geometry.

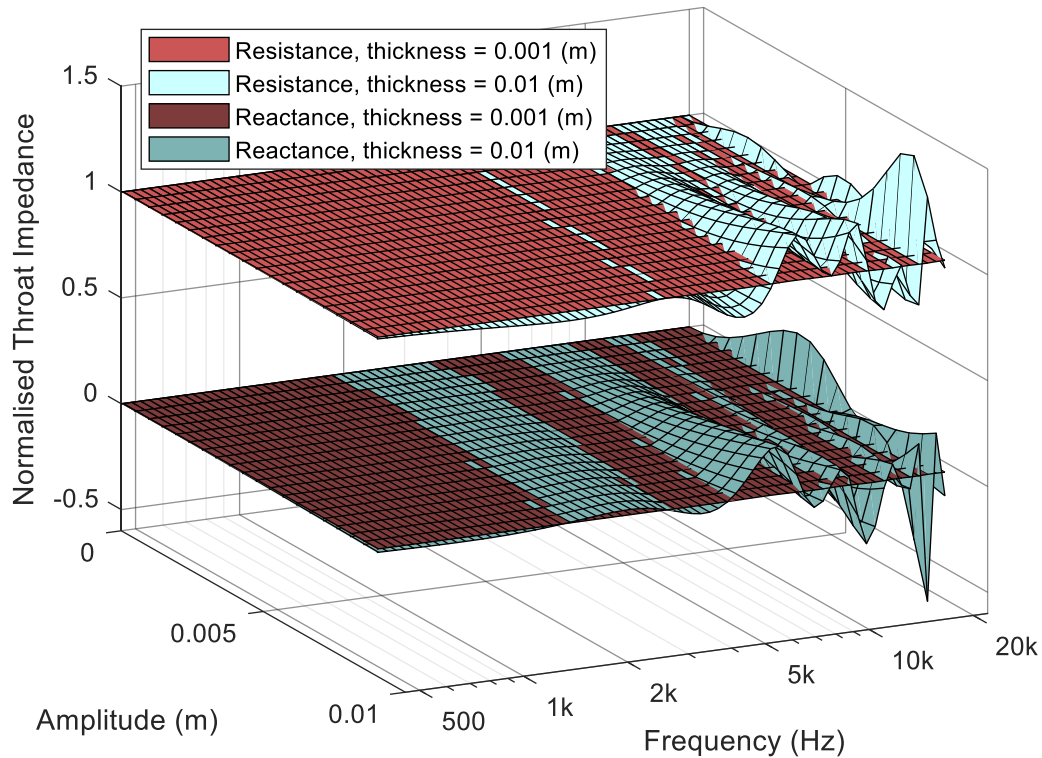


**Figure 69: Normalised acoustic throat impedance for a single corrugation with different amplitude and thickness, (45mm long)**

The throat impedance and the absolute error in *SPL* both appear capable of indicating the extent to which a corrugation shape affects the transmitted pressure wave. Because they both lead to the same conclusions, in this dissertation only the absolute error in *SPL* is shown for the rest of the simulations of a single thickened corrugation.

### 7.2.2 Sine shaped corrugation – length and thickness

Another similar test case was investigated in which the length and thickness of the corrugation were changed while the amplitude remained the same (9mm) for each simulation. Figure 70 shows some example geometries with different lengths and thicknesses,  $L$  and  $T$  respectively.

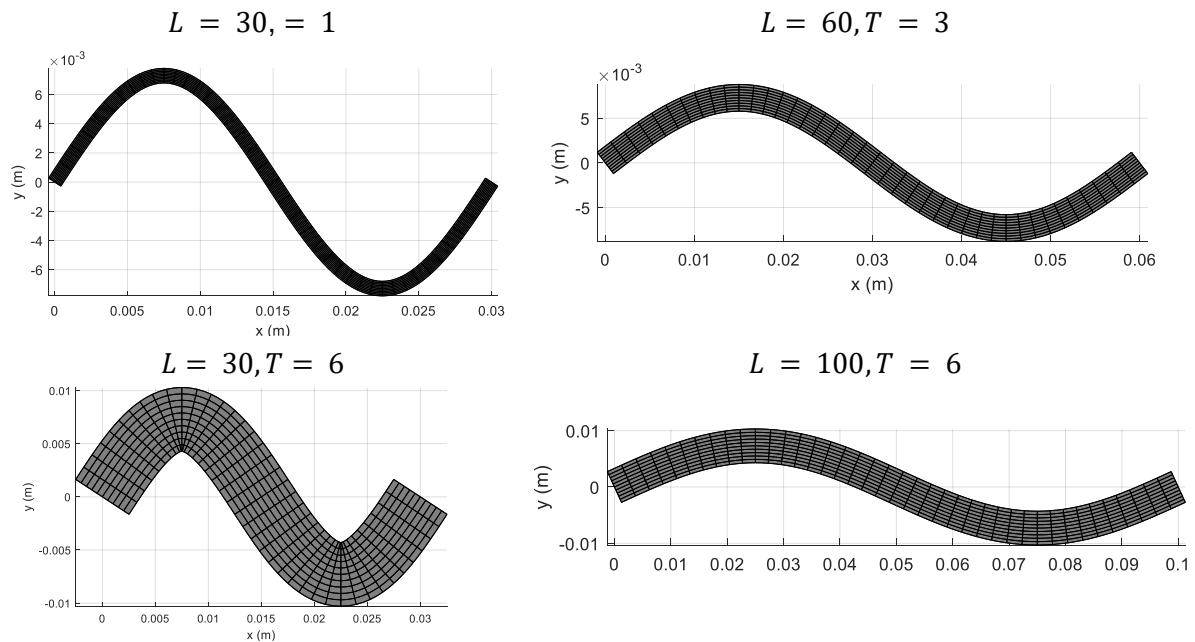


**Figure 70: Examples of sinusoidal corrugation with different lengths and thickness**

Figure 71 shows the error in  $SPL$  between each end of the corrugation when changing the length and thickness. Lengths from 30mm to 100mm were tested. Like in the amplitude test case, a thinner domain is almost always better.

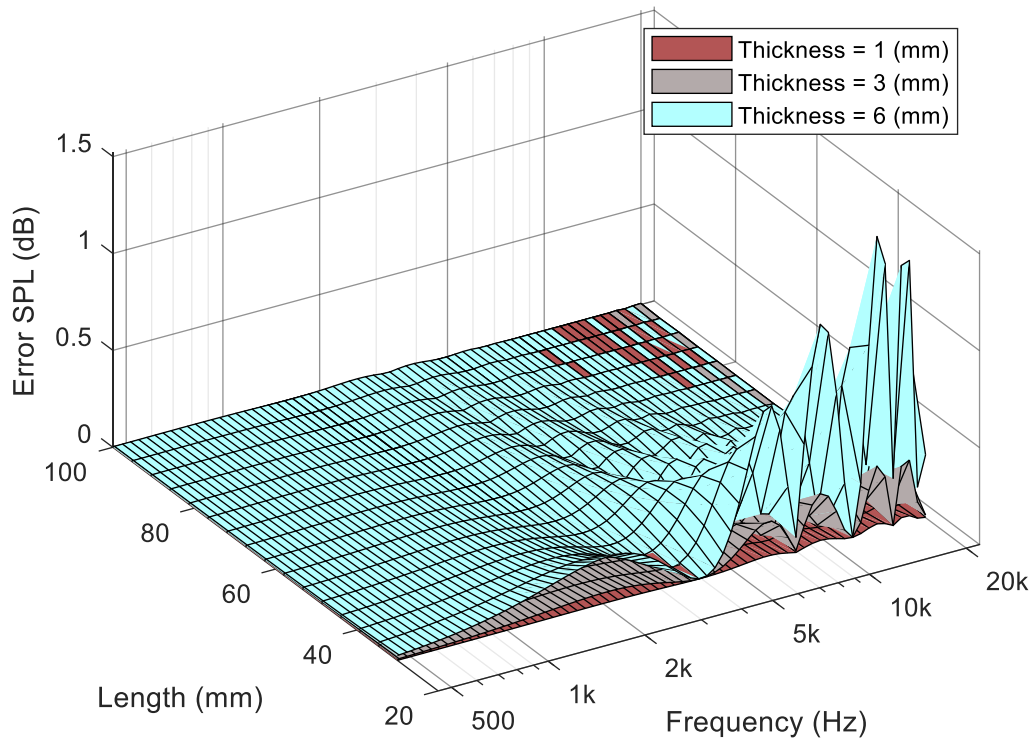


**Figure 71: Absolute error in  $SPL_a$  from a single sinusoidal corrugation with different lengths and thickness (amplitude = 9mm)**

A shorter corrugation of the same amplitude results in more error especially at high frequencies. This is because the acoustic channel turns sharper corners (and therefore has higher curvature) which causes more reflections of the pressure waves from the boundary.

### 7.2.3 Triangular shaped corrugation – Fourier series

To investigate the performance of triangular corrugations a Fourier series was used to morph the corrugation shape from a sine wave towards a triangle wave. The Fourier series for a triangle wave is:

$$y(x) = A \frac{8}{\pi^2} \sum_{n=1,3,5,\dots}^{\infty} \frac{(-1)^{\frac{n-1}{2}}}{n^2} \sin\left(\frac{n\pi x}{L}\right), \quad (48)$$

where  $L$  is the period of the wave and  $n$  is the harmonic order.

A single thickened corrugation was parameterised so that the acoustic performance could be simulated with varying numbers of Fourier harmonics. Figure 72 shows a wave which is 45mm in length and 6mm thick with different numbers of Fourier triangle harmonics  $H$ .

As the number of harmonics increases the corners become sharper and the shape increasingly resembles that of a triangle wave. Amplitudes ranging from 0 to 6mm and corrugations with 1,3 and, 5 Fourier harmonics were used for the simulations.

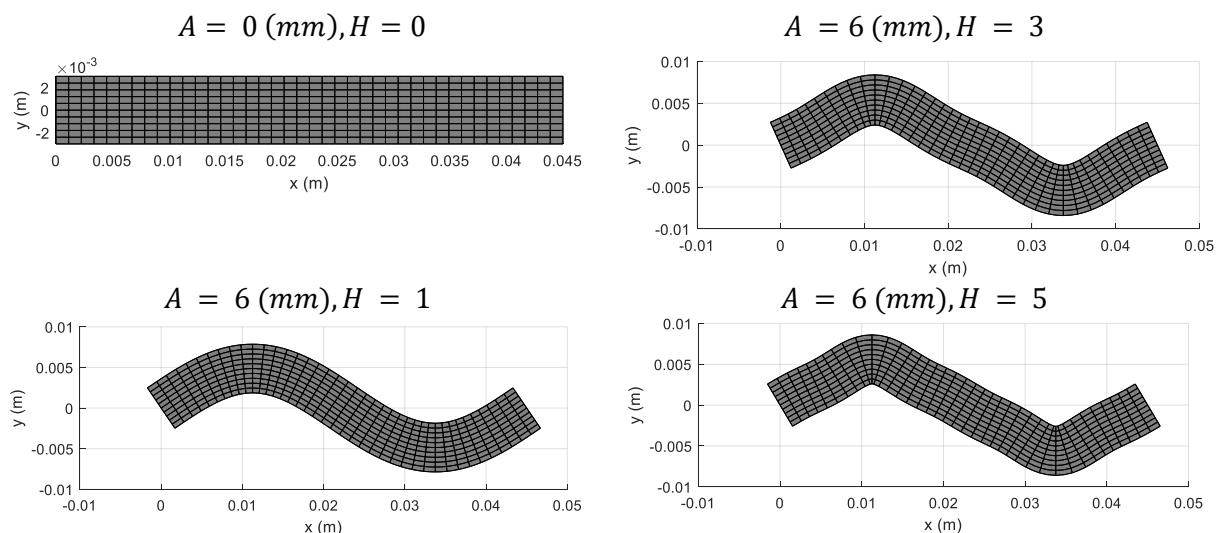


**Figure 72: Example corrugations with different numbers of Fourier triangle wave harmonics, 45mm length, 6mm thick.**

When using a quadrilateral swept mesh, as seen in Figure 72, with enough Fourier harmonics the thickness will cause the domain to fold in on itself. The parameter limits for the test were chosen so that this wouldn't happen as it makes the mesh invalid for FEA use. It would be possible to simulate a thickened triangle wave with more Fourier harmonics if a free tetrahedral

mesh was used instead. However, the experiment still gave a good indication of the acoustic characteristics of a thickened triangle wave, and the effect would likely be exaggerated with more harmonics

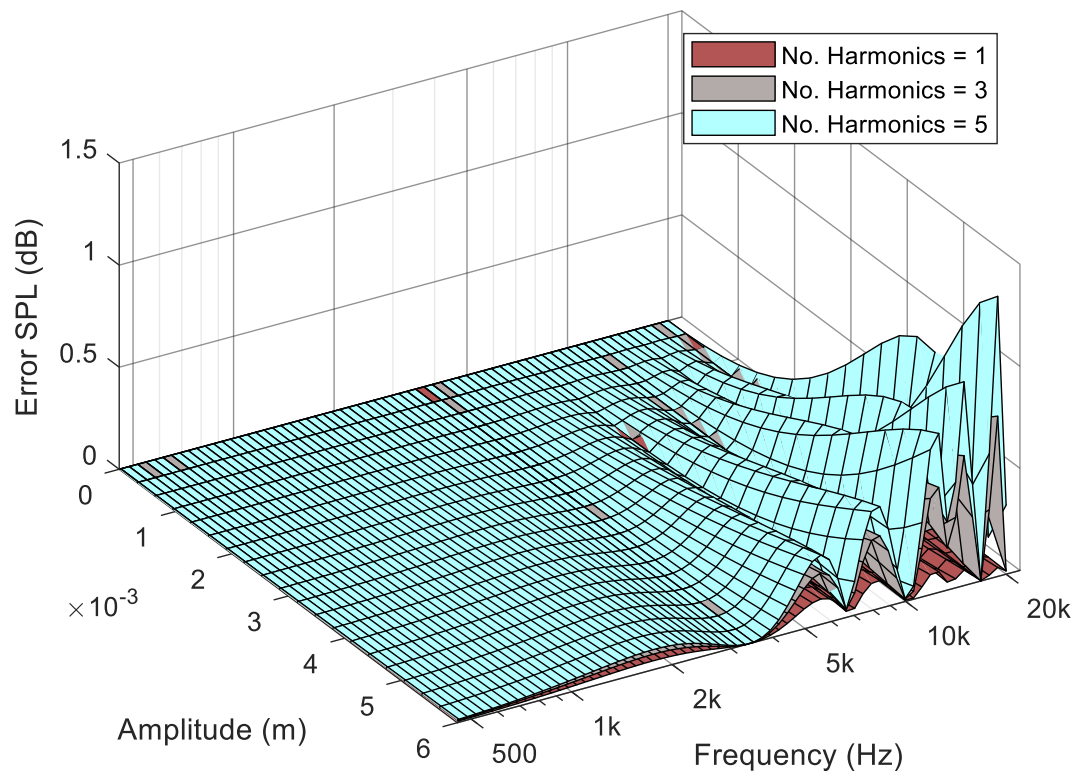


**Figure 73: Absolute error in *SPL* from a single corrugation with varying amplitude and number of Fourier triangle harmonics. 45mm long, 6mm thick**

Figure 73 shows the absolute error in sound pressure level for a corrugation with varying numbers of Fourier harmonics and amplitudes. Like the thickness test in Figure 68, lower amplitudes have less error because the domain is straighter. At almost all frequencies and amplitudes the model with more Fourier harmonics has more error. This is probably because the higher curvature in the propagation path at the peaks and troughs of the corrugation disrupts the high frequency plane wave propagation more significantly.

Figure 74 shows the maximum curvature of a central line through the corrugation with different amplitudes and numbers of Fourier harmonics. There is clear correlation between the Error in SPL shown in Figure 73 and the maximum curvature, which implies that a higher curvature or sharper corner in the sound propagation path will introduce more interference to the transmitted pressure waves.

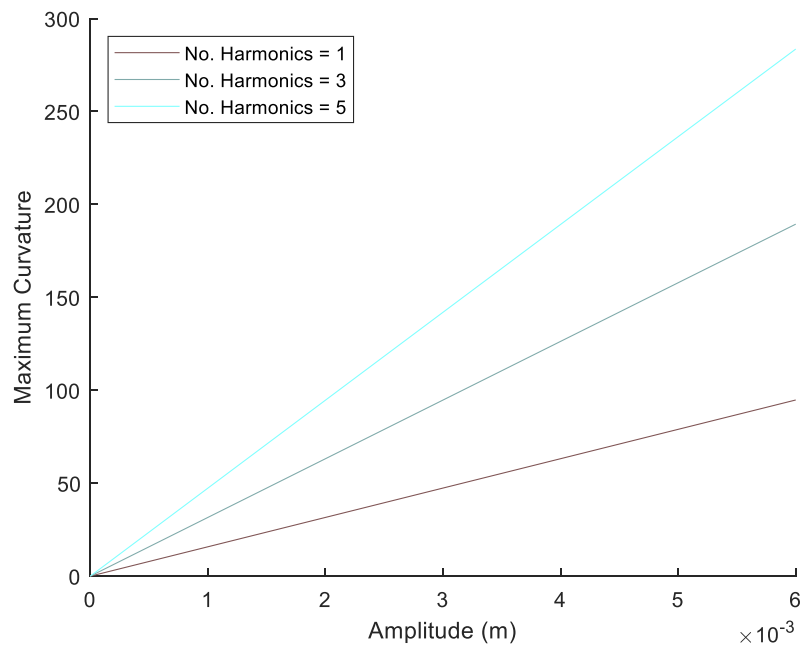


**Figure 74: Maximum curvature of corrugations with different amplitudes and no. of Fourier harmonics**

The results of all the simulations of a corrugation with different geometric parameters (Figure 68, Figure 71, and Figure 73) lead to the general conclusion that to get less error in the *SPL* transmitted through the corrugation, the corrugation shape should be thinner and have gentler corners (lower curvature) in the sound propagation path. This can be achieved both by using sinusoidal corrugations of smaller amplitude and/or of larger wavelength.

### 7.3 Creating 3D modulated domains

Converting a shell mesh into a 3D mesh was done by computing vectors normal to the surface at each node on the domain and then lofting equally in the positive and negative direction to extrude into a 3D domain where the central surface is the same as the original shell domain. Figure 75 shows an example of the surface normal vectors at each node on a coarse shell mesh of the half sine with three corrugations.

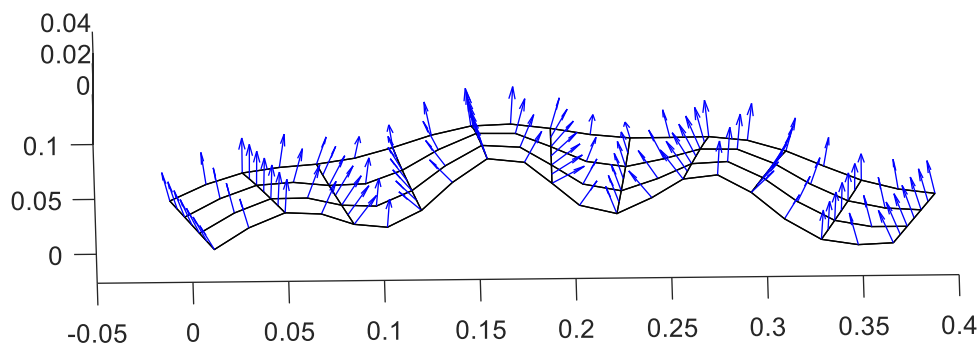


**Figure 75: Example surface normal vectors on a coarse undulated half sine mesh**

A target cross sectional area  $a_T$  was used to control the base thickness  $t_b$  through the geometry as a function of  $\xi_n$ .  $a_t$  could be constant or could change through the domain creating an expansion from entrance to exit. Adjusting the expansion allows the throat impedance to be customised. The base thickness  $t_b$  was calculated from the target area  $a_t$  as

$$t_b(\xi_n) = \frac{a_t(\xi_n)}{w(\xi_n)} \quad (49)$$

where  $w$  is the width of desired 1P wavefront in the domain. In a design which has no expansion, such as the S-bend,  $w$  is simply the constant width of the domain. However, in a geometry like the channel-wedge it can be less clear how to define  $w$  as the wavefront shape changes through the domain.  $w$  was therefore calculated from the arc length of isolines of  $\xi_n$  across the shell geometry. Figure 76 shows an example of  $\xi_n$  isolines on the Channel-Wedge Geometry. The isolines are equally spaced along the longest  $\xi_r$  path and are parallel to the desired 1P wavefront.

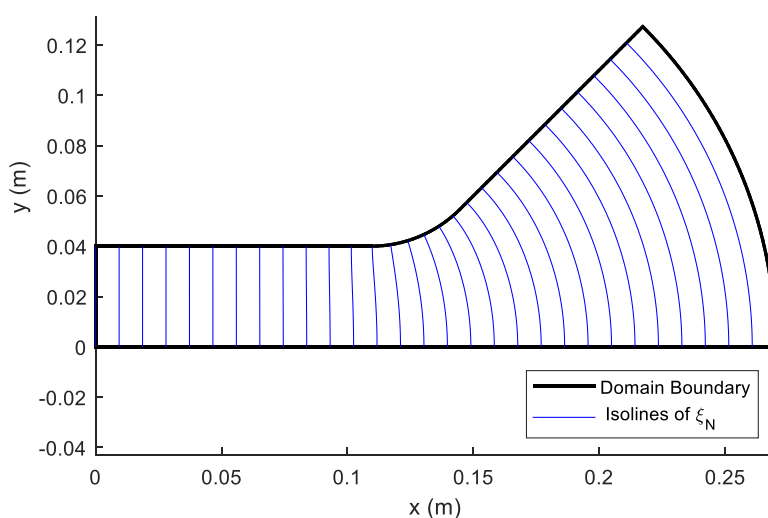


**Figure 76: Isolines of  $\xi_n$  in channel wedge geometry**

$w$  could also be normalised to the throat width  $w_t$  to give the relative change in width  $w_n$ :

$$w_n(\xi_n) = \frac{w(\xi_n)}{w_t}. \quad (50)$$

Figure 77 shows an example mesh which has a linear expansion in area from left to right. The original shell geometry is shown in grey.

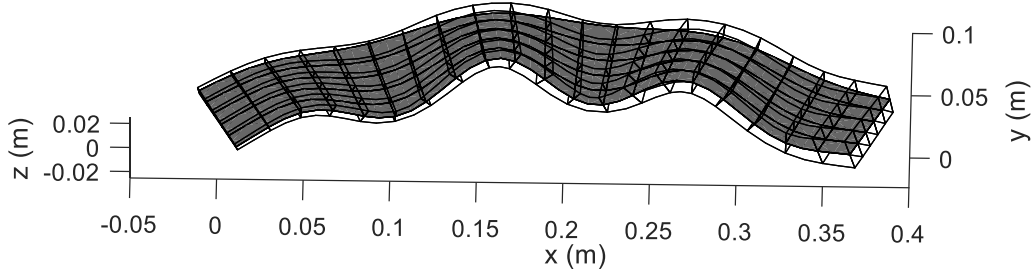


**Figure 77: Example 3D mesh with linear expansion from left to right**

The thickness can also be adjusted spatially using the felt area metric  $a_f$  from the shell domain simulations, to further optimise specific parts of the waveguide. A thickness correction  $t_c$  is calculated as:

$$t_c = \frac{w_c(\xi_n)}{a_f}. \quad (51)$$

If the domain has constant width, such as with the half sine geometry, then  $t_c$  is simply  $1/a_f$ . The area optimised thickness is then:

$$t_o = t_b(\xi_n) \times t_c. \quad (52)$$

Here  $t_b$  is the base thickness as a function of  $\xi_n$  and  $a_f$  is the felt area from the shell domain simulation. Helmholtz acoustic simulations were done with and without the additional thickness optimisation to investigate if it was beneficial.

## 7.4 Acoustic simulations of optimised geometry

To understand the effectiveness of the pathlength and area optimisation techniques, FEA simulations of the Helmholtz wave equation were performed on the 3D geometries. The domain was excited by a constant velocity over the entrance surface and was terminated with a  $\rho_0 c$  boundary condition on the exit surface.

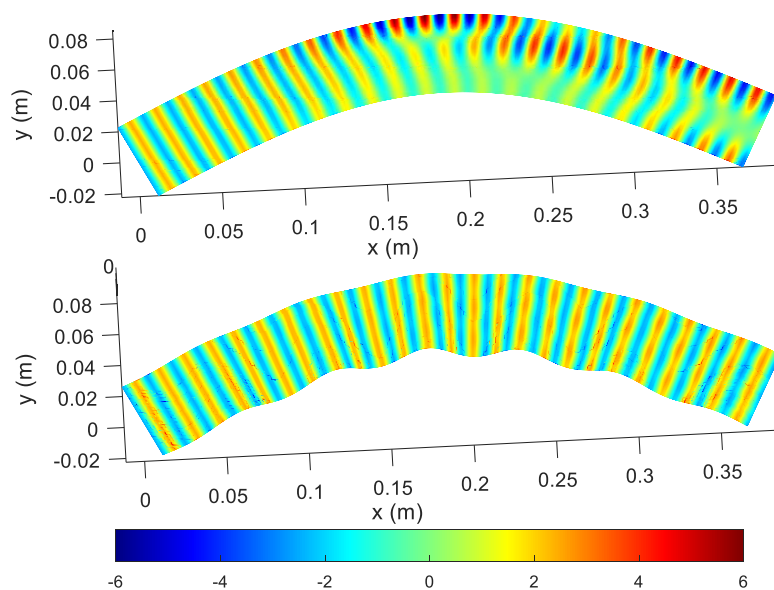
To characterise the acoustic performance across a wide range of frequencies the maximum range of the SPL was calculated over all nodes on the exit surface of the geometry. If the range of the SPL is zero it implies that the pressure wave at the mouth is completely uniform and that no cross-modes have been excited.

Unless specified otherwise the modulated geometry had both pathlength and thickness optimisation applied.

#### 7.4.1 Acoustic performance of the half sine

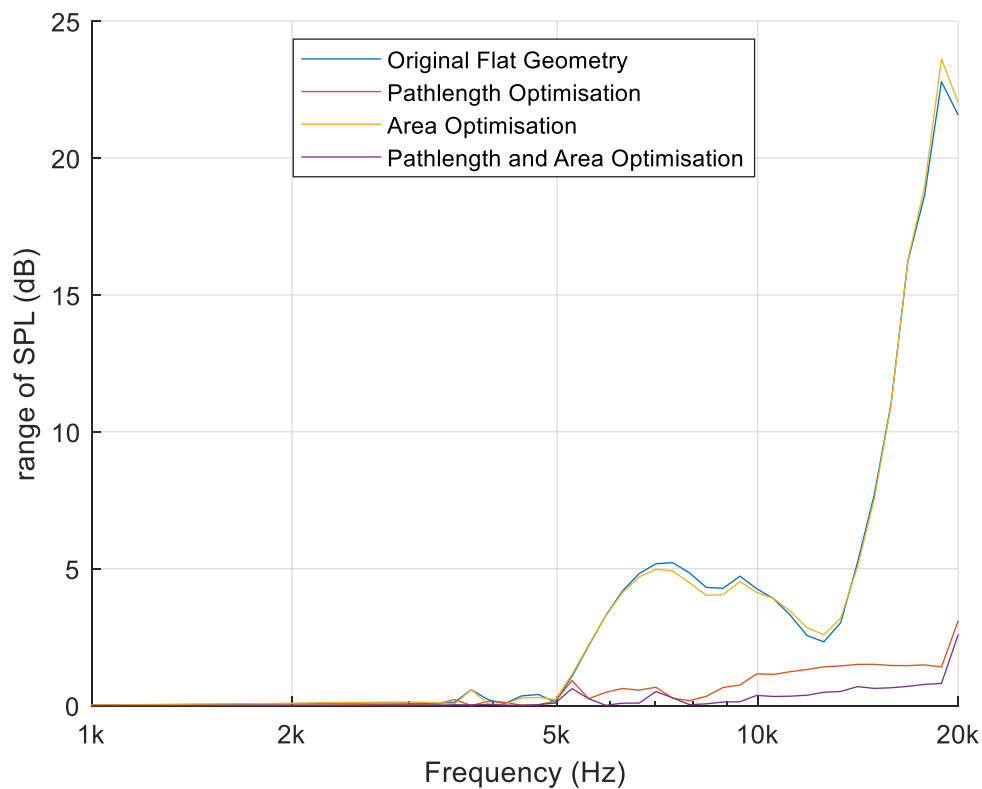
First the half sine geometry was investigated because it is a simple model that allows for a clear insight into of the effects of the geometric parameters. All the optimised half sine models had a stretch offset  $s_o$  of 0.01 to avoid the abrupt curl in the mesh seen in Figure 54.

Figure 78 shows the pressure response at 20Khz with and without pathlength and thickness optimisation. In the original flat model, the bend in the geometry causes the pressure to intensify on the outside edge, and the pressure response at the mouth (right boundary) is clearly uneven. In contrast, the pressure response on the optimised model is much more aligned throughout the geometry.



**Figure 78: Pressure response at 20Khz for the half sine geometry. top: with no optimisation bottom: pathlength and area optimisation ( $t_b = 1mm$ ,  $n_{mod} = 6$ )**

Figure 79 shows the range of SPL across the mouth for the half sine with different optimisation techniques. Frequencies lower than 1kHz have not been included as the larger wavelengths mean there is plane wave propagation regardless of the additional optimisation.



**Figure 79: Range of SPL across the mouth on the half sine, optimised and un-optimised ( $t_b = 1$ ,  $n_{mod} = 6$ )**

The two models with pathlength optimisation perform significantly better than the original flat geometry over all frequencies. Interestingly, the model with only area optimisation is worse than the original flat geometry for some frequencies.

The geometry with both pathlength and area optimisation performs best, with a maximum range of SPL of around 3dB at 20Khz and much less at lower frequencies. The pressure response of this is shown in the bottom of Figure 78, where just a very slight fluctuation in SPL can be seen across the mouth. These results suggest that the best technique is to optimise for both the pathlength and the area ( $s_n$  and  $a_f$ ) together.

#### 7.4.2 Effect of thickness on acoustic performance

To investigate the effect of the thickness of the acoustic performance, simulations of the same half sine geometry were done with different base thickness  $t_b$  values.  $t_b$  was kept constant through the geometry, so there was no expansion, and the final thickness  $t_o$  was calculated using Eq.(52). Figure 80 shows the geometry but with different values of  $t_b$ .

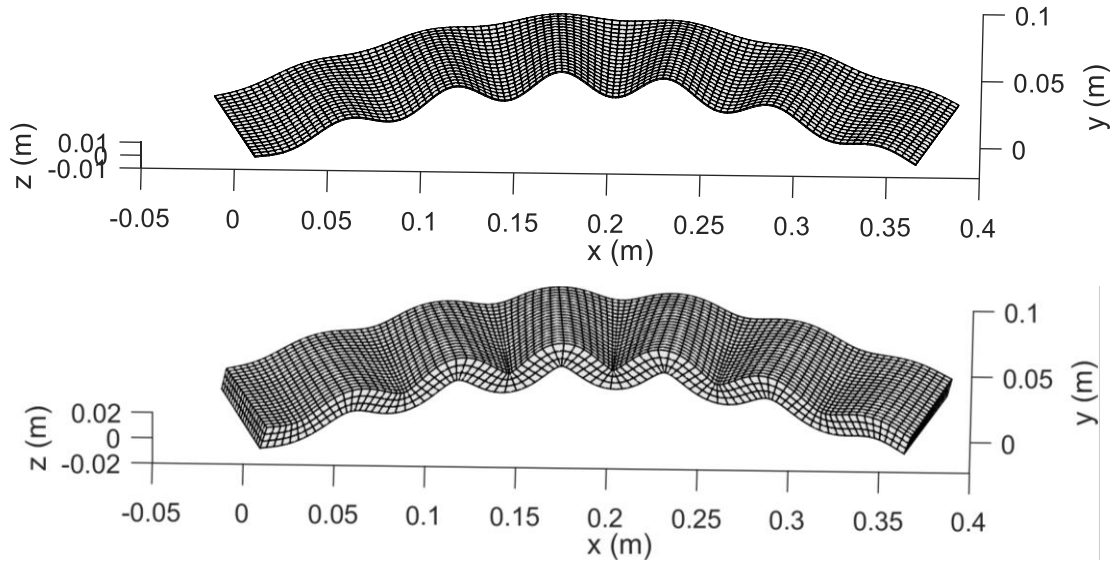


**Figure 80: 3D half sine geometry ( $n_{mod} = 6$ ), top:  $t_b = 0.5mm$ , bottom  $t_b = 15mm$**

Figure 81 shows the effect on the range of SPL for models with different base thickness  $t_b$ . In general, the thinner geometry performs better with the thickest geometry ( $t_b = 15mm$ ) performing significantly worse at all frequencies.

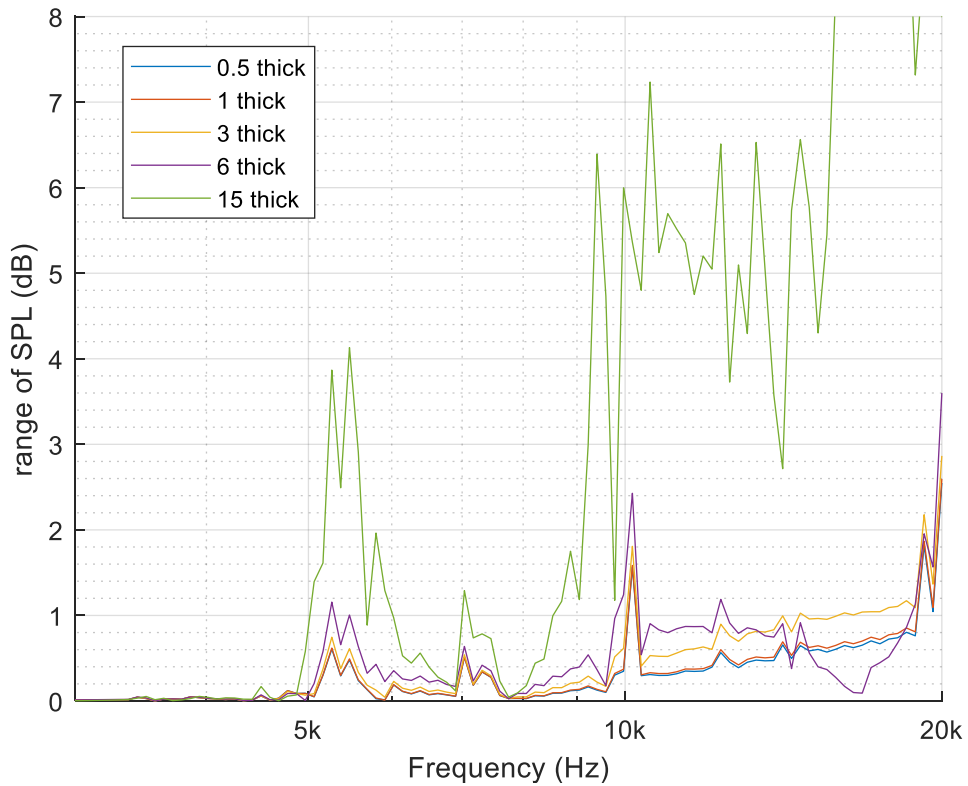


**Figure 81: Range of SPL across the mouth of the half sine with different  $t_b$ ,  $n_{mod} = 6$**

These results fit with the findings from the acoustic simulation of a single corrugation shown in Figure 68 where the thinner corrugation also produced much less error in the transmitted SPL.

### 7.4.3 Effect of the number of corrugations on the acoustic performance

To investigate the effect of the corrugation size on the acoustic performance, simulations of the same half sine geometry were performed with different numbers of corrugations. Figure 82 shows two meshes of the half sine geometry ( $t_b = 1mm$ ) with 2 corrugations and 9 corrugations. Having more corrugations in the same size geometry means that each corrugation is smaller in relation to the thickness and the domain width.

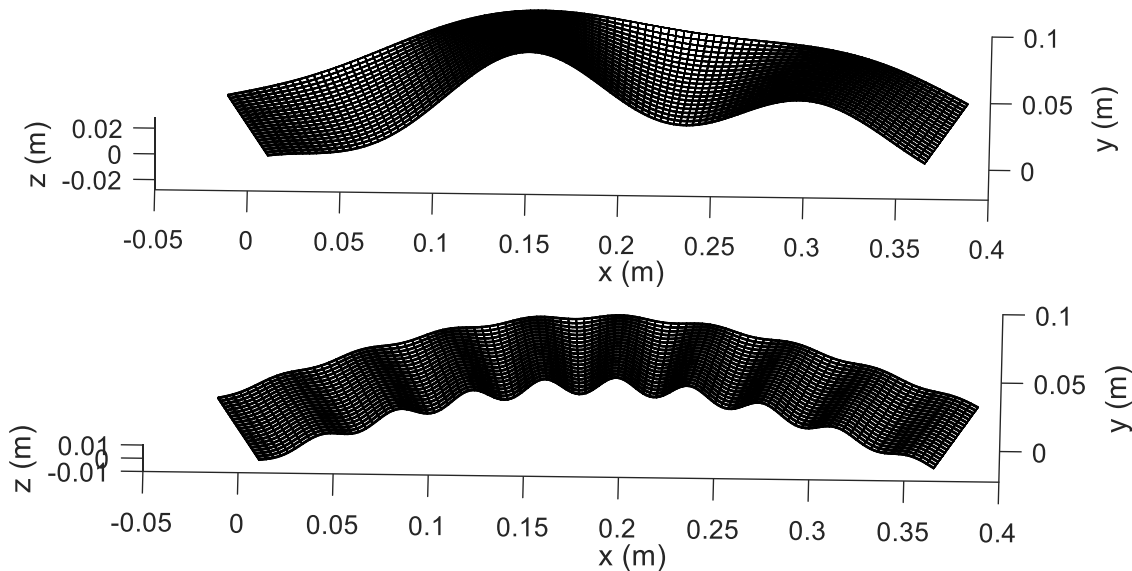


**Figure 82: In plane bend geometry ( $t_b = 1mm$ ), top:  $n_{mod} = 2$ , bottom:  $n_{mod} = 9$**

Figure 83 shows the range of the SPL for the half sine with different numbers of corrugations ( $t_b = 3mm$ ). In this design, below 8kHz having more corrugations works better with less harsh spikes highlighting problematic frequencies. Above 8kHz having more corrugations has a smoother range of SPL between frequencies but it seems as if there is a limit to how low the range of the SPL can go which increases with frequency and number of corrugations.

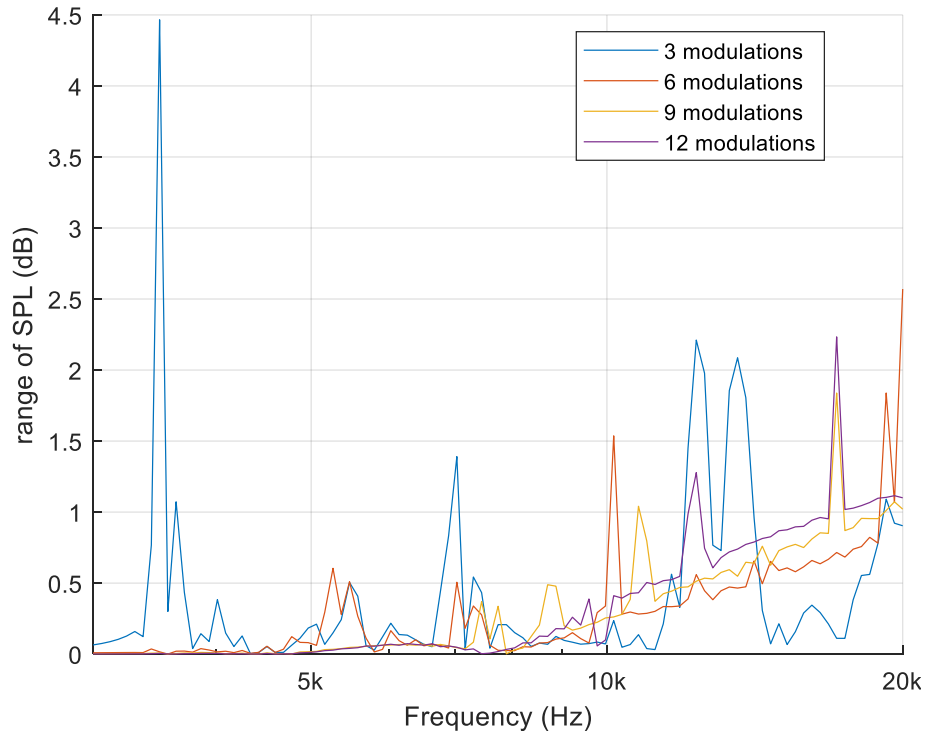


**Figure 83: Range of SPL for the half sine with different number of corrugations ( $t_b = 1mm$ ), pathlength and thickness optimisation)**

With more corrugations the length of each corrugation is smaller in comparison to the thickness and acoustic wavelengths. Therefore, the high frequency limitation which is seen when using more corrugations may be linked to the findings in Figure 71, which showed smaller shorter corrugations with the same thickness result in more error in the transmitted *SPL*.

More simulations were performed on the same geometry but with a thicker domain ( $t_b = 6mm$ ). This made the acoustic performance notably worse overall. The results, shown in Figure 84, suggest having either 3 or 6 corrugations is the better option, with the  $n_{mod} = 12$  model performing much worse. Again, this is likely linked to the findings shown in Figure 71. This is an interesting result for waveguides that feature large gradual deformations.

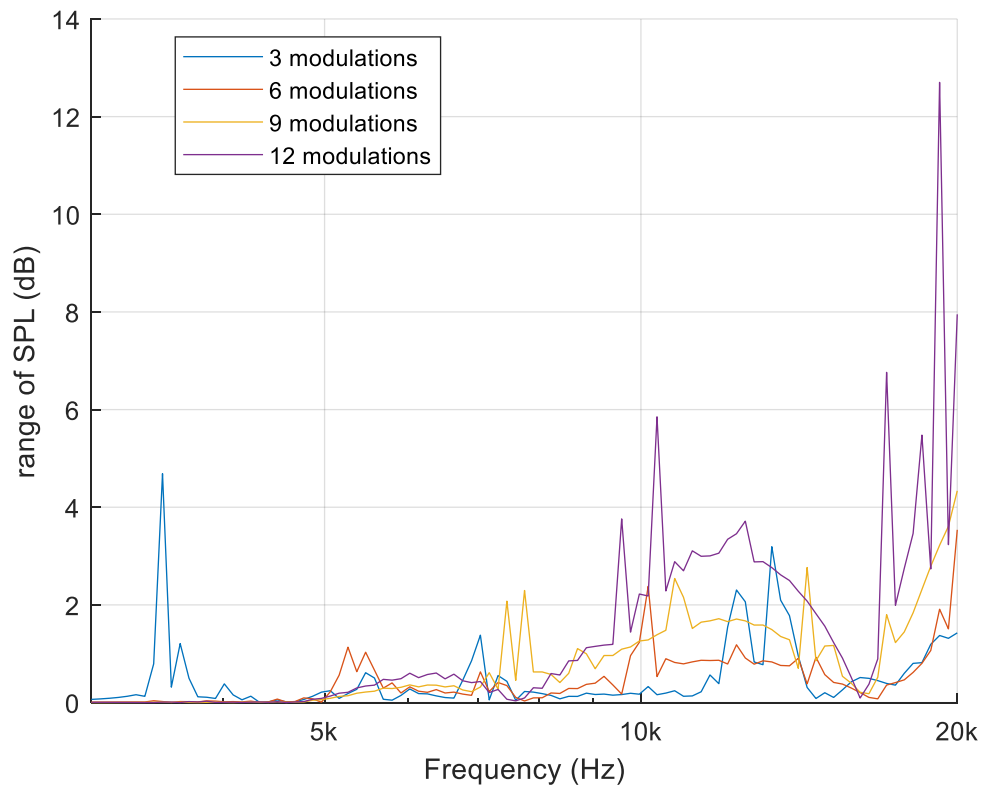


**Figure 84: Range of SPL for the half sine with different number of corrugations ( $t_b = 6mm$ , pathlength and thickness optimisation)**

Figure 84 is an interesting result, especially when compared with Figure 83, since it illustrates just how strongly the thickness of the domain can affect the acoustic performance. It also shows that changing the thickness on a particular geometry may result in a different number of corrugations reaching optimal phase coherent wavefront performance.

#### 7.4.4 Channel-wedge geometry

The channel-wedge geometry is an interesting test case because the design aims to create a transition between a rectangular plane wave in the channel section and a cylindrical wave in the wedge section. The wedge section causes the physical width of the 2D geometry to expand. This is shown in the felt area  $a_f$  in Figure 85 which is around one for the first channel section and then increases smoothly in the wedge section.

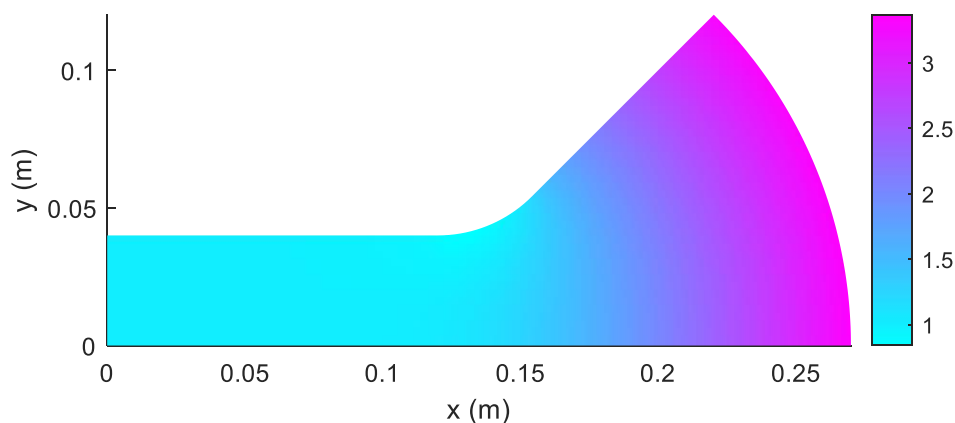
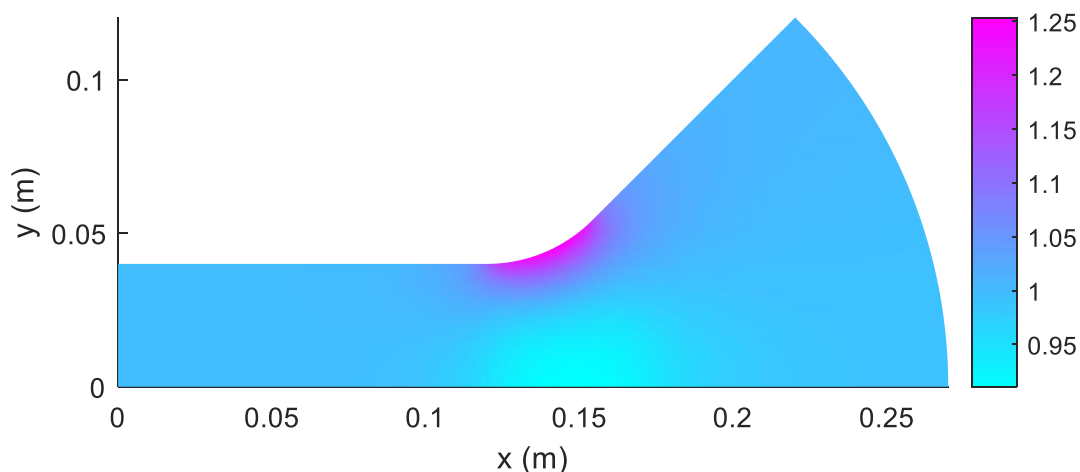


**Figure 85:  $a_T$  felt area on channel wedge geometry**

When correcting for the area in the channel wedge geometry, the resulting channel thickness would decrease towards the exit boundary to correct for the widening of the domain if the  $a_T$  was set constant. One option to avoid this is to give the domain a constant base thickness  $t_b$ .  $a_T$  can then be calculated by rearranging Eq. (49)

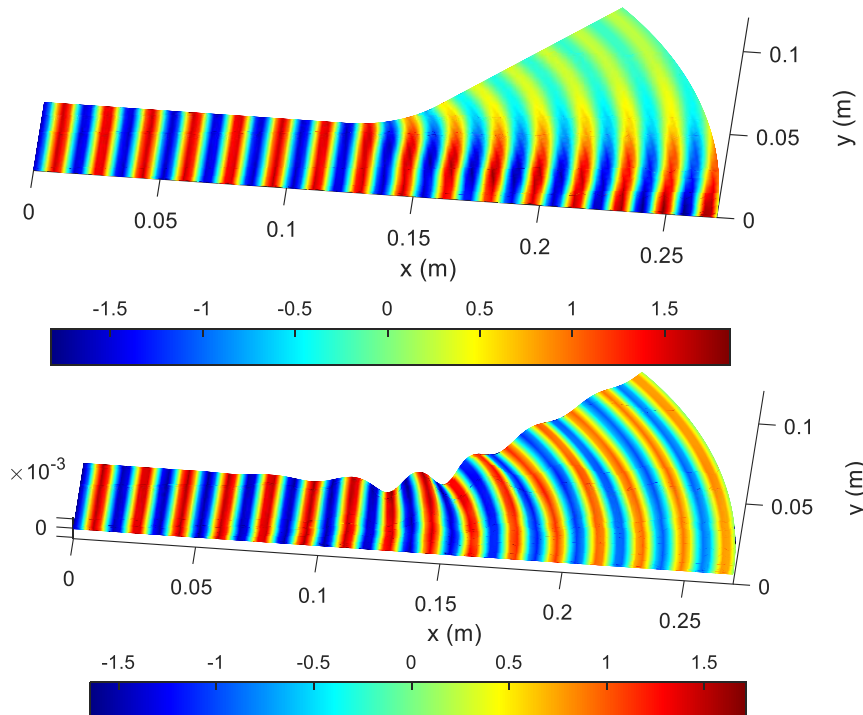
$$a_T(\xi_n) = w(\xi_n)t_b(\xi_n) \quad (53)$$

This results in a geometry which for the most part has a constant thickness, however when optimising for the felt area  $a_f$  there is a slight variation in  $t_c$  around the transition point between the channel and the wedge which is shown in Figure 86.  $t_c$  was calculated using Eq. (51).



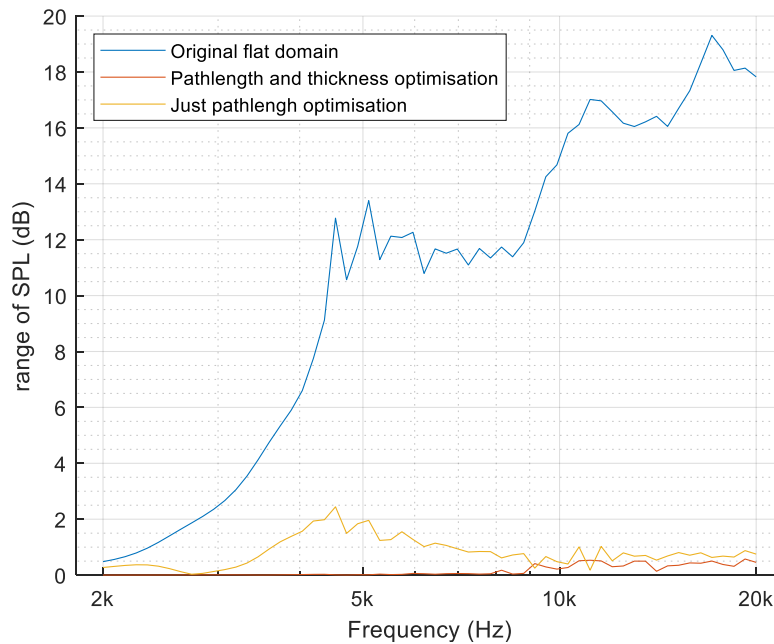
**Figure 86: Thickness correction  $t_c$  for channel wedge geometry**

Figure 87 shows the pressure response at 20Khz. The top model with no optimisation has notable beaming in the wedge section. In contrast, in the wedge section of the bottom plot, which has undergone both area and pathlength optimisation, there is neat cylindrical wave propagation which causes the intensity of the pressure to decrease steadily with distance. The pressure appears to be equally distributed across each wavefront.



**Figure 87: Pressure response at 20KHz for channel-wedge geometry ( $n_{mod} = 8, t_b = 1mm$ ), top: no optimisation, bottom: pathlength and area optimisation**

Figure 88 shows the range of SPL with and without optimisation for the channel wedge geometry ( $t_b = 1mm$  and 6 corrugations). Like with the simulations of the half sine, both models with pathlength optimization are a big improvement on the original flat domain, and the model with both pathlength and area optimisation has the best performance.



**Figure 88: Range of SPL (dB) for channel-wedge geometry with and without optimisation ( $n_{mod} = 8, t_b = 1mm$ )**

### 7.4.5 S-bend geometry

The S-bend geometry has tight curves which cause a large difference in pathlength between each edge. This meant that  $s_n$  reached as low as 0.65 in the 2D simulation, (Figure 20), indicating that the unoptimized geometry will be especially poor at supporting 1P propagation. This is confirmed in the pressure response shown on the left side of Figure 89 where the wavefronts are very unorganised. In contrast the design with pathlength and area optimisation shown on the right has much more aligned wavefronts throughout the shape.

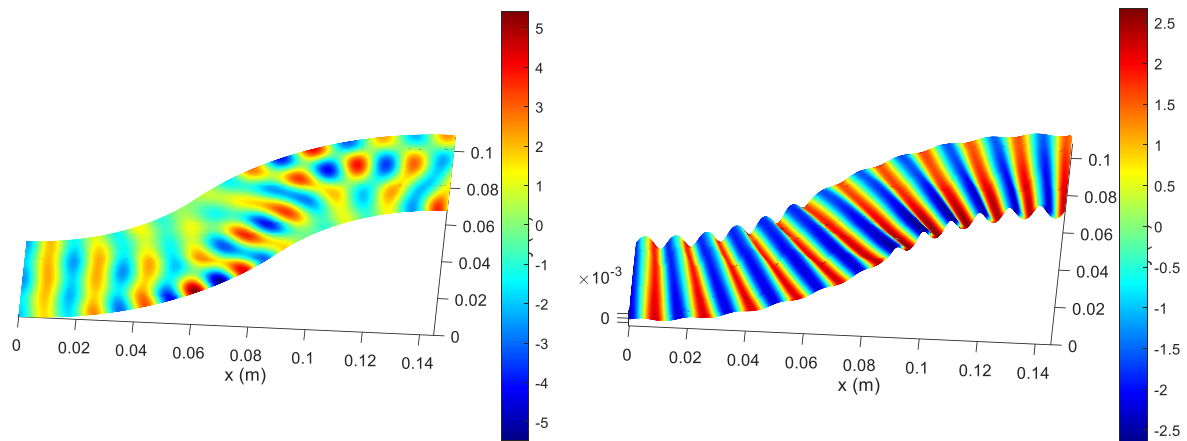


**Figure 89: Pressure response at 20Khz ( $n_{mod} = 12$ ,  $t_b = 1mm$ ,  $s_o = 0.01$ ), left: original flat geometry, right: optimised geometry**

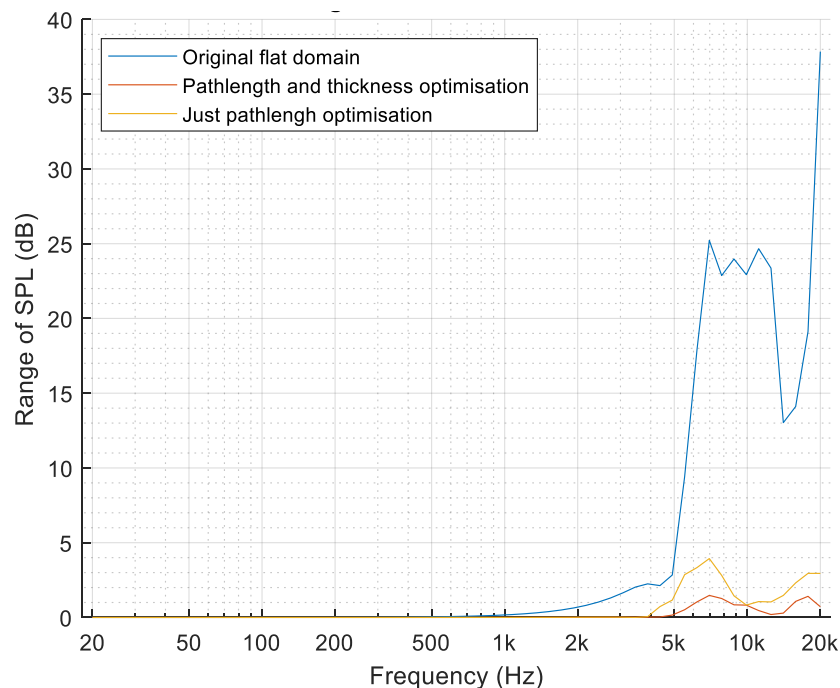


**Figure 90: Range of SPL for the s-bend geometry with and without corrugations ( $n_{mod} = 12$ ,  $t_b = 1mm$ )**

Figure 45 shows the range of the SPL across the mouth for the S-bend geometry for the original flat domain, a domain with pathlength optimisation, and a domain with both

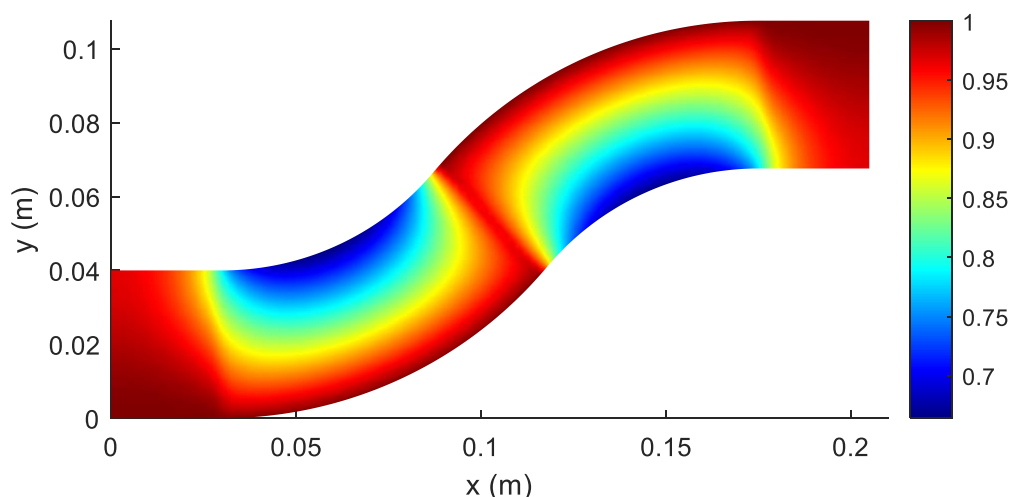
pathlength and thickness optimisation. The pathlength optimised geometry has a significant improvement at higher frequencies, and the model with the additional thickness optimisation performs even better. All the simulations work well at low frequencies because the wavelengths are much longer.

## 7.5 Adding extra channels on to either side of the S-bend – transitions

The S-bend geometry has constant curvature on each bend section right up to the edge of the domain. Therefore,  $s_n$  suggests that the pathlength should be compensated for right up to the edge of the geometry. This prompts the question of what happens to the metrics after the curved section if an additional channel is added and included in the metric calculation.

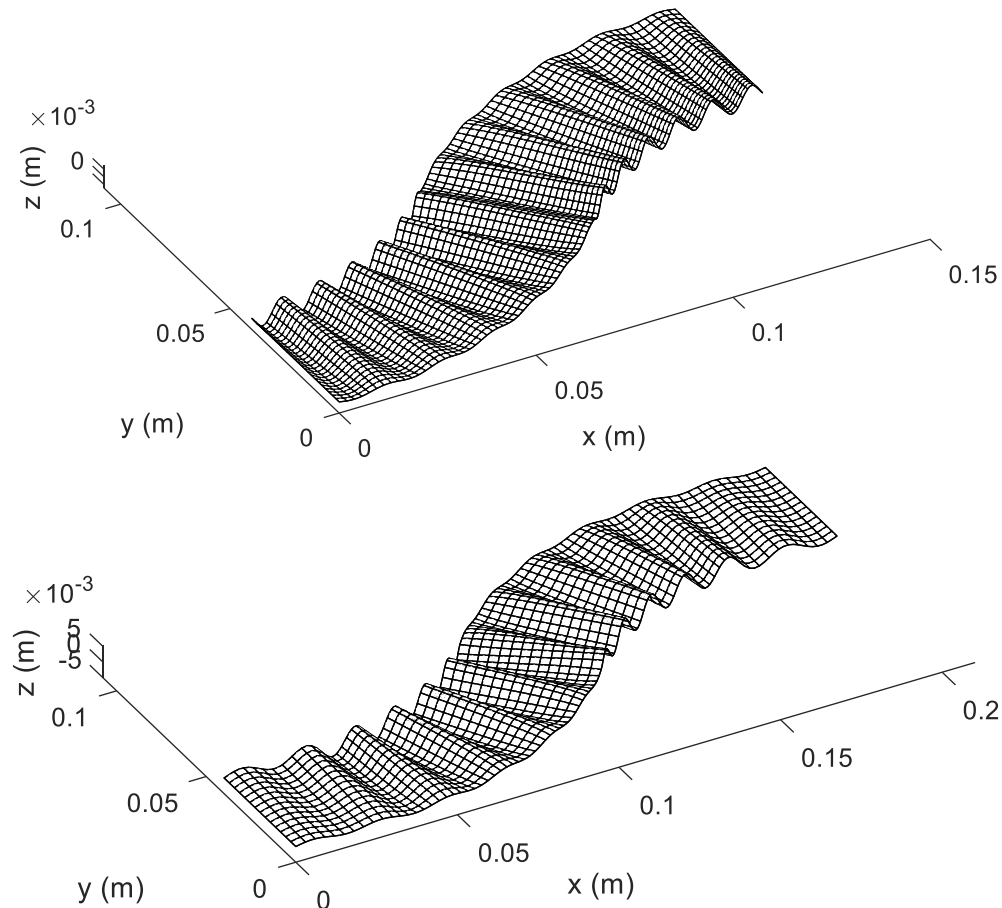
### 7.5.1 Effect of extra channel sections on stretch metric

Figure 91 shows  $s_n$  on the S-bend geometry with extra channels added to each end. Interestingly, the non-unity in  $s_n$  spreads out into the extra channel sections at each end, even though they have no pathlength error on their own.



**Figure 91:**  $s_n$  on the s-bend geometry with extra channels added to each end

Figure 92 shows the pathlength optimised s-bend mesh with no extra sections on the left and with 0.03(m) channels added on the right. In the model with the extra channels, the corrugations correcting the relative pathlength are not confined to the curved region and spread out into the additional sections.



**Figure 92: 3D pathlength optimised S-bend geometry ( $n_{mod} = 12$ ,  $t_b = 1mm$ ), top: no extra channel, bottom: 0.03 (m) extra channel**

In the model with the additional channels the corrugations also have a much lower amplitude (and therefore gradient) at the throat and mouth, which would make the design better for coupling to another device.

### 7.5.2 Effect of extra sections on area optimisation

It is also informative to look at the effect of adding extra channels on the area optimisation and its related metrics.  $f$  and  $a_f$  are plotted on the streamlines in Figure 94 and Figure 95 respectively. The layout of the streamlines is shown in Figure 93 with streamline 1 on the bottom boundary and streamline 7 on the top boundary, and is the same for the S-Bend model without extra sections.

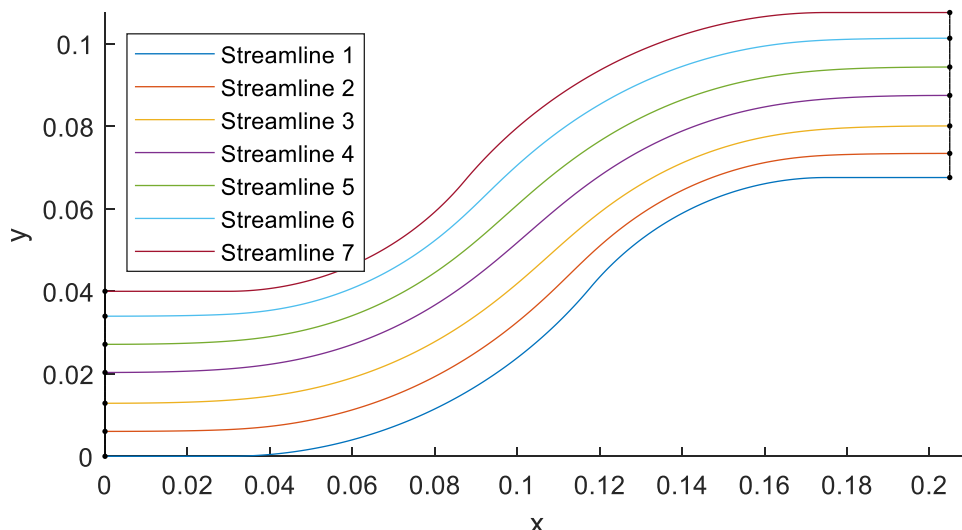


**Figure 93: 7 Streamlines traced through s-bend geometry with 30mm extra channels**

In the s-bend model with no extra sections there is a significant peak in  $f$  at the transition point between the two bends. This causes  $a_f$  to change in the second bend because  $a_f$  is calculated by integrating  $f$  down the streamlines (see Eq.(19)). Notably, it does not return towards unity.

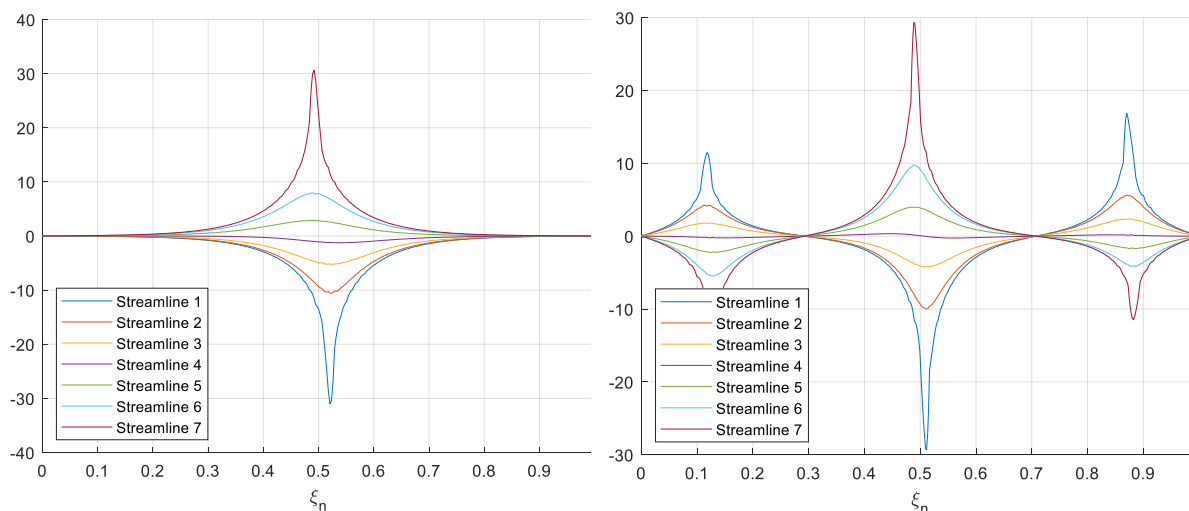


**Figure 94:  $f$  on 7 streamlines through s-bend geometry, left: no extra sections, right: 30mm extra sections**

In the model with extra sections there are additional spikes in  $f$  at the transition between the bends and the extra channel. This causes  $a_f$  to suggest the area is warped in one direction for the first bend and in the other for the second bend.

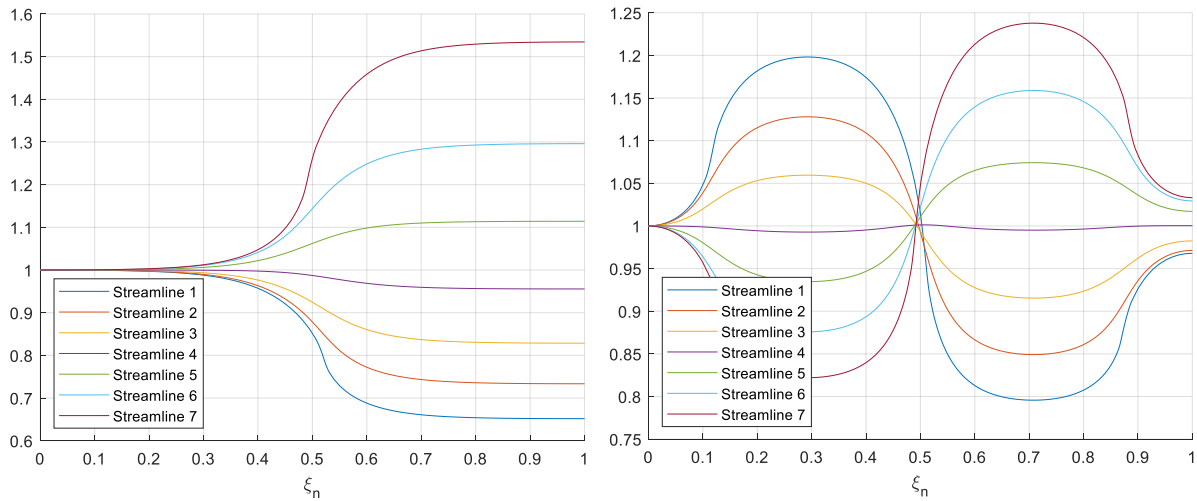


**Figure 95: Felt area  $a_f$  on streamlines through the s-bend geometry, left: no extra sections, right: 30mm extra sections**

When doing area optimisation on the 3D geometry, the model with no extra channels results in a domain which is significantly tapered in the second curved section up to the mouth. In contrast, the model with extra sections is tapered in one direction for the first bend section, tapered in the other direction for the second, and then comes back much closer to a constant thickness in the final additional section. A tapered mouth would be an inconvenience if the waveguide is design to be coupled to another device with a rectangular throat. Hence, including some space for the waveguide to realign to planar propagation appears desirable.

### 7.5.3 Effect of extra sections on the acoustic performance

The effect of adding extra channels to either side of the S-Bend on the acoustic performance was also investigated. The results with and without pathlength and area optimisation are plotted in Figure 96.

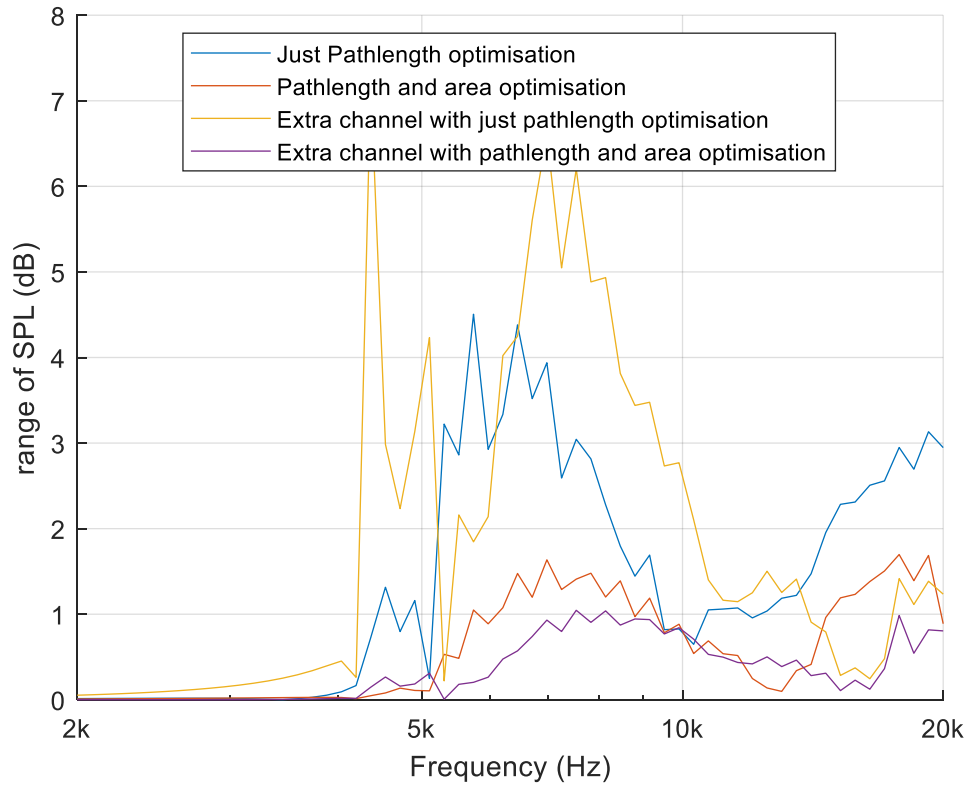


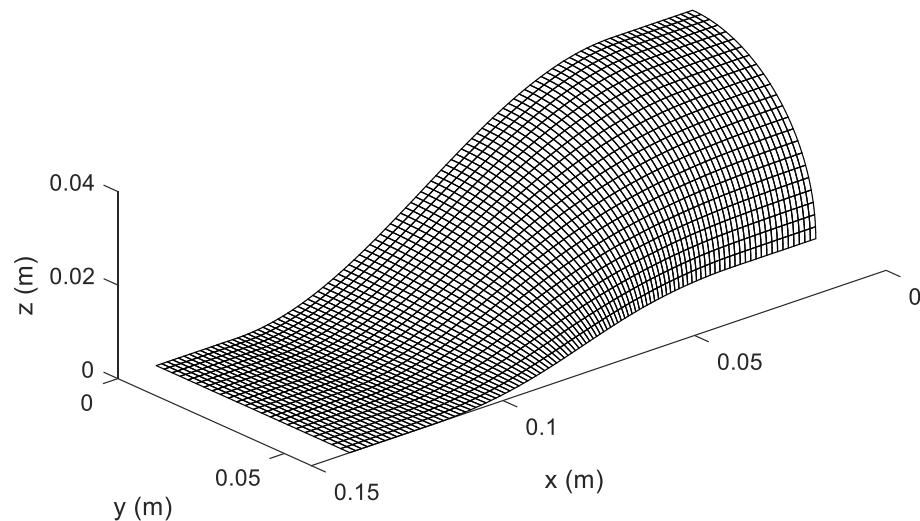
**Figure 96: Range of SPL across the mouth of s-bend geometry with and without 30mm extra channels and area optimisation ( $n_{mod} = 12$ ,  $t_b = 1mm$ ,  $s_o = 0.01$ ).**

The range in the SPL is lowest in the model with both the extra channels and the area optimisation. Interestingly on the simulations with just pathlength optimisation at some frequencies the performance is worse with the additional channels. This could be because the extra channels cause the corrugations to spread out and have larger wavelengths with a lower “stretch correction resolution” which less accurately corrects the sharp changes in  $s_n$ .

## 7.6 Circle to square converter

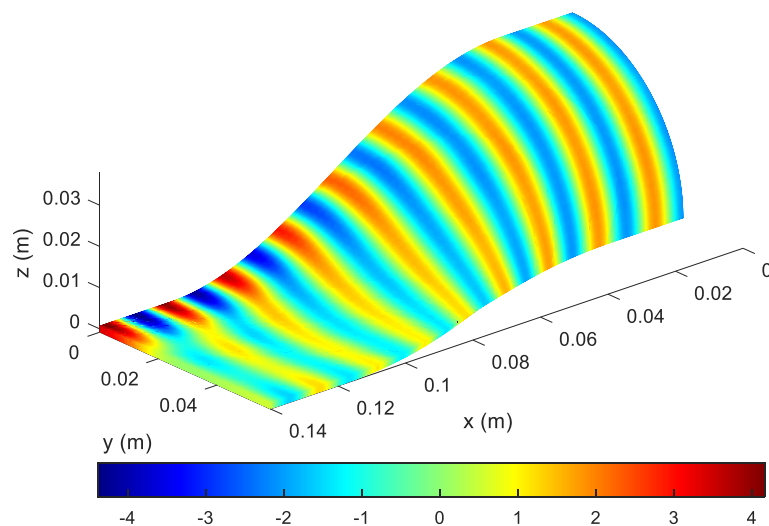
The transition between the circular or annular exit of a compression driver to a rectangular horn throat is a complex problem with significant application in the professional audio industry. This makes it an interesting final test case for the design techniques outlined in this dissertation.

Figure 97 shows a prototype 2D shell mesh which performs this transition. Because the device is symmetrical in two planes, only a quarter of it was simulated to save computational expense, this means that the model excludes any possible higher order asymmetric modes. In this design the exit is at  $x = 0.14$ , and the entrance which would be tapered down in a cone shape and connected to a compression driver is at  $x = 0$ .



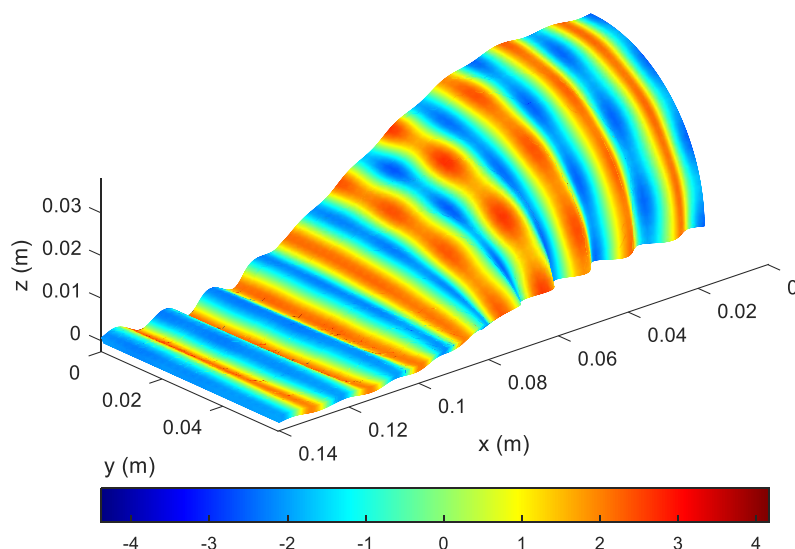
**Figure 97: Prototype mesh for circle to square adapter**

To avoid a sharp corner at the entrance and exit a cosine transition was used to blend from the circular entrance to the line shaped exit. Extra channels were also added to each end to allow the optimisation to spread out and avoid having large corrugations which are too close to the ends of the geometry as this would make the device hard to couple to a horn or compression driver.



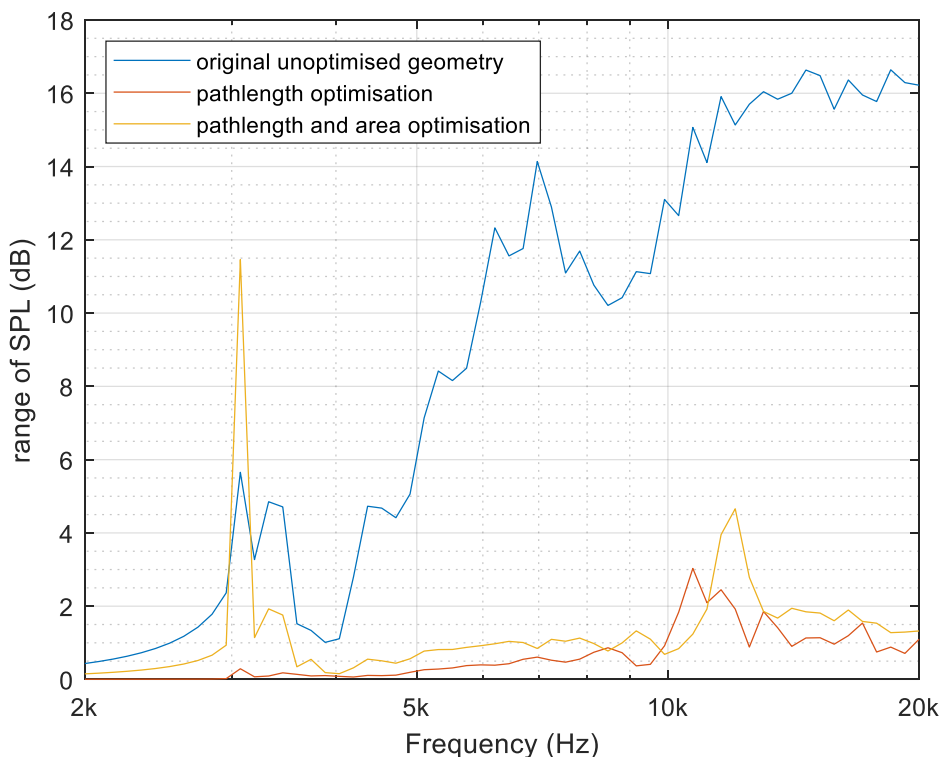
**Figure 98: Pressure response of circle to square adapter at 20KHz with no optimisation ( $t_b = 1.5\text{mm}$ )**

Figure 98 shows the pressure response at 20KHz with no optimisation. There is a notably intense region at  $y = 0$  on the mouth ( $x = 0.14$ ). The wavefronts are also visibly warped due to the differences in the relative pathlength through the shape.



**Figure 99: Pressure response of circle to square adapter at 20KHz with pathlength and area optimisation ( $t_b = 1.5mm$ )**

Figure 99 shows a plot of the pressure at 20KHz on the optimised model. The pressure distribution is much more equal across the wavefronts, and they appear to be more in-line with the mouth. There is some slight modal behaviour visible around  $x = 0.06$ .



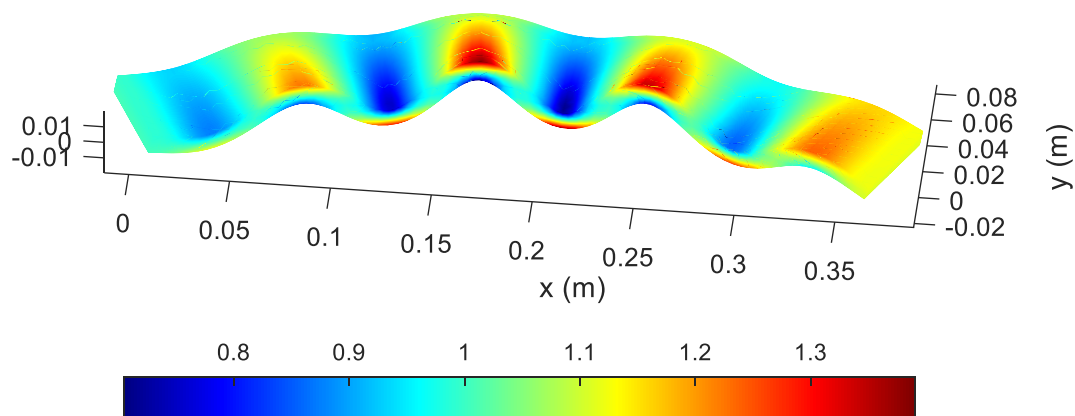
**Figure 100: Range of SPL for the circle to square adapter with and without optimisation ( $t_b = 1.5mm$ )**

Figure 100 is the range of SPL across the mouth with and without different optimisation applied. The best result is in the model with the area and pathlength optimisation which has a

maximum range of SPL of 3dB around 11kHz. Although 3dB is a significant variation in the SPL, the optimised model is still a big improvement on the original flat domain.

## 7.7 Re-analysing a 3D modulated domain

This section investigates re-analysing the thickened 3D domains with the waveguide metrics. Figure 101 is  $s_a$  on the 3D pathlength optimised half sine geometry. Because of the thickness in the domain, there is a difference in the relative pathlength along the top and bottom boundary surfaces. This causes a banding in  $s_a$  which is most pronounced at the peaks and troughs of the corrugations where the curvature of the sine wave corrugation shape is at a maximum.



**Figure 101:**  $s_a$  on 3D optimised half sine geometry

This localised banding is also seen in  $a_f$  in Figure 102 which has similar characteristics to Figure 101.

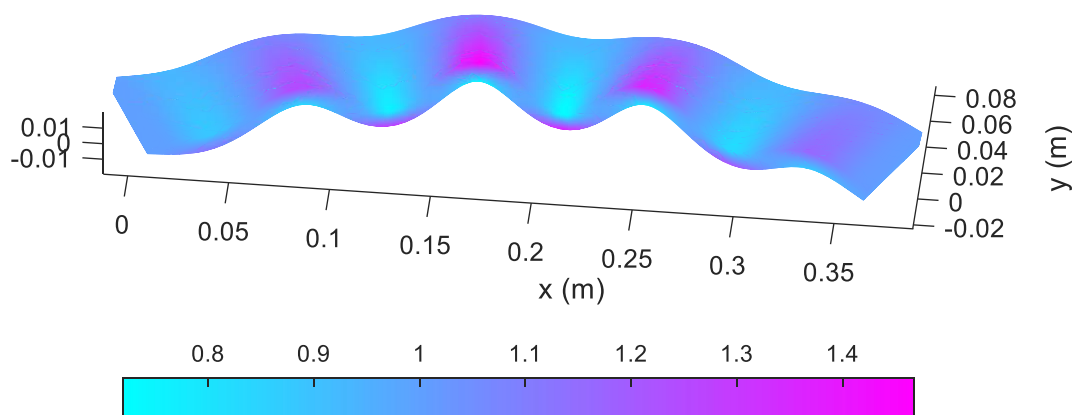


**Figure 102:**  $a_f$  on 3D optimised half sine geometry

Although the acoustic performance of the optimised 3D half sine was shown to significantly improve in section 7.4.1, both Figure 101 and Figure 102 show how using corrugations to equalise the relative pathlength introduces its own localised error within each corrugation. This

localised error is an indication of why the acoustic simulations of the optimised geometry show that the design does not support 1P wave propagation perfectly.

### 7.7.1 Metric banding

To further understand this banding effect simulations of the waveguide metrics were performed on a single corrugation shape in 2D. Figure 103 shows this metric banding on a 2D sine wave shape which is the same as a cross sectional slice through a single 3D sinusoidal corrugation. It illustrates how the corrugation shape causes banding in the metrics. Both  $s_a$  and  $a_f$  show most error around the peaks and troughs of the sinusoidal shape when the curvature is at a maximum and show close to no error in the straighter sections.

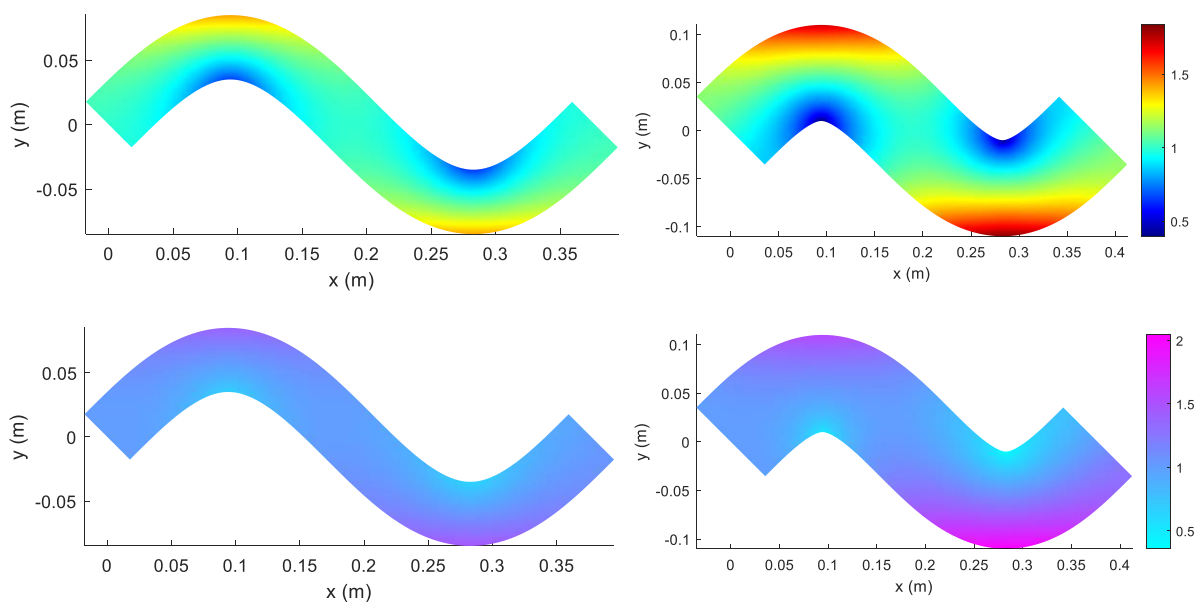


**Figure 103: Metric banding on a single corrugation of different thickness, top:  $s_a$ , bottom:  $a_f$ , left:  $t = 50mm$ , right:  $t = 100mm$**

The thinner model on the left side of Figure 103 has significantly less error in relative pathlength and area shown by  $s_a$  and  $f_a$ . This ties in with the acoustic simulations of a single corrugation in section 7.2.1, which showed a thicker domain to have significantly more error in the SPL between the entrance and exit.

If trying to further optimise a modulated 3D model by iteratively reducing error in  $s_a$  and  $a_f$ , the localised banding introduced by the pathlength optimisation (corrugation shapes) could be a problem as it might cause the algorithm to try and remove the pathlength optimisation from the first iteration. One option to avoid this could be to average through the domain to try to ignore the error in the metrics due to the thickness and concentrate only on error which is parallel to the surface of the shell geometry.

## 7.8 Conclusions

This chapter considered 3D geometries which allowed for the cross-sectional area of the domain to be controlled and simulations of the Helmholtz wave equation to be performed. Through studying a distorted rectangular cuboid, the felt area metric  $a_f$  is shown to be capable of iteratively reducing changes in cross sectional area through a geometry.

When forcing an acoustic pressure wave through a corrugation shape, the magnitude of interference to the wave propagation is closely related to the shape of the corrugation. To get less interference the acoustic channel must be thinner and have less curvature, which can be achieved through corrugations which are longer and have less amplitude. Thickened triangular shaped corrugations perform worse acoustically due to the sharper corners in the acoustic channel found at the peaks and troughs.

In every test case which was studied the thickened 3D geometry with sinusoidal shaped corrugations used to equalise the relative pathlength has significantly less disruption to the acoustic wavefront at the exit when compared to a model without any pathlength optimisation. Additional correction to the thickness using  $a_f$  further reduces variations in the pressure level on the exit surface.

When re-analysing a thickened 3D corrugated domain with the waveguide metrics, the corrugations cause a strong periodic banding through the thickness of the domain, which is intensified if the domain is thicker.

## 8. Discussion, conclusions and future work

This chapter discusses and makes conclusions about different aspects of the research project. This begins with the waveguide metrics and their capability for guiding automatic waveguide optimisation. It then explores the performance limitations of the optimised waveguides, the best corrugation shapes, and the design parameter balancing procedure required for the best performance. The approximations to the simulations are considered and finally future work is suggested.

### 8.1 Waveguide metrics

The research in this project is based on the hypothesis that the waveguide metrics, stretch and flare, proposed by Ocle-Brown are effective measures of the spatial capability of a waveguide to support 1P wave propagation. Figure 53 shows the modulated shell mesh of the half sine to have significantly less pathlength error indicated by  $s_a$  than the original flat geometry. This then ties in with the acoustic simulations of the pathlength optimised half sine in which the pressure wavefronts are much more aligned and there is significantly less range of SPL over the mouth (Figure 78 and Figure 79 respectively), indicating the geometry is better at supporting 1P wave propagation. The same relationship was seen with all the different test geometries. Hence, this hypothesis appears to hold for the test cases simulated.

Metric based optimisation the optimised geometry was notably better at supporting 1P wave propagation than the original geometry. This was marked by a smaller range in SPL across the mouth on the optimised design

On every example which was optimised in this dissertation, In most cases, the models which had both pathlength and area optimisation performed better than the models with pathlength optimisation only.

These findings suggest that the waveguide metrics and corrugation based pathlength compensation techniques investigated are useful tools for the design and development of acoustic waveguides and lenses. However, although the performance of the waveguide has significantly improved, it is still far from perfect as there are some limitations to the corrugation pathlength compensation method investigated in this project.

## 8.2 Performance limitations

The fundamental limitation to the performance of the waveguides is related to the findings by Putland (1993) in which he describes mathematically how there are only three coordinate systems which will support perfect single parameter waves. This is important as the prototype geometric surfaces studied in this project are not of these shapes, so will never support 1P wave propagation perfectly for all frequencies no matter how well the optimisation works. (except for the scenario where the optimisation procedure creates one of Putland's isolated cases). However, through reducing the error in the waveguide metrics proposed by Oclew-Brown, the designs become more capable of supporting 1P wave propagation over a limited bandwidth.

There are limitations to the corrugation based pathlength correction technique too. This is explored in the simulations in section 7.2 which found there is a detrimental effect from forcing the sound waves through a thickened corrugation. The effect was worst when the corrugation shape meant the acoustic channel had higher curvature or that the domain was wider. These problems were also visualised when re-analysing the 3D geometry, as intense periodic banding in the waveguide metrics through the thickness which was strongly affected by the thickness of the domain.

Using corrugations to correct the pathlength through a waveguide can lower the average error in the waveguide metrics over a 2D shell mesh. However localised pathlength error is then introduced within each corrugation when the domain is thickened into 3D.

## 8.3 Corrugation shapes

When working with a 2D shell mesh, sinusoidal shape corrugations are less prone to metric calculation errors than triangular shape corrugations as there is a less sudden change in the gradient found at the peaks and troughs. It may be possible to perform a different type of mesh gradient calculation which would work better with the sharp changes in gradient seen in triangle shaped corrugations. This was not investigated in this project. Figure 73 shows that a sinewave is a better corrugation shape to use acoustically as the simulations of a corrugation shape with added triangular Fourier harmonics resulted in significantly more error in the SPL transmitted through the domain, most probably due to the increase in curvature seen at the top of the corrugation.

Figure 68 and Figure 71 illustrate that a thinner corrugated domain works better. Both test cases also suggest that a smaller amplitude in relation to the corrugation period is preferred. Overall, the studies suggest that a sinusoid is the best shape to use to add pathlength with

minimal disruption to the acoustic propagation. There are however other possible shapes which were not studied in this project.

## 8.4 Design parameters trade off – The balancing act

In most design problems the stretch metric  $s_n$  is fixed, but the number of corrugations  $n_{mod}$ , and in some situations the thickness of the domain, can be adjusted. Getting the best acoustic performance is achieved by carefully balancing these design parameters.

The amplitude of the corrugations is a function of  $s_n$  and  $n_{mod}$ . In section 56 it was found that using fewer larger corrugations results in less accurate pathlength compensation than using an increased number of smaller corrugations. In contrast, the simulations of a thickened corrugation in section 79 showed that smaller corrugations, with higher curvature, will perform worse acoustically especially when a thicker domain is used.

This means that  $n_{mod}$ , and  $t_b$  are critical to reaching the optimal performance. The ‘sweet spot’ depends on the shape of the domain to be optimised and the required thickness or area expansion through the geometry.

Because the viscosity of the air was not modelled, all the simulations in this project suggested a thinner domain works better. When creating physical waveguides having a domain which is too thin might cause problems because of viscosity, engineering tolerances, and meeting the required area expansion through the device.

The three design requirements which must be balanced to achieve the best performance are therefore to create:

- A domain with pathlength equalising corrugations which are short enough to correct small changes in  $s_n$  without too much error from the ‘corrugation resolution’
- A domain with pathlength equalising corrugations which are large enough that they don’t cause sharp corners in the acoustic path and are thin enough that they have good acoustic transmissibility
- A thick enough domain so that the waveguide, has realistic manufacturing tolerances, does not have problems with viscosity, and has the correct cross-sectional area to couple to another device

The optimal parameter values will vary depending on numerous factors such as: waveguide shape; size; intended frequency bandwidth; required cross-sectional area through the device.

## 8.5 Acoustic FEA accuracy and approximations

The acoustic analysis in this project was done using FEA simulations of the Helmholtz equation. The simulations did not include viscous losses or nonlinearities, which could affect performance for real manufactured waveguides. The most significant effect from the viscous losses would occur at high sound pressure levels.

Another approximation in the acoustic simulations was the  $\rho_0 c$  boundary condition used as a termination at the mouth of the waveguides. A physical acoustic lens or waveguide is usually connected to the air, or to another device such as a horn flare. The acoustic impedance at the exit is therefore unlikely to be exactly  $\rho_0 c$ , except in the isolated case the device is connected to a plane wave tube.

When using a  $\rho_0 c$  termination, if the wavefront isn't perfectly normal to the boundary some of the energy will be reflected. Only wavefronts which are perfectly planar in relationship to the boundary will be completely absorbed. This means the disruptive effect from any non 1P wave propagation will be exaggerated, so the models simulated may have slightly better acoustic properties if a more accurate boundary condition was used.

One option for a more accurate boundary condition would be to use a perfectly matched layer (PML), which could be designed to give the correct acoustic load onto the mouth of the waveguide and absorb any outward propagating sound waves.

Another option would be to couple the FEA simulations to a Boundary Element Method (BEM) simulation of the acoustic radiation. BEM simulations are much more suited to simulating external radiating situations as only the boundaries are modelled. Again, care would have to be taken to make sure the correct acoustic load is applied to the mouth of the waveguide.

## 8.6 Lumped parameter acoustic modelling

A lumped parameter model will not measure if a waveguide is good at supporting a 1P propagation. However, an optimised waveguide which is good at supporting 1P wave propagation can be modelled unusually accurately with a 1D lumped parameter model. 1D approximations of the wave equation are a convenient horn design technique and are great for creating useful analytical relationships. Hence, deriving them for optimised waveguides could enable efficient driver optimisation.

## 8.7 Future work

### 8.7.1 Building samples to validate simulations

The best way to validate the simulations and highlight causes of error in the models would be to manufacture physical samples of the different models and measure them. Due to the intricacy of the optimised geometry, 3D printing or CNC cutting would be the best method of manufacturing engineering samples.

Measuring 3D physical samples could be a challenging task for several reasons. For the waveguides to work as intended, the correct acoustic load would need to be applied to the mouth of the device, which, depending on the load, could require building a physical horn or a large, customised plane wave tube to which the waveguide device would couple.

Another difficulty with measurements is that many of the designs have thin channels which means that the microphone or sensor might not fit inside of the device, and even if the microphone was to fit inside, its physical presence would probably have a detrimental effect on the wave propagation inside of the channel. For this reason, it would probably be most practical to measure the shape or pressure distribution of a wavefront radiated from the device rather than an internal wavefront. FEA models could be tuned to give matching radiated pressure, after which their internal predictions would be more trustworthy too.

### 8.7.2 Explore optimising different designs

While the test case geometries studied in this project were useful designs for investigating the metrics and optimisation techniques, the methods explored could be used to create waveguides or acoustic lenses for many different situations. It would be interesting to try to optimise some more complex designs and try and tackle some more complex real-world acoustic wavefront manipulation problems like the circle to square adapter in section 7.6. By doing this more understanding of the limitations of the design method would be gained.

### 8.7.3 Iterative geometry optimisation

It would be interesting to use the waveguide metrics to iteratively optimise a design. For this project only a single iteration of improvement was explored, except for in section 7.1 which studied the iterative area optimisation of a distorted cuboid.

Continuous iterative optimisation would involve re-analysing a modulated model and using the metrics to further modify it, creating a new geometry on each iteration with the aim of further improving its capability of supporting 1P wave propagation.

One problem with this is that the initial area optimisation involves extruding the shell mesh into a 3D mesh, which, as seen in section 7.7, causes banding in the metrics through the

corrugation shapes because of the domain thickness. This additional banding in the waveguide metrics could potentially cause problems, as correcting for it completely would require taking away the corrugations which were added in the first iteration. A potential work around for this could be to average the metrics through the cross-section of the 3D mesh back on to the shell mesh, so that the error from the thickness is ignored.

Another option would be to only optimise for error in the relative pathlength shown by  $s_n$  and keep the geometry as a shell mesh on each iteration. This could continue perhaps until the error in  $s_n$  stops reducing and then a final iteration could be done in which the shell mesh could be extruded into a 3D geometry with area optimisation controlled by  $a_f$ .

#### **8.7.4 Modelling Viscous losses**

The simulations performed in this project did not include the effect of thermo-viscous losses. It would be good to investigate how much these losses effect the performance of the modulated waveguides. A simple prediction would be to consider the thickness of the waveguide and use an analytical model to approximate the viscous losses such as the equations given by Kozlov and Fedorov (2005).

The bends in the corrugated sound propagation path may also influence the viscous losses. A more accurate prediction might be to investigate the losses inside a single corrugation whilst changing the geometric parameters and then use these results to predict the losses in a domain with many corrugations. The most accurate method of modelling the viscous losses would be to use a thermoviscous acoustic FEA simulation and model the entire waveguide. However, this technique is much more computationally expensive and would not result in useful analytical relationships.

## 9. References

- Heil, C., (1992) *Sound wave guide*, (U.S. Patent No 5163167A) U.S. Patent and Trademark Office. <https://patents.google.com/patent/US5163167A/en>
- Spillmann, J., & Riemersma, S. (2017) *Acoustic Waveguide* (U.S. Patent No 5163167A) U.S. Patent and Trademark Office. <https://patents.google.com/patent/US5163167A/en>
- Magalotti, R., (2009) *Acoustic waveguide and electroacoustic system comprising said waveguide* (European Patent No 1927978B1) European Patent Office. <https://patents.google.com/patent/EP1927978B1/en?q=acoustic+waveguide&oq=acoustic+waveguide>
- Dodd, M. A., & Oclew-Brown. A. J. (2021), *Acoustic Waveguides* (EP3806086A1). European Patent Office.
- Dodd, M. A., & Oclew-Brown. A. J. (2022), Wave-shaping using novel single-parameter waveguides. *Audio Engineering Society Convention*, no. 153.
- Gustavo Silva., Rodolphe Le Riche., Jérôme Molimard., & Alain Vautrin. (2007). Exact and efficient interpolation using finite elements shape functions. *HAL* <https://hal.archives-ouvertes.fr/hal-00122640v2>
- Putland, G. R. (1993). Every One-Parameter Acoustic Field Obeys Webster's Horn Equation. *J. Audio Engineering Society*, Vol. 41, No. 6.
- Zienkiewicz, O. C., Taylor, R. L., Zhu, J. Z., & Zienkiewicz, O. C. (2013). *The finite element method : Its basis and fundamentals*. Jordan Hill, Oxford: Elsevier Science & Technology.
- Yang, Y., Jia, H., Lu, W., Sun, Z., Yang, J. (2017). Impedance-matching acoustic bend composed of perforated plates and side pipes. *Journal of Applied Physics* 122, 054502. doi: <https://doi.org/10.1063/1.4996848>
- Kolbrek, B., & Dunker, T. (2019). *High-Quality Horn Loudspeaker Systems*. Croydon, UK: Kolbrek Elektroakustikk
- Kock, E. W., & Harvey, F. K. (1949) Refracting Sound Waves. *The journal of the Acoustical Society of America* Vol.21 No. 5
- Memoli, G., Chisari, L., Eccles, J., Caleap, M., Dinkwater, B., & Subramanian, S. (2019) VARI-SOUND: A Varifocal Lens for Sound. *CHI Conference on Human Factors in Computing Systems Proceedings (CHI 2019)*, May 4–9, 2019, Glasgow, Scotland Uk. ACM, New York, NY, USA, 14 pages. <https://doi.org/10.1145/3290605.3300713>
- PACSYS Ltd., (2008). *PAFEC FE*. PACSYS Ltd.,
- Kinsler, L., & Frey, A. (2000). *Fundamentals of Acoustics* (4th Ed.). Danvers, USA: John Wiley & Sons.
- Shaw, E. A. G., (1971). Acoustic Horns with Spatially Varying Density or Elasticity. *The Journal of the Acoustical Society of America* Vol.50 No.3 830-840

- Webster, A. G. (1920). Acoustical Impedance and the Theory of Horns and the phonograph, *Proc. Natl. Acad. Sci. USA*, 5, pp. 275–282; reprinted in *J. Audio Engineering Soc.*, 25 (1977), pp. 24–28
- JBL (1954), *Professional series acoustic lens family*, Available at: [https://jblpro.com/en/site\\_elements/2301-2390-2391-2392-2395-information](https://jblpro.com/en/site_elements/2301-2390-2391-2392-2395-information) (Accessed: 08/02/2022).
- Dickie, L. (2009). Horn loading arrangement for a co-axial two-way loudspeaker (United Kingdom Intellectual Property Office Patent) [Review of Horn loading arrangement for a co-axial two-way loudspeaker]. <https://patentimages.storage.googleapis.com/53/e9/11/934d5df268808d/GB2458275A.pdf>
- Felix, S., & Pagneux, V. (2001). Sound propagation in rigid bends: A multimodal approach. *Acoustical Society of America*, 110 (3), Pt. 1. doi: 10.1121/1.1391249
- Geddes, E. (1989). Acoustic Waveguide Theory. *Journal of the Audio Engineering Society*. Vol. 37, No 7/8 p554.
- Geddes, E. (1993). Acoustic Waveguide Theory Revisited. *Journal of the Audio Engineering Society*. Vol. 41, No 6. p452.
- Kreyszig, E (1991). *Differential Geometry*. New York: Dover.
- Kozlov, V. F., & Fedorov, A. V., Acoustic properties of rarefied gases inside pores of simple geometries. *Journal of the Audio Engineering Society*. Vol. 117, No. 6 p760-774.

# **Appendix A: A method for numerically testing if an acoustical waveguide admits one-parameter waves**

This appendix is a copy of the paper by Dr Jack Ocleo-Brown with which much of the work in this dissertation is based on. It has been replicated here with his permission.

# A method for numerically testing if an acoustical waveguide admits one-parameter waves.

## 1 Introduction

Putland [1] shows that in the Helmholtz equation has one-parameter solutions (1-P) for a particular coordinate,  $u$ , only if  $|\nabla u|$  and  $\nabla^2 u$  are functions of  $u$  alone.

Putland expresses these condition as

$$\nabla u = M(u) \mathbf{e}_u \quad \text{Condition A1.}$$

$$\nabla^2 u = N(u) \quad \text{Condition B1.}$$

where  $M$  and  $N$  are real functions and  $\mathbf{e}_u$  is a unit vector in the direction of  $\nabla u$ .

Putland further demonstrates that  $u$  may be transformed into another coordinate  $\xi(u)$  that measures the arc length along an orthogonal trajectory of surfaces of constant  $u$ .

$$\xi(u) = \int \frac{du}{M(u)} \quad 1.1.$$

Condition A1 may be equivalently expressed in terms of  $\xi$  as

$$|\nabla \xi| = 1 \quad \text{A2.}$$

and condition B1 as

$$\nabla^2 \xi = L(\xi) \quad \text{B2.}$$

where  $L$  depends on  $\xi$  alone.

In the final sections of Putland's work he demonstrates that there are emphatically only three 1-P waveshapes (planar, cylindrical and spherical) concluding that "The design of practical constant-directivity horns cannot be advanced by finding a new geometry for an exact 1P waveguide, because all possible 1P waveshapes are already known.". The purpose of this method is for the development of waveguide geometries that approximately meet conditions A1 and B1 thereby allowing close to 1-P wave propagation over a limited low-frequency bandwidth.

## 2 Geometrical interpretation of Putland's conditions

Putland himself offers some useful discussion of the geometric implications of his conditions. It's useful to repeat these and also add some additional points. In order to do this we will use Putlands terminology

$\xi$ surface	Surface of constant $\xi$
$\xi$ trajectory	Orthogonal trajectory to the $\xi$ surfaces
$\xi$ tube	Tube of $\xi$ trajectories, that is, the locus of all the $\xi$ trajectories intersecting a simple closed curve contained in a $\xi$ surface.

## 2.1 Interpretation of condition A

The interpretation of condition A is straight-forward. All  $\xi$  trajectories between any two  $\xi$  surfaces have the same length. In terms of the acoustical pressure  $p(\xi)$  one might think of this as the propagation distance between consecutive wavefronts being strictly the same over the entire wavefront surface.

## 2.2 Interpretation of condition B

An alternative expression for A2, also given by Putland, is that the divergence of  $\xi$  is equal to the unit vector tangent to the  $\xi$  trajectories,  $\mathbf{e}_\xi$

$$\nabla \xi = \mathbf{e}_\xi \quad 2.1.$$

Expression B2 can be re-written in terms of these unit vectors as

$$\nabla^2 \xi = \nabla \cdot \mathbf{e}_\xi = L(\xi) \quad 2.2.$$

Note that the unit vectors,  $\mathbf{e}_\xi$ , are also the unit normal vectors of the  $\xi$  surfaces. The mean curvature of a surface in 3D space is related to the divergence of it's surface normals,  $\mathbf{n}$ , by the expression

$$2H = -\nabla \cdot \mathbf{n} \quad 2.3.$$

This allows us to write

$$H_\xi = \frac{-L(\xi)}{2} \quad 2.4.$$

where  $H_\xi$  is the mean curvature of the  $\xi$  surfaces. Therefore we see that the physical interpretation of B2 is that the mean curvature is constant over any surface of constant  $\xi$ . In terms of the acoustical pressure, that the mean curvature is constant over the surface of any given wavefront.

## 2.3 Alternative interpretation of condition B

Putland uses A2 applied in a  $\xi$  tube to derive Webster's substitution for the Laplacian operator

$$\nabla^2 p = \frac{d^2 p}{d\xi^2} + \frac{1}{S} \frac{dS}{d\xi} \frac{dp}{d\xi} \quad 2.5.$$

Using this substitution directly in B1 results in

$$N(u) = \frac{d^2 u}{d\xi^2} + \frac{1}{S} \frac{dS}{d\xi} \frac{du}{d\xi} \quad 2.6.$$

where  $\frac{1}{S} \frac{dS}{d\xi}$  is commonly called the flare-rate, by convention given the notation  $m$ . The flare rate is a useful parameter for an acoustician as it is directly related to the cut-off frequency of a waveguide,  $f_c = \frac{mc}{4\pi}$ , which is the frequency above which the pressure due to wave propagation is larger than the hydrostatic pressure.

Expression 2.6 indicates that an alternative interpretation of condition B is that for 1P behaviour the flare rate must be constant over any surface of constant  $\xi$ .

### 3 Analysis method overview

The basis of the method presented here is to use a numerical solution to Laplace’s equation to find a suitable  $u$  coordinate within the waveguide. From  $u$  two metrics are calculated that measure the local geometric deviation from Putland’s two conditions for 1-P propagation.

#### 3.1 Laplace analysis arrangement

To determine the coordinate  $u$  we apply Laplace’s equation to the interior of the waveguide

$$\nabla^2 u = 0 \tag{3.1}$$

with the following boundary conditions

$$u(\mathbf{x}) = 0 \Big|_{\mathbf{x}=S_{throat}} \tag{3.2}$$

$$u(\mathbf{x}) = 1 \Big|_{\mathbf{x}=S_{mouth}} \tag{3.3}$$

$$\nabla u(\mathbf{x}) \cdot \mathbf{n} = 0 \Big|_{\mathbf{x}=S_{wall}} \tag{3.4}$$

where  $S_{throat}$  is the entrance surface, or throat, of the waveguide, into which homogenous acoustical waves will be directed during use.  $S_{mouth}$  is the exit surface, or mouth, of the waveguide from which homogenous acoustical waves will be emitted during use.  $S_{wall}$  is the rigid surface forming the boundaries of the waveguide.

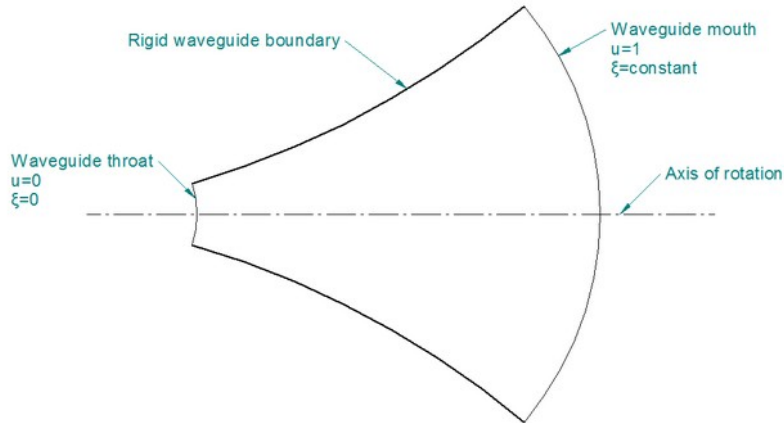


Figure 1. Schematic illustration of an example waveguide

Figure 1 shows an example of a flared axisymmetric waveguide with throat surface, mouth surface and rigid boundary surfaces labelled. The boundary conditions force the calculate coordinate  $u$  to be zero on the throat surface and increase monotonically to  $u=1$  at the mouth surface. As a result of the boundary condition at the rigid walls, surfaces of constant  $u$  are perpendicular to the rigid boundary wall.

Every coordinate system for which the Helmholtz equation is separable is necessarily also a separable coordinate system for Laplace’s equation. Therefore if we calculate  $u$  using this approach and then subsequently find that  $u$  satisfies Putland’s conditions A and B, we can guarantee that the waveguide is a 1-P solution to the Helmholtz equation along the coordinate  $u$ .

## 3.2 Metrics

### 3.2.1 Metric A: “stretch”

To measure the deviation from Putland’s condition A we simply compute the magnitude  $|\nabla \xi|$ . According to A2,  $|\nabla \xi|$  must be unity in the entire waveguide. If  $|\nabla \xi|$  is less than unity in some regions of the waveguide, this indicates that the  $\xi$  surfaces are too close to one another. Greater than unity indicates that the  $\xi$  surfaces are too far apart.

$$\text{metric A} = |\nabla \xi| \quad 3.5.$$

To find a mapping between  $u$  and  $\xi$  we simply compute the line integral along any  $\xi$  tube,

$$\xi(u) = \int \frac{du}{|\nabla u|}. \quad 3.6.$$

In general this mapping is not unique and depends on the choice of  $\xi$  tube. In fact the only situation where the mapping is unique for every  $\xi$  tube is when condition A is met. However, whichever mapping for  $\xi$  is chosen, the value of metric A on any  $\xi$  surface is linearly scaled to be unity at the intersection of the  $\xi$  surface with the selected  $\xi$  tube.

**JACK: normalisation is still an outstanding issue with this metric as we can only easily add extra distance to the waveguide by adding modulations.**

### 3.2.2 Metric B: “flare”

To compute the flare from the numerically calculated  $u$  we assume that within each  $\xi$  tube we can apply Webster’s Laplace approximation (equation 2.6) and the Laplace solution is of the form

$$\frac{d^2 u}{d\xi^2} + \frac{1}{S} \frac{dS}{d\xi} \frac{du}{d\xi} = 0 \quad 3.7.$$

From the continuous  $u$  field this can be written as

$$\mathbf{e}_u \cdot \nabla (\mathbf{e}_u \cdot \nabla u) + \frac{1}{S} \frac{dS}{d\xi} (\mathbf{e}_u \cdot \nabla u) = 0 \quad 3.8.$$

where  $\mathbf{e}_u$  is a unit vector pointing in positive  $u$ . Due to the applied boundary conditions, the vector  $\nabla u$  always has direction  $-\mathbf{e}_u$  and  $\mathbf{e}_u \cdot \nabla u = -|\nabla u|$ . This allows the flare to be calculated from  $u$  as

$$\frac{1}{S} \frac{dS}{d\xi} = \frac{-\mathbf{e}_u \cdot \nabla (|\nabla u|)}{|\nabla u|} \quad 3.9.$$

### 3.3 Examples

#### 3.3.1 In-plane bend

A channel of constant width that turns around a 45-degree corner.

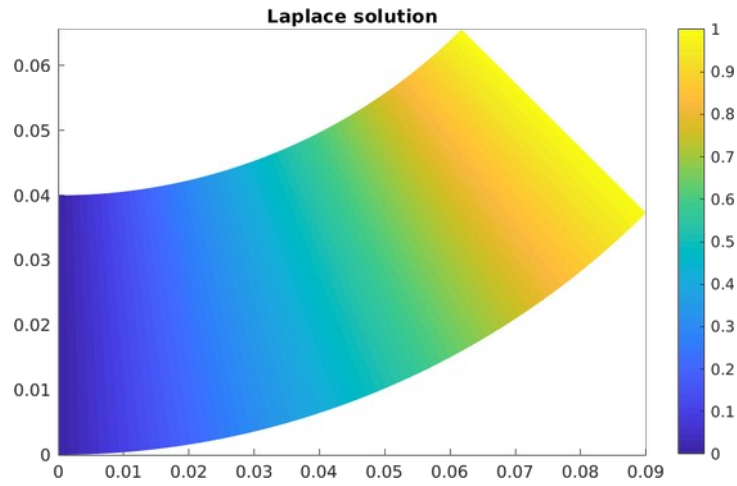


Figure 2. Numerically computed  $u$  for the in-plane bend.

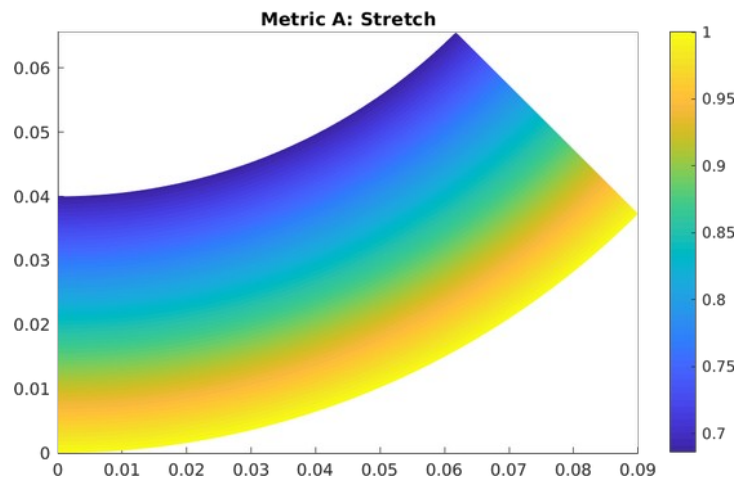


Figure 3. "Stretch" for the in-plane bend

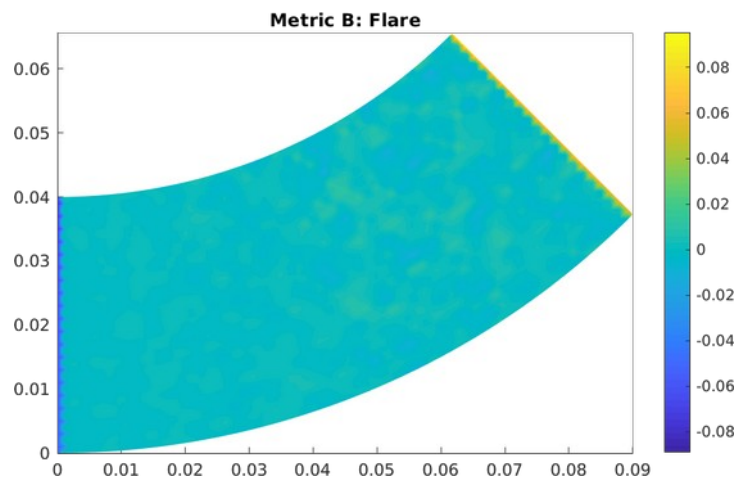


Figure 4. "Flare" for the in-plane bend

### 3.3.2 Wedge

A channel with constant angle of expansion

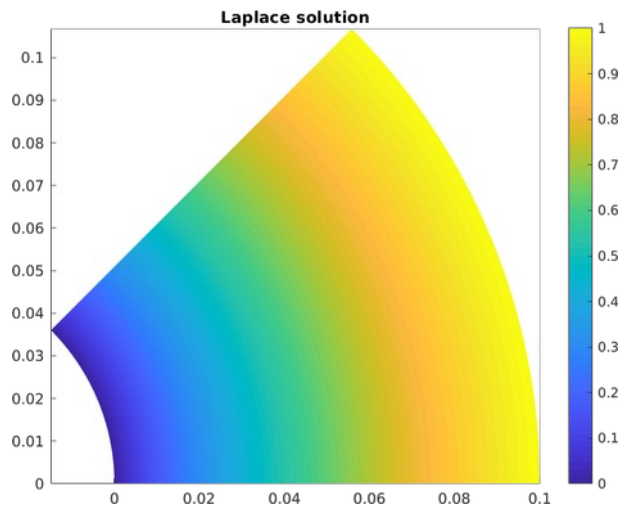


Figure 5. Numerically computed  $u$  for the in-plane bend.

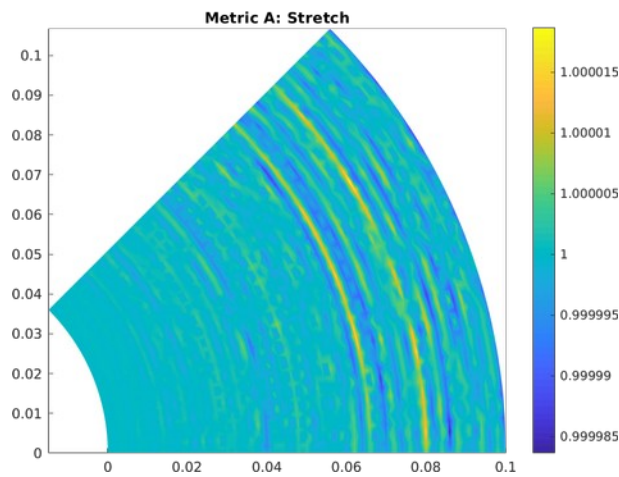


Figure 6. “Stretch” for the in-plane bend

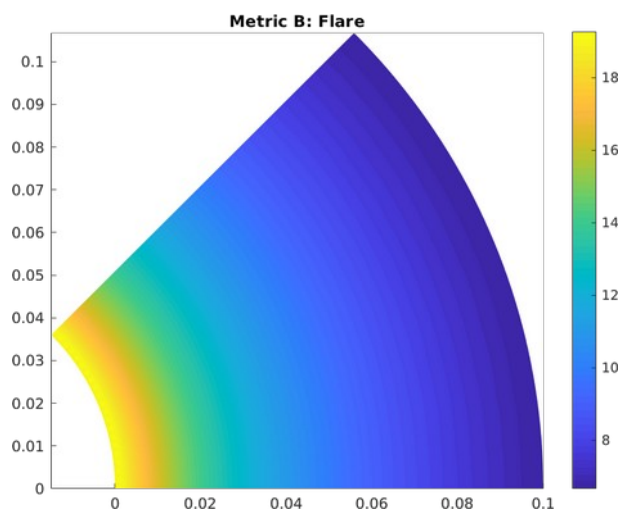


Figure 7. “Flare” for the in-plane bend. The analytical solution for flare is  $1/r$ . Maximum error is in the region of 1.5% with quadratic elements and concentrated on the throat and mouth of the waveguide.

### 3.3.3 Channel joining wedge

A straight channel joining a channel with constant angle of expansion

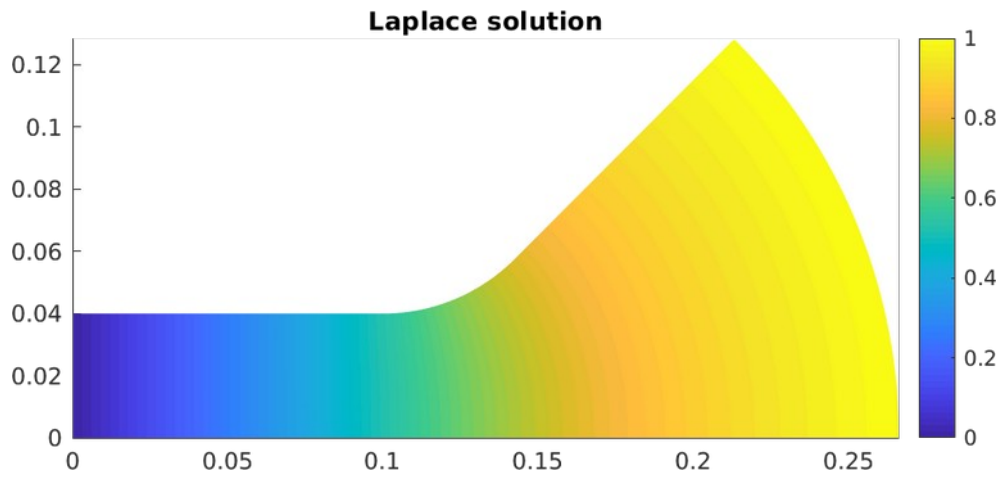


Figure 8. Numerically computed  $u$  for the channel joining wedge.

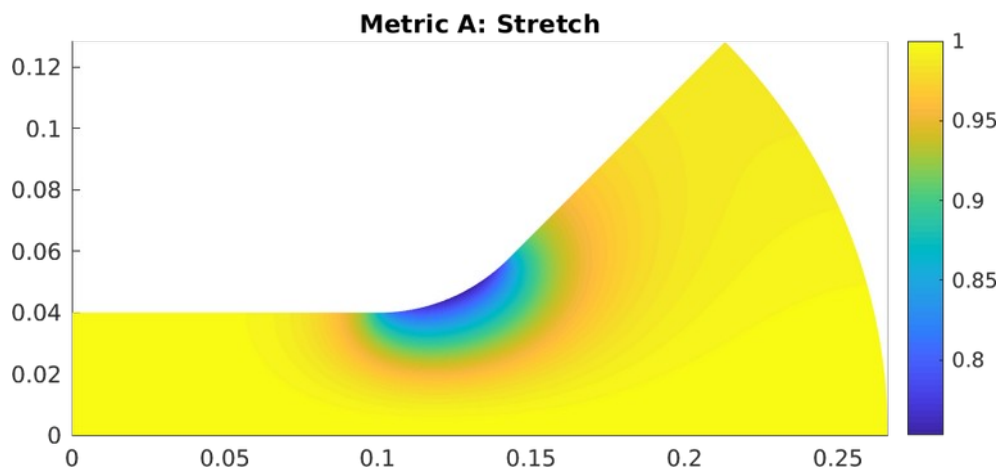


Figure 9. "Stretch" for the channel joining wedge.

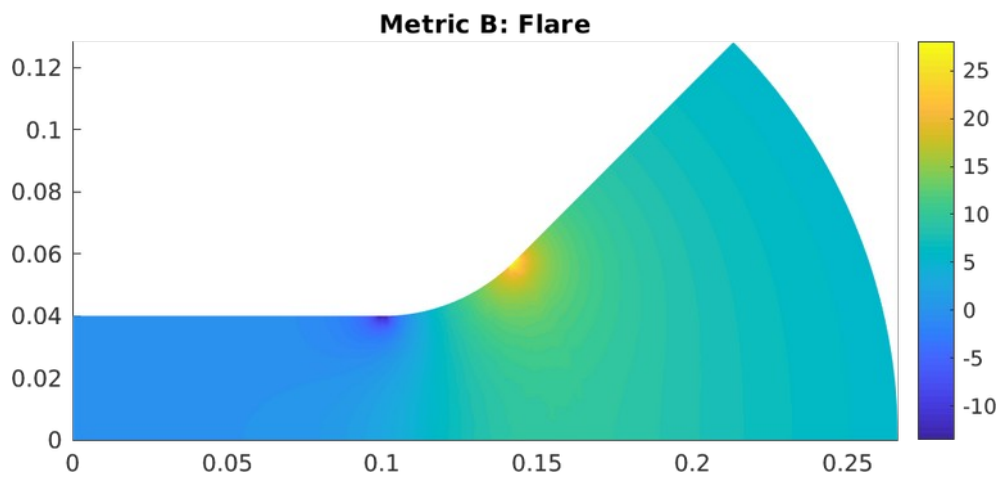


Figure 10. "Flare" for the channel joining wedge.

### 3.3.4 Simple arc annular to linear

Simple annular to linear formed by sweeping an arc of constant arc-length and varying the arc angle from 90deg to 0deg.

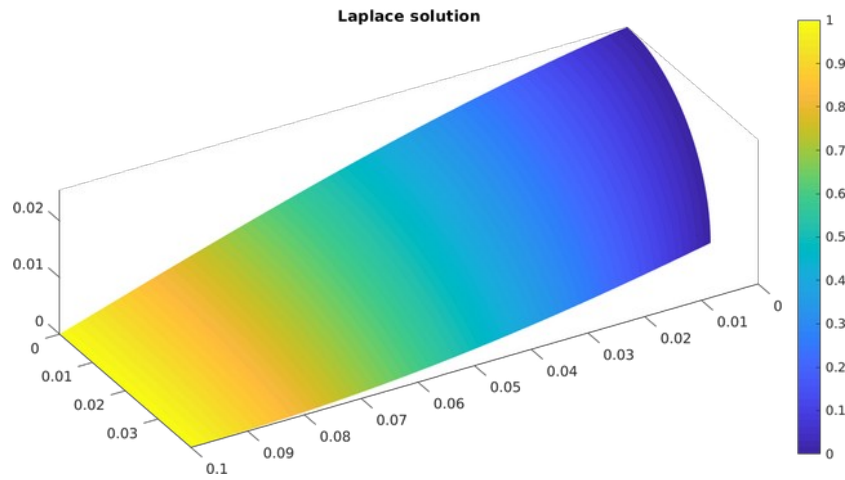


Figure 11. Numerically computed  $u$  for the simple annular to linear.

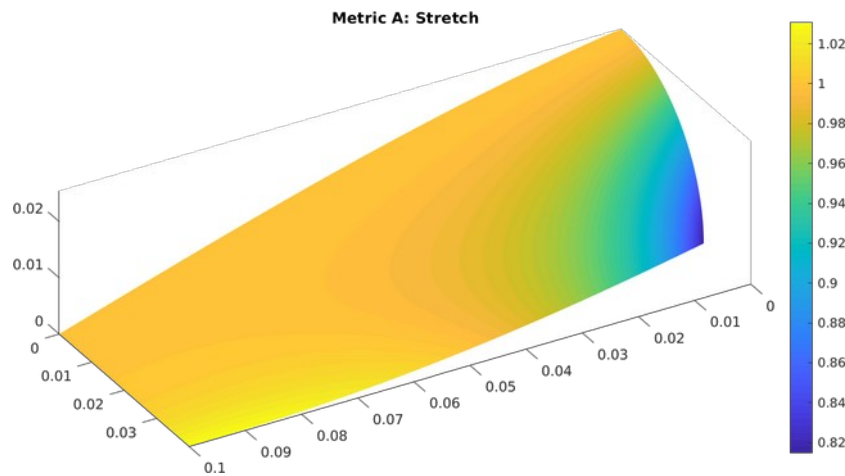


Figure 12. "Stretch" for the simple annular to linear.

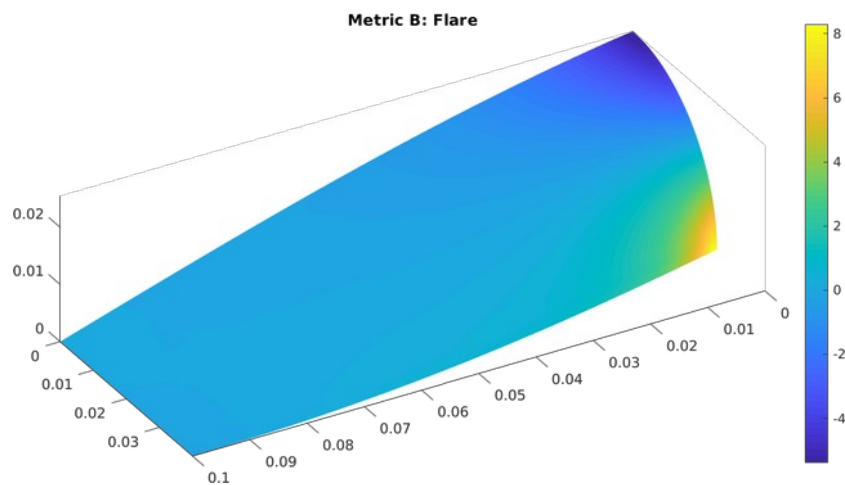


Figure 13. "Flare" for the simple annular to linear.

### 3.3.5 Simple elliptical annular to linear

Simple annular to linear formed by morphing an ellipse from a circle into a line. The minor axis is linearly changed through the waveguide, the circumference of the ellipse is fixed.

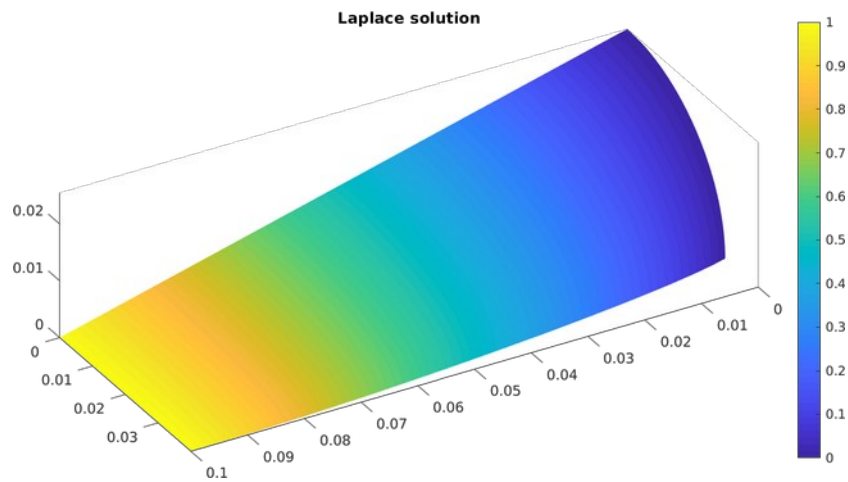


Figure 14. Numerically computed  $u$  for the simple elliptical annular to linear.

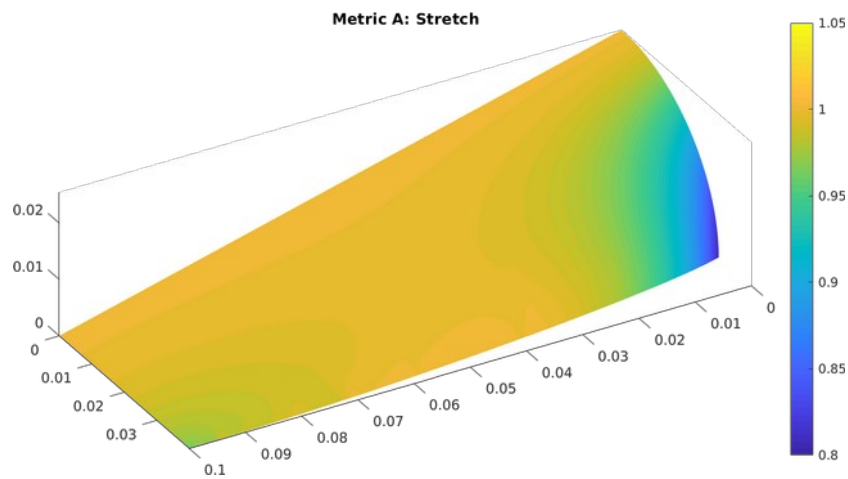


Figure 15. "Stretch" for the simple elliptical annular to linear.

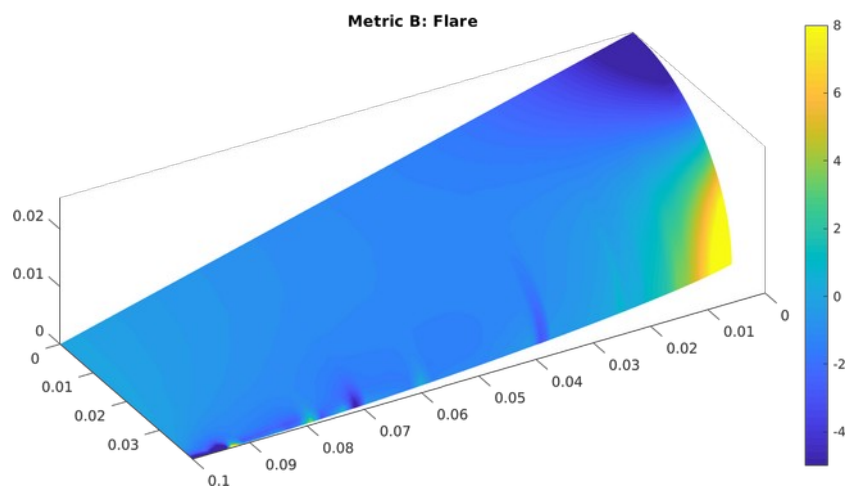


Figure 16. "Flare" for the simple elliptical annular to linear.